BEHAVIOR OF TWO-DIMENSIONAL AGGREGATES IN SHEAR FLOW

The work described in this thesis has been carried out in the group Physics of Complex Fluids at University of Twente. The work was supported financially by the Foundation for Fundamental Research on Matter (FOM) and was part of the research program of the Institute for Mechanics, Processes and Control - Twente and the J.M. Burgerscentrum.

ISBN 90-365-2386-9

BEHAVIOR OF TWO-DIMENSIONAL AGGREGATES IN SHEAR FLOW

DISSERTATION

to obtain
the doctor's degree at the University of Twente,
on the authority of the rector magnificus,
prof. dr. W.H.M. Zijm,
on account of the decision of the graduation committee,
to be publicly defended

on Friday 25^{th} August 2006 at 15.00

by

Nikolina Dimitrova Vassileva

born on 26^{th} November 1970
in Ihtiman, Bulgaria

This dissertation is approved by:

Promotor: Prof. Dr. J. Mellema
Assistant promotor: Dr. H.T.M. van den Ende

For Joris

Contents

Chapter 1

Introduction

1.1 General Background

Particles with attractive interactions dispersed in a Newtonian fluid may form aggregates. Under flow the aggregates can deform restructure, break up and merge with each other. This class of phenomena is wide spread in practical systems and at the heart of particulate flow which is a type of two-phase flow. The most widespread example of particulate flow is the flow of blood in our body [1]. Particulate flow is encountered in several industrial applications and environmental problems such as paper manufacturing, paint manufacturing, medical applications and waste water treatment [2, 3, 4, 5]. Amongst others it is highly relevant for food industry where a long-standing problem is the behavior of particle gels in flow [6, 7]. The scientific understanding of these systems is emerging but due to the complexity of the involved processes important questions remain unanswered. The influence of the hydrodynamics can not be figured out easily in an analytical way, since we deal with a multiple particle aggregate. Direct observations of the structural and configurational changes of an aggregate are lacking.

1.2 Aim of the project

To produce primary knowledge of aggregate behavior one better focuses on single aggregates with well defined particles and structures and good controllable experiments.

In this project we study experimentally single 2D aggregates, consisting of non-Brownian monodisperse attractive particles, in shear flow and analyze their behavior. The 2D plane coincides with the shear plane. The translation from 2D to 3D phenomena is not simple, however they will in general show similar features. We consider the 2D study as a model system for 3D studies. The focus of the study is the role of the hydrodynamics on the restructuring and breaking of the aggregates. We investigate the effects coming from the size of the primary particles, interface properties, aggregate size and initial shape.

1.2.1 Break-up criterion

Crucial assumption in the modeling of the processes is that the size of an aggregate is determined by a balance between the hydrodynamic force on it due to the ambient flow

field and its strength: a break-up criterion [8, 9, 10].

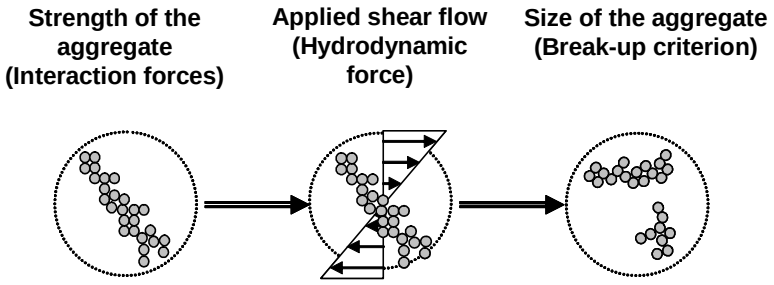

Figure 1.1: *Schematic representation of the break-up criterion.*

Figure 1.1 presents a schematic representation of the break-up criterion. The strength of the aggregate is defined by the superposition of repulsive and attractive forces between the primary particles. When the aggregate is subjected to a shear flow the hydrodynamic stresses acting on its surface may cause its break-up. The hydrodynamic forces are counteracted by the attractive forces between the particles. The break-up occurs when the hydrodynamic force overcomes the attractive forces.

1.2.2 Experimental approaches

Finding a good technique for studying floc strength is difficult. The flocs can be very different in size, shape, and they can be also very fragile. It is also difficult to compare the results from different studies because the results depend strongly on the technique that has been used for measuring floc strength.

Two distinctive breaking mechanisms have been identified: erosion and fragmentation [11, 12, 13]. Erosion consists of shearing of single particles or small fragments from the aggregate surface while rupture means breaking of the aggregate in two or more large pieces. It is believed that different forces are responsible for the two mechanisms. The erosion is caused by the shear force of the fluid on the surface of the aggregate. It is a slow process and dominates at moderate stresses. Rupture occurs when the hydrodynamic stress exceeds the cohesive force and is assumed to be caused by the pressure difference inside the aggregate.

Most researches investigate the dependence of the floc size as a function of the applied hydrodynamic shear flow. For a review of the experiments performed in 3D one can refer to Jarvis and coworkers [12]. In general, it is assumed that the maximum final size of an aggregate in a shear flow is inversely proportional to the rate of shear to some power (break-up criterion). This criterion leads to a length scale, which determines the maximum size of an aggregate as a function of shear flow [14]. The simplest way of evaluating the floc strength is to measure the ratio between the floc size before and after break-up for a given shear rate [15]. The higher the strength factor is, the stronger the flocs are. The floc strength is connected to the floc structure, which is defined by the number and strength of bonds between the individual particles inside the floc. It was found that increasing the floc compactness will increase the floc strength due to the higher number of bonds between the particles. The floc strength can be related to the energy dissipation of the system or the velocity gradient applied to the system. This

approach relays upon complex theories and floc break-up models. Additionally, the floc visualization in the vessel is difficult (when using optical microscopy), expensive (when using light scattering) and sometimes rely on invasive techniques (such as taking samples) that can influence the results.

Recently developed techniques directly measure the force needed for a floc rupture. Yeung and Pelton [16] use micromechanical techniques to pull apart flocs. They found that break-up occurs at the weakest spot inside the aggregate. Thus, a compact aggregate will break due to erosion. The aggregate strength did not depend on the aggregate size. Another technique (micromanipulations) explored the break-up of flocs by compression [17]. These techniques provide direct insight into aggregate breaking, however the number of experiments and hence the received results are limited.

In 2D most of the research has been concentrated on the investigation of particle monolayers at a liquid interface [18, 19, 20, 21]. Stancik investigated the effect of shear [18] and elongational flow [19] on the structure of a monolayer of particles at a water/oil interface. The lattice structure was observed to pass from a hexagonal array through a liquid-like state, at start-up of the flow, to a semi-ordered state during steady flow. Aveyard [20, 21] also studied monolayers of particles at an interface when compressed in a Langmuir trough. At the water/air interface the particles were packed in a hexagonal array while at the water/oil interface they went through a transition from a hexagonal to a rhombohedral structure. The monolayer collapses by folding and corrugation when the surface pressure equals the interfacial tension, but the particles did not migrate from the interface under the compression.

Two types of 2D suspensions of colloidal particles have been studied by Hoekstra and coworkers [22]: systems in which the particles can and can not slide along each other, depending on the strength of the attractive interparticle potential. They found that shear flow induces the same type of anisotropy in both systems. To probe this anisotropy the Fourier transforms of the aggregate images were studied. In the system with a strongly attractive potential the density inside the aggregates increases with the applied shear flow while it decreases in system with a weak attraction between the particles. Break-up was found to occur at the weakest link in the aggregate (at a single contact point between the particles) and erosion was not observed.

Hansen and coworkers [23] studied 2D colloidal aggregation in a Couette cell. The cluster size and structure was followed at different shear rates. The weakly aggregated systems showed rearrangement into a more compact structure and a densification with increasing shear rate while the strongly aggregated systems did not display a significant change in structure.

1.2.3 Analytical models

Analytical models can be used to describe the aggregate break-up. These models generally simplify the aggregate structure. The two limiting cases are a uniform impermeable [24] or permeable [25] sphere. Bagster and Tomi [24] calculated that for a homogeneous impermeable sphere the rupture occurs on a plane trough the center of the sphere while the critical shear rate does not depend on its size. Adler and Mils [25] considered the aggregate as uniform porous sphere. In that case the critical shear rate depends on the aggregate size; it is less for smaller aggregates. However for large flocs the critical shear rate approach to a constant value similar to the case considered by Bagster and Tomi. The work of Sonntag and Russel [26] is a further development of the Adler-Mils theory to non-uniform flocs. Again the considered flocs are porous and permeable to the flow.

They assume in their model that there is no internal rearrangements and that break-up occurs near the surface of the flocs. Their results show a dependence of the floc size on the shear rate.

The fracture of the aggregate is assumed to occur along planar surfaces (usually passing through the aggregate center) [24, 27] or by crack growth [28]. The several models for break-up predict a different dependence on the volume fraction and the radius of the primary particles.

Only a few studies dealing with erosion have been carry out [29, 30, 31]. Powell and Mason [29] described the erosion kinetics for compact spherical aggregates without attraction between the primary (cohesionless) particles. They found that the erosion rate depends on the flow type and the ratio between the aggregate and primary particle size, but it is independent of the shear rate.

1.2.4 Numerical simulations

Numerical simulations are needed for computing multiple particles hydrodynamic interactions or transient behavior. The set of differential equations is too large or too many variables are present to be solved analytically. Various numerical simulations have been carried out. Doi and Chen [32] proposed the sticky sphere model in which the particles are assumed to stick to each other. They can roll over each other without slipping at their contact points. It is assumed that the hydrodynamic drag force acts on all particles in the aggregate even when they are not directly exposed to the flow. Thus the model is applicable to small number of particles in which the assumption is valid. Bossis and Brady proposed the Stokesian Dynamics [33], which calculates rigorously the mutual hydrodynamic interactions. Although the method has been improved during the years, as the Accelerated Stokesian Dynamics [34], it still requires long computational times which also limits the number of particles that can be considered. Another method is the Discrete Element Method (DEM) developed by Cundal [35] and later modified by Higashitani for aggregates in 2D [36] and 3D [37]. The method starts by putting all particles at certain positions with some initial velocities. At every time step the total force acting on each particles is computed and from there the change in the position and velocity. The method is very convenient for visualizing transient behavior. A limitation at the moment is that there is no DEM that takes into account the exact local flow field.

1.3 Thesis outline

The thesis is organized as follows. In chapter 2 the considerations with respect to the design and operation of the experimental setup are presented. The first part of the chapter is devoted to the flow field while the second describes the liquid-liquid interface shape.

In chapter 3 particles at the interface, before introducing a shear flow, are treated. The interface deformation that a single particle creates is described. Next the exact boundary conditions for the three phase contact line on a wall, cylinder and sphere are derived. The exact interface profile is calculated by solving the linearized Young-Laplace equation. Then the capillary interactions between two spherical particles are considered.

The theory for capillary interactions is extended further in chapter 4 for an arbitrary number of particles and allowing also for a background curvature of the interface. The theoretical findings are supported by experimental results for pairs of interacting particles

at an interface with a slight macroscopic background curvature. Particle velocities are measured and compared with model calculations based on a force balance.

Next in chapter 5 the results for the critical shear rate for break-up of aggregates with different sizes in a simple shear flow are presented. The evolution of the aggregate structure before break-up is also investigated. A simple theoretical model is developed for aggregate rupture. In the model the aggregate is considered as solid circular disk that will break near a middle line.

In chapter 6, the investigation of the aggregates structure and breaking is continued, with more experimental systems introduced. Special attention is paid to how and where the aggregates rupture. The theoretical model from chapter 5 is developed further by calculating also the critical shear for erosion and erosion kinetics. The thesis ends with an overview and perspectives in chapter 7, followed by a short summary.

References

[1] Das R. N. , Seshadri V. *Bull Math Biol.* **1975**, 37(5), 459.

[2] Vermant J. *Curr. Opin. Colloid Interface Sci.* **2001**, 6, 489.

[3] Tadros, Th. F. *Solid-liquid dispersion*, Academic press, **1987**.

[4] B.A. Wills, *Mineral processing technology (Int. Ser. Material Sci. Technology, vol 41),* Pergamon press, Oxford **1988**.

[5] Elimelech M., Gregory J., Jia X., Williams R.A. *Particle deposition and Aggregation*, Butterworth-Heinemann, Woburn, **1998**.

[6] van Vliet T., Luyten H., Walstra P., *Fracture and Yield of gels (proc. Symp. Norwich)*, Royal Society of Chemistry, **1991**.

[7] Whittle M., Dickinson E., *Faraday Trans* **1998**, 94(1), 129.

[8] de Rooij R., Potanin A.A., van den Ende D., Mellema J., *J. Chem. Phys.* **1993**, 99, 9213.

[9] Potanin A.A., de Rooij R., van den Ende D., Mellema J., J. *Chem. Phys.* **1995**, 102, 5845.

[10] Wolthers W., Duits M.H.G., van den Ende D., Mellema J., *J. of Rheology* **1996**, 40(5), 799.

[11] Parker D.S., Kaufmann W. J., Jenkins D. J., *San. Eng. Div. Proc. Amer. Soc. Civ. Eng.* **1972**, 98, SA1, 79.

[12] Jarvis P., Jefferson B., Gregory J. and S.A Parsons, *Water Research* **2005**, 39, 3121.

[13] Ottino J.M, DeRoussel, Hansen S. and Khakhar D.V., *Adv. Chem. Eng.* **1999**, 25, 105.

[14] Hunter R. J., Frayene J., *JCIS*, **1980**, 76, 107.

[15] Gregory J., Monitoring floc formation and breakage (Proc. Nano Micro Particles Water Wastewater Treatment Conf.), International Water Association, Zurich, **2003**.

[16] Yeung A.K., Pelton R., *JCIS* **1996**, 184,579.

[17] Zhang Z., Sisk M. L., Mashmoushy H. and Thomas C.R. *Part. Part. System Characterisation* 16, 278, **1999**.

[18] Stancik E. J., Gavranovich G. T., Widebrant M. J. O, Laschitsch A. T., Vermant J. and Fuller G. G., *Faraday Discuss.* **2003**, 123, 145.

[19] Stancik E. J., Hawkinson A. L., Vermant J. and Fuller G. G., *J. Rheol.* **2004**, 48(1), 159.
[20] Aveyard R., Clint J. H., Nees D., Paunov V. N. *Langmuir* **2000**, 16, 1969.
[21] Aveyard R., Clint J. H., Nees D., Quirke N. *Langmuir* **2000**, 16, 8820.
[22] Hoekstra H., Vermant J. and Mevis J., *Langmuir* **2003**, 19, 9134.
[23] Hansen P. H., Malmsten M., Bergenstahl B.,Bergstrom L. *JCIS* **1999**, 220,269.
[24] Bagster D. F., Tomi D., *Chem. Eng. Sci.* **1974**, 29, 1773.
[25] Adler P. M., Mills P. M. *J. of Rheol.* **1979**, 23, 25.
[26] Sontag R. C. and Russel W. B. , *JCIS* **1987**, 115, 378.
[27] Rumpf H., *Agglomeration* (W.A.Knepper Ed.), Wiley Interscience, New York, **1962**.
[28] Kendall K., *Powder Metallurgy* 31, 28, **1988**.
[29] Powel R. L. and Mason S. G. *AIChE J* **1982**, 28, 286.
[30] Pandya J.D. and Spielman L. A., *JCIS* **1982**, 90, 517.
[31] Thomas D. G., *AIChE* **1964**, 10(4), 517.
[32] Chen D., Doi, M. *J. of Colloid Interface Sci.* **1999**, 212, 286.
[33] Bossis G., Brady J. F. *J. Chem Phys.* **1984,** 80, 5141.
[34] Sierou A., Brady J.F., *J. Fluid. Mech.*, 2001, 448, 115.
[35] Cundall p. A. and Strack O. D. L., *Geotechnique* **1979**, 29(1), 47.
[36] Higshitani Ko, Iimura K., *JCIS* **1998**, 204, 320.
[37] Higshitani Ko, Iimura K., Sanda H., *Chem. Eng. Sci.* **2001**, 56, 2927.

Chapter 2

Description of the experimental set-up and instrumental characteristics

Abstract

In the present chapter we describe the counter rotating Couette device, used in this study. Also the flow field in the Couette device is discussed. Not only the steady state is considered but also the transient behavior due to changes in the cylinder speeds. From this analysis a response time of about 45 s was obtained, indicating that position control of an object in the flow field, using a feedback loop, is not feasable. Moreover, the shape of the undistrubed liquid-liquid interface is described and how it is controled in the experiments. To this end a laser refraction method is presented.

2.1 Introduction

In the present chapter the considerations with respect to the design and operation of the experimental setup will be treated. In Figure 2.1 the experimental setup is depicted, it basically consists of a Couette cell, containing two immiscible fluid layers with the aggregate particles confined at their interface. The upper fluid is air or an oil, while the lower phase is aqueous. The aggregate behavior is recorded by means of a microscope fitted with a camera and linked to a video-recorder. In order to be able to watch the particles at a fixed position, a stagnant line of flow has to be maintained at the interface by means of rotating the inner- and outer Couette cylinders in opposite direction. The radial position of the stagnant line may be controlled by appropriately adjusting the speed of the cylinders.

The behavior of the aggregate is determined by the forces acting from the flow field on the particles, therefore we need to know the exact shape of the flow field. In the first part of this chapter the steady state flow field will be treated, then the transient response of the flow field to a change in rotational speed of the cylinders will be determined. The aim of the calculations is to provide better insight into the experiments.

The shape of the interface may add an extra force to the system due to its curvature. Characterization and control of the interface shape is therefore necessary. In the

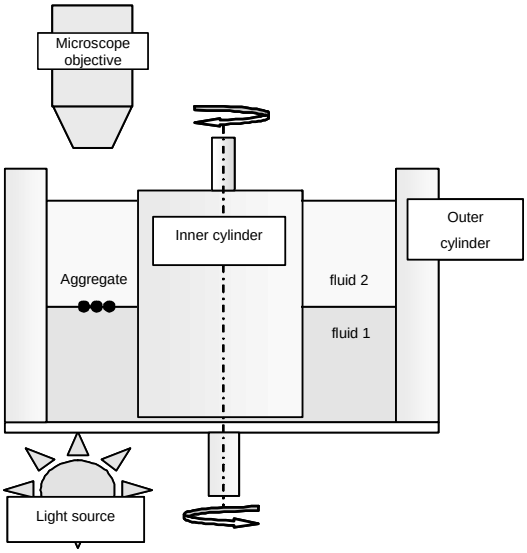

Figure 2.1: *Schematic of the experimental set-up.*

second section the interface shape will be calculated and methods will be presented for characterizing and controlling it.

2.2 Description of the flow field in a counter rotating Couette device

We assume steady, laminar and isothermal flow and non slip at the cylinders walls. The presence of the interface is omitted and the gap is filled with a Newtonian fluid. The calculations were made considering water as the liquid phase. First the velocities and shear distribution in the gap are given followed by expressions for the stagnant zone position and shear rate. Then the size of the aggregate is taken into consideration and the shear variation over the entire aggregate is discussed. Taylor number for the fluid and the bottom effect are calculated too in order to characterize the stability of the flow.

2.2.1 Calculation of the shear rate and velocity profile in the gap

One has to consider flow of a fluid confined between the two counter rotating concentric cylinders. The inner and the outer cylinder have radii a and b and the angular velocities are Ω_a and Ω_b, respectively (as shown in Figure 2.2). In our case $a = 24$ mm and $b = 45$ mm. The annular gap between them is filled with a Newtonian fluid with viscosity η. For the calculation cylindrical coordinates (r, ϕ, z) were used.

According to the Newton's viscosity law the shear stress τ can be written as:

$$\tau = \eta\dot{\gamma} \tag{2.1}$$

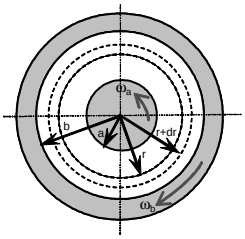

Figure 2.2: *Scheme of the Couette geometry.*

The shear rate $\dot{\gamma}$ at a radial distance r from the axis can be expressed as follows:

$$\dot{\gamma} = r\frac{d\omega}{dr} \tag{2.2}$$

At a small element of the cylindrical surface $dA = rd\phi dz$ at radius r of height L, the tangential force dF resulting from the internal friction equals the stress times area:

$$dF = \tau r d\phi dz$$

while the corresponding torque M is given by:

$$dM = rdF = \tau r^2 d\phi dz$$

The last differential equation can be integrated:

$$M = \int_0^L \int_0^{2\pi} \tau r^2 d\phi dz = 2\pi L r^2 \tau$$

Since the liquid does not undergo an angular acceleration this torque M should be constant. Thus the shear stress is given by:

$$\tau = \frac{M}{2\pi L r^2} \tag{2.3}$$

By combining Eqs.(2.1), (2.2) and (2.3) one obtains:

$$r\frac{d\omega}{dr} = \frac{M}{2\pi L\eta} \cdot \frac{1}{r^2}$$

or:

$$\frac{d\omega}{dr} = c_1 \cdot \frac{1}{r^3} \tag{2.4}$$

where the constant c_1 is given by:

$$c_1 = \frac{M}{2\pi L\eta}$$

The solution of Eq.(2.4) is:

$$\omega(r) = c_2 - c_1\frac{1}{2r^2} \tag{2.5}$$

where c_2 is a integration constants. c_1 and c_2 can be found from the boundary conditions. We assume that there is no slip at the cylinders walls:

$$\omega(a) = -\Omega_a \qquad \text{and} \qquad \omega(b) = \Omega_b$$

where the angular velocities are taken with opposite sign (counter rotating cylinders). Then:

$$c_1 = \frac{2a^2b^2\left(\Omega_a + \Omega_b\right)}{b^2 - a^2} \qquad \text{and} \qquad c_2 = \frac{a^2\Omega_a + b^2\Omega_b}{b^2 - a^2}$$

Now one can find expressions for angular velocity, shear rate and shear stress as a function of the radial distance r:

$$\omega\left(r\right) = \frac{a^2b^2\left(\Omega_a + \Omega_b\right)\left(a^{-2} - r^{-2}\right)}{b^2 - a^2} - \Omega_a \tag{2.6}$$

$$\dot{\gamma}\left(r\right) = \frac{2a^2b^2}{\left(b^2 - a^2\right)r^2}\left(\Omega_a + \Omega_b\right) \tag{2.7}$$

$$\tau\left(r\right) = \eta\frac{2a^2b^2}{\left(b^2 - a^2\right)r^2}\left(\Omega_a + \Omega_b\right) \tag{2.8}$$

Using Eq. (2.7) we can plot graphically the shear rate distribution in the gap between the cylinders. In Figure 2.3 shear rate as a function of r is shown. From the plot it is clear that the shear rate is not constant in the gap. Shear rate changes across the gap are expected with a wide gap Couette device [1]. The variation is higher for higher angular velocities as can be seen from Figure 2.3.

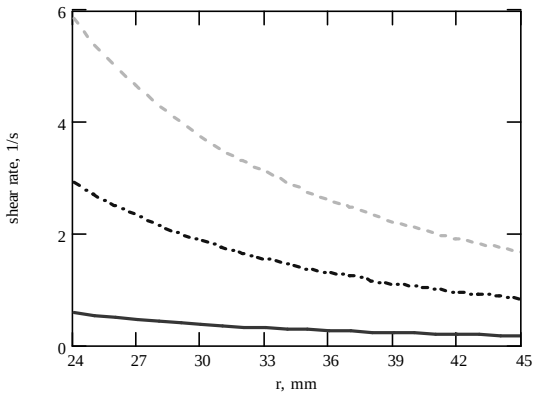

Figure 2.3: *Shear rate variation across the gap. The lines corresponds to different velocities of the cylinders: solid line* $\Omega_a = 1$ *rpm, dash-dot line* $\Omega_a = 5$ *rpm and dot line* $\Omega_a = 10$ *rpm. In all cases the ratio* $\Omega_a/\Omega_b = 1$.

It is interesting to note that the variation of $\Delta\dot{\gamma}$ over the gap is independent of the relative gap width:

$$\Delta\dot{\gamma} = \dot{\gamma}_a - \dot{\gamma}_b = 2\ \left(\Omega_a + \Omega_b\right)$$

However the relative variation is equal to:

$$\frac{\Delta\dot{\gamma}}{\langle\dot{\gamma}\rangle} = 2\,\frac{\dot{\gamma}_a - \dot{\gamma}_b}{\dot{\gamma}_a + \dot{\gamma}_b} = 2\,\frac{b^2 - a^2}{b^2 + a^2}$$

i. e. the relative variation is independent of the rotational speeds and decreases with decreasing gap width.

Above equation (2.7) can be derived also directly from the Navier-Stokes equation for low Reynolds numbers as it was done in [2], [3]. The final result will be the same.

2.2.2 Stagnant zone position and shear rate

The position of the stagnant zone can be calculated from Eq.(2.5) with the condition $\omega = 0$ at $r = r_s$. Then:

$$\omega(r_s) = -\frac{1}{2}c_1 r_s^{-2} + c_2 = 0$$

$$r_s = \sqrt{\frac{c_1}{2c_2}}$$

$$r_s = \sqrt{\frac{a^2 b^2\,(\Omega_a + \Omega_b)}{a^2\Omega_a + b^2\Omega_b}} \tag{2.9}$$

Using Eqs.(2.7) and (2.9) one can calculate also the shear rate at the stagnant layer:

$$\dot{\gamma}_s = \frac{2\left(a^2\Omega_a + b^2\Omega_b\right)}{b^2 - a^2} \tag{2.10}$$

2.2.3 Shear rate variation over the floc

As presented in Figure 2.3, the shear rate varies across the gap. Thus one has to calculate also the variation in the shear rate over the entire aggregate. For aggregates the maximum relative variation of the shear rate over the aggregate at the stagnant zone is given by:

$$\frac{\Delta\dot{\gamma}}{\dot{\gamma}} = \frac{D}{\dot{\gamma}}\left|\frac{d\dot{\gamma}}{dr}\right| = \frac{2D}{r_s}$$

where D is the diameter of the aggregate and r_s the position of the stagnant zone. For a typical aggregate considered in the experiments (2 mm diameter) the variation of the shear rate is about 10 % over the whole aggregate.

2.2.4 Laminar flow and Taylor vortices

The analytical solution for the flow profile assumes a laminar flow. At higher rotational speeds the laminar flow in the gap becomes distorted and Taylor vortices could arise [4]. When Taylor vortices occur the actual flow field will differ from the calculated one and will influence the hydrodynamic stresses on the aggregates at the interface. Below an estimate of the shear rate at which Taylor vortices are expected to appear is given.

It is known that the instabilities will first occur for a rotating inner cylinder. For simplicity we will consider that only the inner cylinder is rotating. The outer cylinder is assumed to be stationary. The criterion of stability for long cylinders is given by:

$$Re < Re_{\text{crit}} = 41.5\sqrt{\frac{b}{b-a}} = 60.5$$

For our system: $Re = \rho v_{\rm rms}\,(b-a)\,/\eta$, where $v_{\rm rms} \simeq \sqrt{1/3}a\Omega_a$ is the root mean square velocity in the gap. (The average velocity is close to zero due to the counterrotating cylinders.) Moreover the Ω_a can be linked to the shear rate $\dot{\gamma}_s$ at the stagnant zone if $r_s = (a+b)/2$:

$$\dot{\gamma}_s = \frac{2a^2}{r_s^2 - a^2}\Omega_a$$

Then:

$$\dot{\gamma}_s < \frac{2a}{r_s^2 - a^2}\frac{\eta\sqrt{3}Re_{\rm crit}}{\rho\,(b-a)} \simeq 1\,{\rm s}^{-1}$$

In the experiments $\dot{\gamma}$ ranges from 0 to 2.5 s^{-1} so we may expect the onset of Taylor vortices. However, we have to consider also the presence of the interface. The interface is expected to play a stabilizing role preventing the development of the vortices. This is supported by the experiments, where outward motion of particles or dust was not observed.

2.2.5 Finite size effects

At the gap between the bottom of both cylinders there will be also a shear flow due to the rotation of the bottom with the outer cylinder [5]. The presence of this gap can influence the flow profile at the interface. The creeping flow equation for $\omega(r,z)$:

$$\frac{\partial^2\omega}{\partial r^2} + \frac{3}{r}\frac{\partial\omega}{\partial r} + \frac{\partial^2\omega}{\partial z^2} = 0$$

was solved numerically for the geometry of the shear cell.

[This equation can be obtained by considering the torque balance on an annulus of liquid bounded by the planes: $r = $ const, $r + dr = $ const, $z = $ const, $z + dz = $ const:

$$\begin{aligned} 2\pi dz\left((r+dr)^2\,\tau_{r\phi}(r+dr,z) - r^2\tau_{r\phi}(r,z)\right) \\ + 2\pi r^2 dr\,(\tau_{z\phi}(r,z+dz) - \tau_{z\phi}(r,z)) \end{aligned} \quad = \quad 0 \qquad (2.11)$$

$$\text{or} \qquad \frac{\partial}{\partial r}\left(r^2\tau_{r\phi}\right) + \frac{\partial}{\partial z}\left(r^2\tau_{z\phi}\right) \quad = \quad 0 \qquad (2.12)$$

where $\tau_{r\phi} = \eta r\partial\omega/\partial r$ and $\tau_{z\phi} = \eta r\partial\omega/\partial z$. Substitution of these expressions in Eq 2.12 results in the given differential equation.]

The boundary conditions for this geometry are given by:

$$\left.\begin{array}{ll} r = a & h_1 < z < h_2 \\ z = h_1 & 0 < r < a \end{array}\right\} \qquad \omega(r,z) = -\Omega_a$$

$$\left.\begin{array}{ll} r = b & 0 < z < h_2 \\ z = 0 & 0 < r < b \end{array}\right\} \qquad \omega(r,z) = \Omega_b$$

$$\left.\begin{array}{ll} z = h_2 & a < r < b \end{array}\right\} \qquad \frac{\partial\omega}{\partial z}(r,z) = 0$$

where $z = 0$ corresponds to the bottom plane of the outer cylinder, $z = h_1$ corresponds to the bottom plane of the inner cylinder and $z = h_2$ corresponds to the liquid-fluid

interface. Using a finite volume scheme a set of algebraic equations was obtained. This set was solved following the accelerated relaxation method. Figure 2.4 shows the resulting ω field (Figure 2.4a) and the rotational speed and shear rate along the interface at $z = h_2$ (Figure 2.4b). For simplicity the inner cylinder is taken stationary ($\Omega_a = 0$) and only the rotation of the outer has been considered. In Figure 2.4b the angular velocity and the shear rate for the real and the ideal (infinitely long cylinders) geometry are compared. No significant differences can be observed. Clearly the assumption to neglect edge effects for the analytical expression of the flow field is justified.

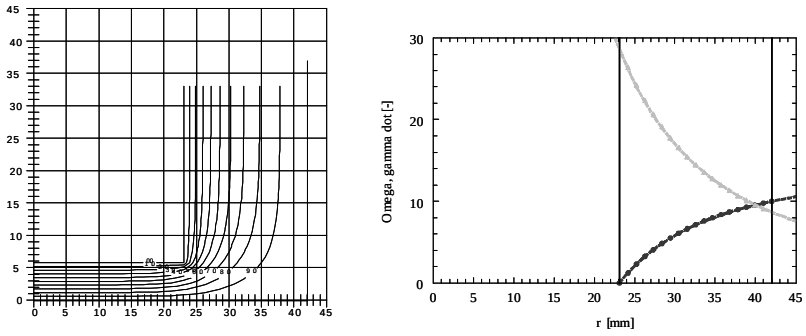

a) b)

Figure 2.4: *a) The velocity distribution in the gap between the two cylinders. The inner cylinder is considered stationary. The calculations are made until the interface level (33 mm from the bottom). b) Comparison between the ideal system (presented with the lines) and real one (the points). With black color is presented the angular velocity and with grey- the shear rate.*

2.3 Response of the fluid to the speed adjustments

To keep the aggregate in the stagnant zone and consequently in the field of view of the camera, the cylinder speeds have to be adjusted using a feedback loop. Crucial in this approach is the response time of the flow field to these adjustments. In the experiments it was observed that when the motion of the cylinders is stopped suddenly, the fluid and the particles are still moving for relatively long time. Therefore we calculate the transient velocity profile in the fluid.

The calculations were done following Bird [6],[7]. Let us consider a liquid layer between two moving concentric cylinders. The system is depicted in Figure 2.2. The cylinders are moving with velocities Ω_a and Ω_b in opposite directions. The gap between them is $(b-a)$. For our system $v_r = v_z = 0$ and $v_\theta = r\omega(t, r)$ where v is the velocity. From the equation of motion for an incompressible fluid we find that:

$$2\pi r^3 dr dz \rho \frac{\partial \omega}{\partial t} = 2\pi dr dz \eta \frac{\partial}{\partial r}\left[r^3 \frac{\partial \omega}{\partial r}\right] \tag{2.13}$$

where η is the viscosity and ρ the density of the liquid phase.

The initial and the boundary conditions for the above equation are:

$$\omega = 0 \quad \text{at} \quad t = 0$$

$$\omega = -k\Omega_a \quad \text{at} \quad r = a = kb$$

where $k = a/b$ is the ratio between the cylinders radii. In our case $k = 0.53$.

$$\omega = \Omega_b \quad \text{at} \quad r = b$$

The following dimensionless quantities are introduced:

$$\begin{array}{lcl} \text{Radial coordinate:} & \xi & = & \dfrac{r}{b} \\ \text{Time:} & \tau & = & \dfrac{\eta t}{\rho b^2} \\ \text{Tangential velocity:} & \phi & = & \dfrac{r\omega}{b\Omega} \\ \text{Angular velocity:} & \alpha & = & \dfrac{\Omega_a}{\Omega} \end{array}$$

where $\Omega = \Omega_b + \Omega_a$. Then Eq.(2.13) becomes:

$$\frac{\partial \phi}{\partial \tau} = \frac{\partial}{\partial \xi}\left[\frac{1}{\xi}\frac{\partial}{\partial \xi}(\xi\phi)\right] \tag{2.14}$$

With initial and boundary conditions:

$$\phi = 0 \quad \text{at} \quad \tau = 0$$

$$\phi = \frac{-a\Omega_a}{b\Omega} = -k\alpha \quad \text{at} \quad \xi = k \tag{2.15}$$

$$\phi = \frac{b\Omega_b}{b\Omega} = 1 - \alpha \quad \text{at} \quad \xi = 1 \tag{2.16}$$

The solution has the form:

$$\phi(\xi, \tau) = \phi_\infty(\xi) - \phi_{tr}(\xi, \tau)$$

where $\phi_\infty(\xi)$ is the steady-state solution which will be reached for $\tau \to \infty$. It can be received from Eq.(2.14) with $\partial\phi/\partial\tau = 0$, i.e.:

$$\phi_\infty(\xi) = \left[\frac{1 - \alpha\left(1 - k^2\right)}{1 - k^2}\right]\xi - \left[\frac{k^2}{1 - k^2}\right]\xi^{-1} = A\xi - B\xi^{-1}$$

This expression is equivalent to Eq. (2.6). The transient function $\phi_{tr}(\xi, \tau)$ is also solution of Eq.(2.14), now with the initial and boundary conditions:

$$\phi_{tr} = \phi_\infty \quad \text{at} \quad \tau = 0 \tag{2.17}$$

$$\phi_{tr} = 0 \quad \text{at} \quad \xi = k$$

$$\phi_{tr} = 0 \quad \text{at} \quad \xi = 1$$

According to the method of separation of variables, we can represent ϕ_{tr} as:

$$\phi_{tr}(\xi,\tau) = f(\xi)\, g(\tau)$$

Then from Eq.(2.14) we can generate two ordinary differential equations:

$$\begin{array}{l} \frac{1}{g}\frac{dg}{d\tau} = -\lambda^2 \\ \frac{1}{f}\frac{d}{d\xi}\left[\frac{1}{\xi}\frac{d}{d\xi}(\xi f)\right] = -\lambda^2 \end{array} \tag{2.18}$$

where λ is a separation constant.

A solution of the first expression in Eq.(2.18) is:

$$g(\tau) = \exp\left(-\lambda^2\tau\right) \tag{2.19}$$

The second equation can be transformed to:

$$\xi^2\lambda^2\frac{d^2f}{d(\xi\lambda)^2} + \xi\lambda\frac{df}{d(\xi\lambda)} + \left(\xi^2\lambda^2 - 1\right) f = 0$$

which is the Bessel equation and has solution [8]:

$$f(\xi) = AJ_1(\lambda\xi) + BY_1(\lambda\xi)$$

in which A and B are constants and J_1 and Y_1 are Bessel functions of first order. From the boundary conditions (Eq. 2.17), one can receive:

$$\begin{aligned} 0 &= AJ_1(\lambda) + BY_1(\lambda) \\ 0 &= AJ_1(\lambda k) + BY_1(\lambda k) \end{aligned}$$

And thus:

$$\begin{aligned} B &= -\frac{J_1(\lambda)}{Y_1(\lambda)}A \\ B &= -\frac{J_1(\lambda k)}{Y_1(\lambda k)}A \end{aligned}$$

From these equations one obtains a condition for the separation constant:

$$J_1(\lambda_n)\, Y_1(\lambda_n k) = J_1(\lambda_n k)\, Y_1(\lambda_n)$$

The general solution is a superposition of all these solutions:

$$\phi_{tr}(\xi,\tau) = \sum_{n=1}^{\infty} C_n \exp\left(-\lambda_n^2\tau\right) Z(\lambda_n\xi) \tag{2.20}$$

In which $C_n = A_n/Y_1(\lambda_n k)$and:

$$Z(\lambda_n\xi) = Y_1(\lambda_n k)\, J_1(\lambda_n\xi) - J_1(\lambda_n k)\, Y_1(\lambda_n\xi) \tag{2.21}$$

To obtain the values for λ_n the Bessel functions can be approximated, for $z > 1$ as [9]:

$$\begin{array}{l} J_1(z) \approx \sqrt{\frac{2}{\pi z}}\cos\left(z - \frac{\pi}{2} - \frac{\pi}{4}\right) \\ Y_1(z) \approx \sqrt{\frac{2}{\pi z}}\sin\left(z - \frac{\pi}{2} - \frac{\pi}{4}\right) \end{array} \tag{2.22}$$

The approximation is good enough for our purpose. Then one can find λ_n:

$$\lambda_n = \frac{n\pi}{1-k} \quad \text{for} \quad n = 1, 2, ..\infty \tag{2.23}$$

The values for C_n can be obtained from the initial condition Eq.(2.17) which leads to:

$$\phi_\infty(\xi) = \sum_{n=1}^{\infty} C_n Z(\lambda_n \xi)$$

Using the orthogonal properties of the Bessel functions, we multiply both sides by $Z(\lambda_m \xi)\,\xi d\xi$ and then integrate from k to 1. The only term on the right side that contributes is that for which $m = n$. Hence we obtain:

$$C_n = \frac{\pi J_1(\lambda_n)\left[(1-\alpha) J_1(\lambda_n k) + \alpha k J_1(\lambda_n)\right]}{J_1^2(\lambda_n k) - J_1^2(\lambda_n)}$$

The final expression for the unsteady state velocity profile reads:

$$\phi(\xi, \tau) = \phi_\infty(\xi) - \phi_{tr}(\xi, \tau)$$

where the steady-state solutions is:

$$\phi_\infty(\xi) = \left[\frac{1-\alpha\left(1-k^2\right)}{1-k^2}\right]\xi - \left[\frac{k^2}{1-k^2}\right]\xi^{-1}$$

and the transient function is given by:

$$\begin{aligned}\phi_{tr}(\xi, \tau) &= \pi \sum_{n=1}^{\infty} \frac{J_1(\lambda_n)\left[(1-\alpha) J_1(k\lambda_n) + \alpha k J_1(\lambda_n)\right]}{J_1^2(k\lambda_n) - J_1^2(\lambda_n)} \\ &\quad \times \left[Y_1(k\lambda_n) J_1(\xi\lambda_n) - J_1(k\lambda_n) Y_1(\xi\lambda_n)\right] \exp\left(-\lambda_n^2 \tau\right)\end{aligned}$$

where λ_n has been given by Eq.(2.23). From the above expression the characteristic time t_{ch} for the process can be calculated:

$$t_{\text{ch}} = \frac{(1-k)^2 \rho b^2}{\pi^2 \eta} \quad \text{with} \quad n = 1$$

For the water phase we received $t_{ch} = 45\ s$. We consider here the $n = 1$ mode because that is the slowest mode: $t_n = t_{ch}/n^2$. Figure 2.5 shows how the steady-state will be reached; there the calculated profiles for different times are presented. As one can see indeed the calculated characteristic time is close to the steady state profile.

Increasing the viscosity of the liquid phase will additionally lead to lower characteristic times. In Table 2.1 the characteristic times for all the liquids used in our study are presented: water, water with glycerol (35 wt.%) and pentadecane.

We initially intended to keep the aggregates in the stagnant zone by continuously adjusting the speeds of the cylinders. However due to the long characteristic times in practice it is difficult to keep the aggregates in the stagnant zone. The way the experiments are performed was changed. The aggregate is allowed to rotate slowly in the Couette device. The CCD camera is kept stationary and the aggregate is recorded when it passes the field of view. The rotational speed of the cylinders is set to minimize the velocity of the aggregate.

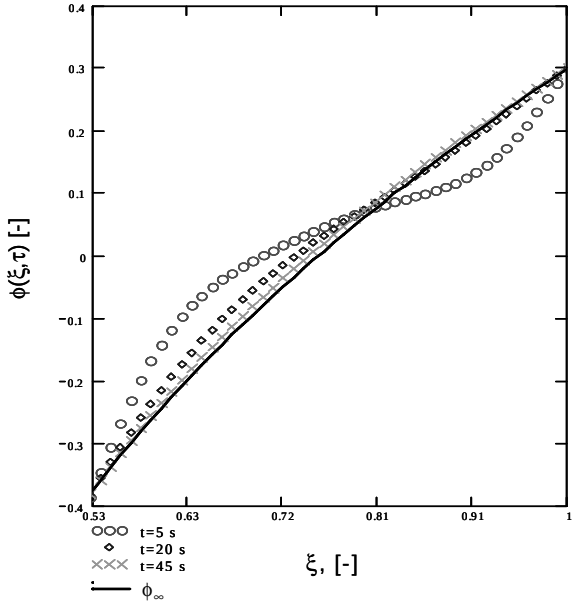

Figure 2.5: *Calculated transient velocity profile* $\phi_{tr}(\xi, \tau)$ *for water phase at different times (with circles* $t = 5$ *s, with rhombs* $t = 20$ *s and with crosses* $t = 45$ *s. The steady state profile* $\phi_{\infty}(\xi)$ *is presented with the black line. The parameters used for the calculations are:* $k = 0.53$, $\rho = 1000$ *kg/m*^{3}, $\varpi_a = 7$ *rpm,* $\varpi_b = -3$ *rpm and* $n = 19$.

System	ρ, kg/m^3	η, mPas	t_{ch}, s
Water	1000	1	45
Water+Gly	1090	2.34	21
Pentadecane	773	2.34	15

Table 2.1: *Calculated characteristic times*

The two cylinders are driven by ribbed belts from two permanent magnet D.C. servo-motors. The motor speeds are controlled from a personal computer. The actual rotation speeds were measured independently and compared with the computer digital read out. It was found that they coincide very well. The results are presented in Figure 2.6 where ω_m is the measured angular velocity in rpm and ω_d is the digital read-out. The open circles correspond to the outer cylinder and the solid rhombs to the inner cylinder. It was found that the measured and the displayed angular velocity coincide quite well. For the rotational speeds used in the experiments (less than 15 rpm) the error is less than 2 %.

2.4 Calculating the shape of the interface

The behavior of the aggregate is determined by the forces acting on the particles, hence it is important to know which forces are present. A key issue related to this is the shape

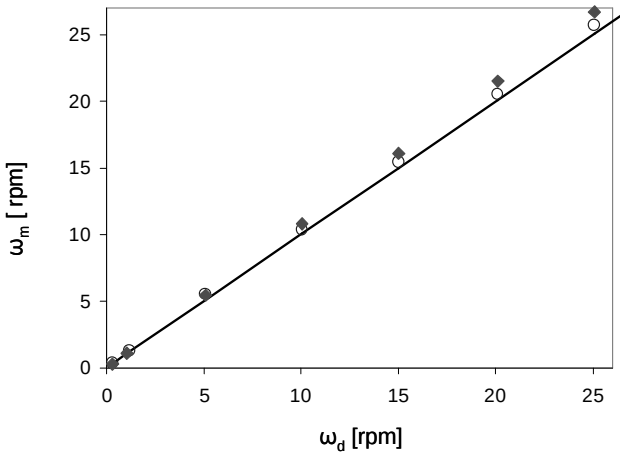

Figure 2.6: *Measured independently* (ω_m) *versus digital read-out* (ω_d) *cylinder speeds in rpm. The speed of the outer cylinder is given with open circles and the speed of the inner with solid rhombs.*

of the interface, since this may add an extra force to the system due to its curvature. Therefore it is important to know the interface shape and control it in the experimental system. In the next sections we calculate this interface shape and present a method to control and measure it.

We have an interface between two concentric cylinders with radii a and b (see Figure 2.7a). The three phase contact angles where the interface meets the cylinders walls are noted as θ_a and θ_b . In the most general case $\theta_a \neq \theta_b$. To calculate the interface profile one has to consider the forces acting upon an annulus of liquid containing the interface. The cylindrical shell has a radius r, thickness dr and height h. In Figure 2.7b the free body diagram of the liquid annulus and the acting forces are depicted. There are two forces present in the system: the net force due to the hydrostatic pressure and the interfacial tension force. We consider here only the vertical component of these forces. For the interfacial tension force we can write:

$$F_z^{(\gamma)} = 2\pi\gamma\left[(r+dr)\sin\beta(r+dr) - r\sin\beta(r)\right]$$

while the hydrostatic pressure force is given by:

$$F_z^{(p)} = 2\pi r dr\left[P_2 - P_1 - g\rho_u\left(h-z\right) - g\rho_l z\right]$$

where ρ_u and ρ_l are the density of the upper and the lower liquid phase, γ is the interfacial tension force, ϕ is the interface slope angle, g is the gravitation acceleration and P_1 and P_2 the hydrostatic pressure at the top and the bottom surface of the elementary cylindrical shell with radius r thickness dr and height h. Since the net force on this shell should be zero, one receives:

$$\frac{1}{r}\frac{d}{dr}\left(r\sin\phi\left(r\right)\right) = \frac{\rho_u g h + P_1 - P_2}{\gamma} + \frac{g\Delta\rho\, z}{\gamma} \tag{2.24}$$

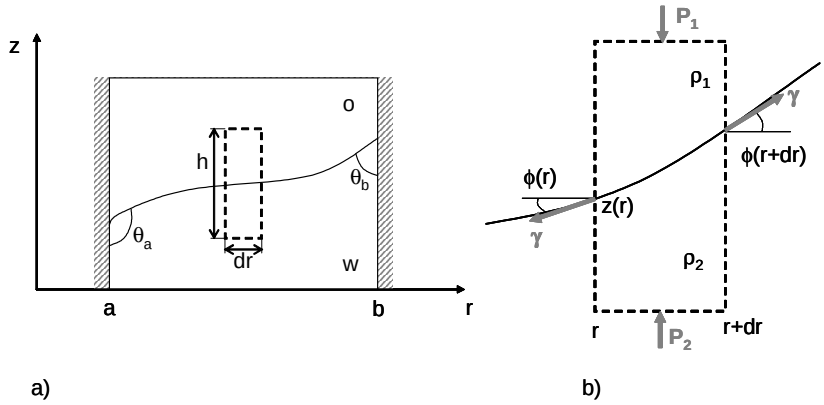

Figure 2.7: *a) A sketch of an interface in the gap between two concentric cylinders. With a and b are denoted the inner and outer cylinder radii and with θ_a and θ_b the contact angles at the walls. With the dashed line is presented the elementary volume with thickness dr and height h. b) A magnified sketch of the elementary volume used for the balance of forces. The interface is described with $z = z(r)$, ρ_1 and ρ_2 are the density of the upper and the lower liquid phase, γ is the interfacial tension force, $\phi(r)$ is the interface slope angle and P_1 and P_2 the hydrostatic pressure at the top and the bottom surface of the elementary volume.*

with $\Delta\rho = \rho_l - \rho_u$. If the interface between the two liquid is defined by $z = z(r)$, then $dz/dr = z' = \tan\phi$ and $\sin\phi = z'(1 + (z')^2)^{-3/2}$. Substitution in Eq. (2.24) gives:

$$\frac{z''}{\left(1 + (z')^2\right)^{3/2}} + \frac{z'}{r\left(1 + (z')^2\right)^{1/2}} = \alpha + \beta z \tag{2.25}$$

where $\alpha = (\rho_u g h + P_1 - P_2)/\gamma$ and $\beta = (g\Delta\rho)/\gamma$ are constants. This equation is the so called Young-Laplace equation [10] which describes a curved interface.

The boundary conditions read:

$$z' = \tan(\theta_a - \frac{\pi}{2}) \quad \text{at} \quad r = a \tag{2.26}$$

$$z' = -\tan(\theta_b - \frac{\pi}{2}) \quad \text{at} \quad r = b \tag{2.27}$$

If we scale every length on a:

$$\tilde{r} = \frac{r}{a}, \quad \tilde{z} = \frac{z}{a}, \quad \tilde{z}' = \frac{d\tilde{z}}{d\tilde{r}} = z', \quad \tilde{z}'' = \frac{d^2\tilde{z}}{d\tilde{r}^2} = az''$$

we can rewrite Eq. (2.25) in dimensionless form:

$$\frac{\tilde{z}''}{(1 + \tilde{z}'^2)^{3/2}} + \frac{\tilde{z}'}{\tilde{r}\,(1 + \tilde{z}'^2)^{1/2}} = \tilde{\alpha} + \tilde{\beta}\tilde{z} \tag{2.28}$$

with $\tilde{\alpha} = a\alpha$ and $\tilde{\beta} = a^2\beta$. The new constant $\tilde{\beta}$ is the so called Bond number Bo which is a dimensionless constant that quantifies the ratio between gravity and capillary forces:

$$Bo = \frac{g\Delta\rho\, a^2}{\gamma} = \frac{a^2}{k^2}$$

where $k = \beta^{-1/2}$ is the so-called capillary length.

Eq.(2.28) is a second order nonlinear differential equation that can be solved only numerically. To solve this equation one can write it as a set of two first order differential equations:

$$\begin{aligned} \tilde{z}' &= u \\ u' &= \left(\tilde{\alpha} + \tilde{\beta}\tilde{z}\right)\left(1+u^2\right) - (u/\tilde{r})\left(1+u^2\right) \end{aligned} \tag{2.29}$$

which can be solved using a 4th order Runge- Kutta scheme. The boundary conditions are:

$$\tilde{z}' = \tan(\theta_a - \frac{\pi}{2}) \quad \text{at} \quad \tilde{r} = 1 \tag{2.30}$$

$$\tilde{z}' = -\tan(\theta_b - \frac{\pi}{2}) \quad \text{at} \quad \tilde{r} = b/a \tag{2.31}$$

which is the dimensionless form of Eqs.(2.26, 2.27). Since $\tilde{\alpha}$ is an unknown constant which depends on the vertical position at which $\tilde{z} = 0$ we define:

$$\tilde{z} = 0 \quad \text{at} \quad \tilde{r} = 1 \tag{2.32}$$

Starting with a guess value for $\tilde{\alpha}$ and with boundary conditions Eqs.(2.30, 2.32), the profile is calculated and from that the value of $\tilde{z}'$ at $\tilde{r} = b/a$ is received. This value is compared with its real value, Eq.(2.31), and $\tilde{\alpha}$ is optimized until both values become equal:

$$\left| \tilde{z}'\,(b/a) + \tan(\theta_b - \frac{\pi}{2}) \right| < \varepsilon$$

within the computational precision ε.

In Figure 2.8 the results from these calculations are presented. An interface between water and pentadecane. was considered ($\rho_u = 773$ kg/m^3, $\rho_l = 1000$ kg/m^3 and $\gamma = 0.052$ N/m). For simplicity $\theta_a = \theta_b$ is taken. The contact angle varies between 10° and 90°. The wetting properties of the cylinder surfaces in general will lead to a curved interface. It is difficult to achieve a flat interface by varying only the physicochemical properties of the system (ρ_u, ρ_l and γ) or the geometrical characteristic of the apparatus (radii a, b and the gap width $(b-a)$). The most efficient way to obtain a flat interface is to pin the contact angle at the cylinder surface to 90°. Therefore the Couette apparatus has been modified. Figure 2.9 illustrates the modification. Both cylinders have a hydrophilic (Steel) lower part and a hydrophobic (Perspex) upper part. The transition between the two parts will act as a pinning line for the interface between the hydrophilic and the hydrophobic liquid (e.g. water and oil). Once the interface has been pinned, the contact angle at the cylinders walls can be adjusted to 90° by controlling the amount of the lower liquid.

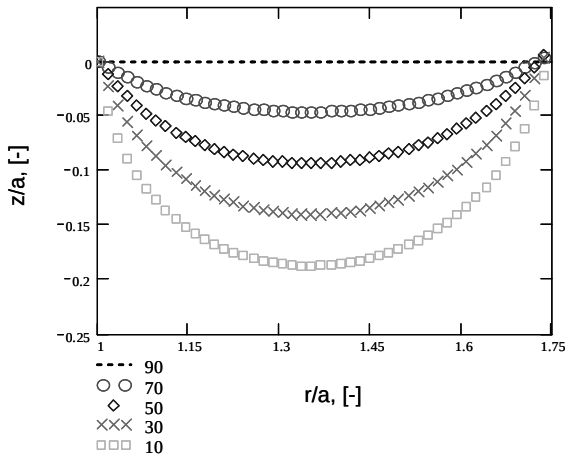

Figure 2.8: *Interface profile $z(r)$ for different contact angles at the cylinders walls. In all cases $\theta_a = \theta_b$, the dash line corresponds to $\theta_a = 90°$, the circles to $\theta_a = 70°$, the rhombs to $\theta_a = 50°$, the crosses to $\theta_a = 30°$ and the squares to $\theta_a = 10°$. The parameters used in the calculations are for a water/pentadecane interface: $\rho_1 = 773$ kg/m^3, $\rho_2 = 1000$ kg/m^3, $\gamma = 0.052$ N/m.*

2.5 Measurement of the local curvature of the interface

In the previous section it was shown that it is important to have a contact angle of 90° at the cylinders walls. It was reached in practice by making the cylinder surfaces from two different materials; on their transition the interface will pin. To achieve a flat interface we need to control the amount of lower liquid added, and so we need a method to measure the interface shape. Below this method for measuring the interface shape is described.

2.5.1 Principle of the measurement

When a narrow light beam passes through the interface, its propagation direction will change due to refraction, if the beam is not perpendicular to the interface. In Figure 2.10 the principle is illustrated. In the first case the beam is perpendicular to the interface and not changing direction passing through it. In the second case the beam is not perpendicular and changes direction after passing the interface. If the incoming beam is oriented perpendicular to the ideal flat interface, then the deviation of the outgoing beam will be a measure of the interface slope at that position. The angle of incidence of the beam is denoted as θ_1 and it is also equal to the slope of the interface at that point. Due to the difference in the refractive index the beam will be shifted to direction θ_2 after the interface. From Snell's refraction law the propagation direction of the outgoing beam relative to the interface is given by:

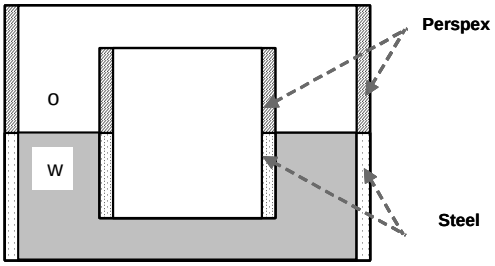

Figure 2.9: *Illustration of pinning of the interface. To the walls of the cylinders rings with different wetting properties are attached. The bottom part is from steel (hydrophilic) and the upper is from Perspex (hydrophilic material).*

$$\theta_2 = \arcsin\left(\frac{n_1}{n_2}\sin\theta_1\right) \tag{2.33}$$

where n_1 and n_2 are the refractive indices relative to vacuum of the lower and upper liquid phase. We can measure the deviation d of the beam from a reference point (chosen at $\theta_1 = 0°$) at distance h from the interface. Then one obtains via geometrical arguments:

$$\tan(\theta_2 - \theta_1) = \frac{d}{(h-z)} \tag{2.34}$$

where z is the deflection of the interface; it is the difference of the vertical positions of the flat and the curved interface. Combining Eqs.(2.33) and (2.34) one can receive an expression for the interface slope angle θ_1:

$$\arcsin\left(\frac{n_1}{n_2}\sin\theta_1\right) - \theta_1 = \arctan\left(\frac{d}{h-z}\right) \tag{2.35}$$

In this form we still can not determine θ_1 because the displacement z is not known.

However if we take the distance h much larger than z , then Eq.(2.35) can be approximated as:

$$\arcsin\left(\frac{n_1}{n_2}\sin\theta_1\right) - \theta_1 = \arctan\left(\frac{d}{h}\right) \qquad \text{for } z \ll h \tag{2.36}$$

and we have a method to determine the interface slope θ_1 at the position of the laser beam.

From the last equation the accuracy of the method can be estimated as $\Delta\theta_1 = (\partial\theta_1/\partial d)\,\Delta d$. For a typical situation with $\Delta d = 1$ mm and $n_1 = 1.33$ (water), $n_2 = 1$ (air) and $h = 1\ m$, one obtains $\Delta\theta_1 = 0.17°$. Thus the method is very accurate.

2.5.2 Experimental verification of the method

To test the method described in last section, a model setup was used as substitution of the real Couette device. This model setup allows simpler measurements and calculations. It consists of a glass Petri dish filled with water. Using the top edge of the dish for

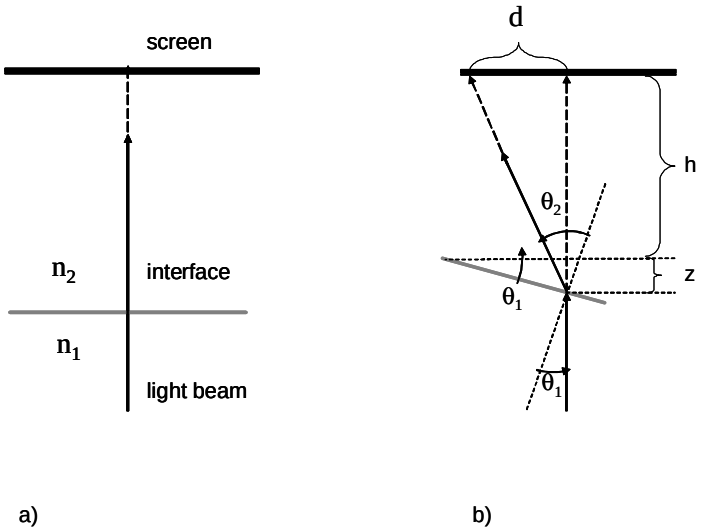

Figure 2.10: *Illustration of the method for measuring the interface shape. a) When the beam is perpendicular to the interface there is no radial shift in its position after the interface. b)When the beam is not perpendicular to the interface (which corresponds to a curved interface), it will refract at different angle after the interface.* θ_1 *is the angle of incidence of the beam,* θ_2 *is the angle of refraction,* d *is the shift in the beam position at a certain distance* h *after the interface and* z *is the interface deflection.*

pinning of the w/a interface, one can control the interface in the same way as in the real experimental setup by using hydrophilic/hydrophobic separation (see Figure 2.11). The set-up has been leveled in order to avoid a nonsymmetrical shape of the meniscus.

A He-Ne laser was placed under the dish in such way that the beam crosses the bottom of dish perpendicularly, close to the rim of the dish where the interface slope is steeper and the refraction of the beam at the liquid-air interface will be large. The position of the spot of the laser beam, using an empty dish, at a distance $h = 1$ m above the dish, is marked as a reference point. This position corresponds to a beam refracting from a flat interface. Next a known volume of water is poured in the dish until it protrudes over the edge and forms a convex (curved upwards) meniscus. The deflection d of the beam at height h from the reference point (zero position) is measured. In the next step a known small volume of water is removed by means of a pipette and the deflection is measured again. This is repeated until the meniscus curvature visibly becomes concave (curved down). The experiment is repeated three times in order to judge the reproducibility of the method. The collected data is presented in Figure 2.12 as the shift in the radial position d versus the corresponding volume of water in the dish V. Since the interface curvature is the cause of the shift, the volume corresponding to a flat interface is at $d = 0$. It was found that a flat interface corresponds to $V_{flat} = 25.45 \pm 0.21$ ml. Based on the dimensions of the Petri dish we can verify the volume of the dish that corresponding to flat interface: $V_{flat} = \pi R_{dish}^2 H_{dish} = 25.5$ ml. This is in agreement with the measured value. From the test performed in the Petri dish we have seen that the method gives good estimation of the interface flatness. The advantages of the method are: it is fast

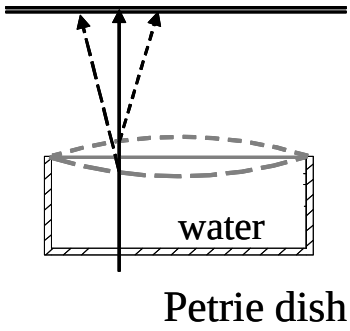

Figure 2.11: *Illustration of the model setup for testing the laser refraction from an interface.*

and accurate, the disadvantage is: it measures the interface slope only at one point and not the whole interface curvature.

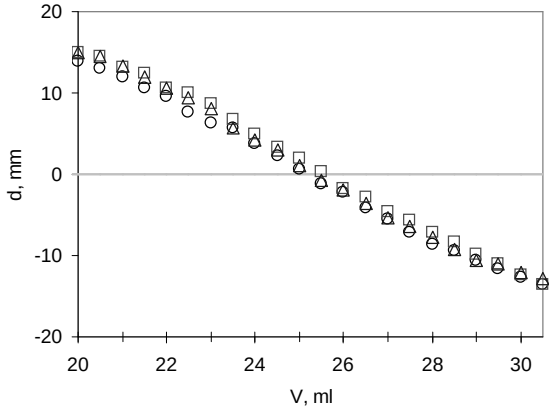

Figure 2.12: *Measured shift d in the radial position of the beam spot plotted against the corresponding water volume V.*

2.5.3 Implementation in the experimental setup

The experimental setup with the laser implemented is depicted in Figure 2.13. The bottom of the outer cylinder is made from glass. A narrow laser beam (He-Ne) passes through it and is transmitted across the interface. The direction of the beam is parallel with the cylinder surfaces and it is positioned close to the outer cylinder where the interface slope is the steepest. The beam passes the Couette device, travels a long distance in the air (1.5 m) and reaches a perpendicular screen. As a reference point for the measurements the position of the beam on the screen with an empty Couette device is taken. This point corresponds also to a flat interface and it also compensates for errors coming from

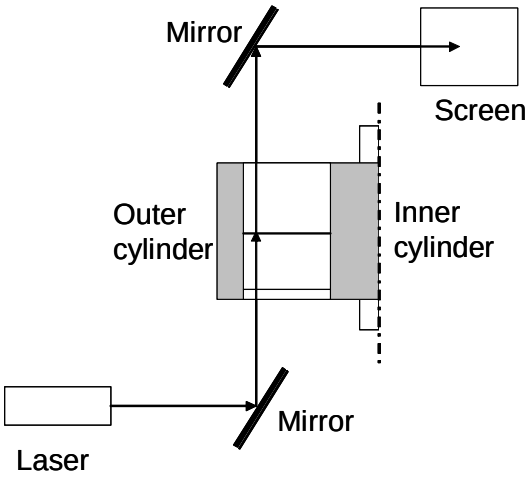

Figure 2.13: *Measuring of the interface shape in the experimental setup.*

refraction of the laser beam in the glass bottom. The lower phase is poured in the device. We add/remove small quantities of water while checking on the screen the deflection of the beam from the reference point. At the moment they coincide we have flat w/a interface. Then the upper liquid phase can be added. Due to the pinning of the contact line at the hydrophilic/hydrophobic transition of the cylinders, the w/o interface remains flat.

2.6 Summary

In this chapter the flow properties in our Couette geometry were investigated. From the results it can be concluded that the experimental device is suited to study the deformation and break-up of 2D aggregates. It is important to realize that shear rate in the gap is not a constant. The variation of the shear rate over the aggregate has to be taken into account. Possible deviations due to end effects or flow instabilities were found to be insignificant. Also, a simple model for the adaptation time of the flow field to changes of the cylinder speeds has been presented. The transient flow profiles at different times were calculated. The characteristic time for reaching the steady-state profile for the water phase is 45 s. Due to this long response time we are not able to keep the aggregate under investigation in the field of view of the CCD camera but we allow for a slow rotation of the aggregate. The camera is kept stationary and the aggregate is observed when it passes through its field of view.

To prevent the appearance of an extra force on the particles due to the interface curvature the liquid-liquid interface should be completely flat. To this end we modified the Couette device in order to be able to control the interface shape. First, a hydrophilic/hydrophobic transition at the cylinder surfaces was created, where the interface can be pinned. Second, by optimizing the amount of lower liquid and checking the interface slope by laser beam refraction, a flat interface is achieved.

References

[1] Van de Ven, T. G. M. *Colloidal hydrodynamics*, Academic Press: London, **1989**.

[2] de Haas K.H.,van den Ende D. et al., *Review of scientific instruments*, **1998**, 69 (3), 1391.

[3] R.A. de Bruin, *Ph.D. thesis.*

[4] Macosko C.W., *Rheology:Principles, Measurements, and Applications,* Wiley-VCH, **1994**.

[5] Ferguson J., Kemblowski Z., *Applied fluid rheology*, Elsevier, **1991**.

[6] Bird R.B., Warren E., *Transport phenomena, **2002**.*

[7] Bird R.B., *Chem. Eng. Sci.*, **1959**, 11, 108.

[8] Bronshtejn I.N., *Mathematical handbook*, **1986** (in Russian).

[9] Janke E. and Emde F., *Funktionentafeln, **1938**.*

[10] Princen H.M. The equilibrium shape of interfaces, drops and bubbles. Rigid and deformable particles at interfaces Surface and colloid science, vol. 2 (Matijevic E.,Ed.), Interscience, New York, **1969**.

[11] Douglas J., Gasiorek J., *Fluid mechanics*, Pearson education, **2001**.

Chapter 3

Interface profile around a single particle and capillary force between two particles

Abstract

In this chapter we investigate the influence of a spherical particle trapped at a liquid-liquid interface on the interface profile. Moreover, the capillary interaction between two particles at the interface is calculated based on the interface profile around these particles. Special attention is paid to the boundary conditions along the tpc-line on the particle surface, in relation to the wetting angle at contact.

3.1 Introduction

In this chapter we investigate particles at the interface without applying a shear flow to the system. The starting point for this investigation is the behavior of a singe particle trapped at the interface. In the first section we describe the interface profile around a single spherical particle. We are interested in the deformation of the profile caused by the particle. If there are more particles present that deformation will give rise to a capillary interaction force between them.

The capillary interaction between particles is usually calculated using the linear superposition approximation (LSA), which states that the total deformation of the interface is determined by superposition of the deformations due to the individual particles [1]. It is valid for not too close distances between the particles. For close distances the correct boundary conditions will be violated and this results in a wrong calculation of the interaction force. This is the case for particles in a dense aggregate as in our experiments. In the present chapter we presented a method to calculate the exact interaction force. Here we will consider only the interactions between two particles. Before we do so, first the exact boundary conditions for the three phase contact line on a wall, a cylinder and finally a sphere are derived. Once the boundary conditions are known, the interface profile can be calculated by solving the Young-Laplace equation, that can be linearized in very good approximation for the particles considered in this thesis. In the last section the interaction force between two spherical particles will be derived. This chapter serves

as an introduction to the theory describing the interactions between multiple particles, which is presented in chapter 4.

3.2 Description of the interface near a single particle

Our solid particles approach the interface under the influence of gravity. Depending on the size of the particle, the density ratio and the interface nature, the particles can pass the interface or stay trapped there. When the density of the particle ρ_p is intermediate between the densities of the two liquid phases ($\rho_l > \rho_p > \rho_u$), the particle will always be trapped at an equilibrium position in the interface. When ρ_p is greater than either ρ_l, the particle still can be supported at the interface by interfacial tension forces [2], [3].

We consider a spherical particle at a fluid interface with a density ρ_p and a radius R_p, where the interface meets the solid surface at a contact angle α_c (measured through the lower fluid). This angle is determined by the wetting properties of the particle. The situation is depicted in Figure 3.1. The interface is formed between the lower fluid with density ρ_l and upper fluid with density ρ_u, the interfacial tension between them is γ. Near the particle the interface is curved and far from the particle it is planar. Also, the particle surface is considered to be homogeneous and smooth. The vertical distance between the planar interface and the contact line is ζ_c and between the planar interface and the center of the particle ζ_m. The angle β is the angle between the vertical and the radius to the line where the interface meets the surface of the sphere, i.e. the three phase contact (tpc-) line. The angle $\psi = (\alpha_c - \beta)$ is the angle between the horizontal and the tangent of the meniscus at the tpc-line.

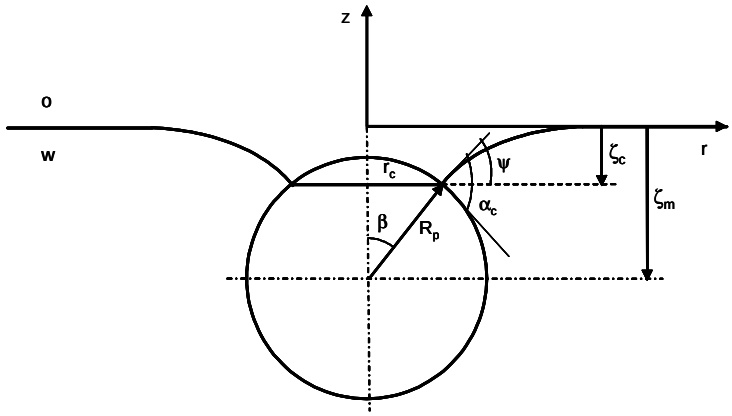

Figure 3.1: *Sketch of a single particle at the interface.*

The simplest way to determine the position of a particle at a liquid-liquid interface is to make an analysis of the forces acting on the particle. There are three distinct vertical forces present. The vertical component of the interfacial tension force:

$$\underline{F}_\gamma = 2\pi\gamma R_p \sin\psi \sin\beta \underline{e}_z \tag{3.1}$$

The gravitational force:

$$\underline{F}_g = -\frac{4}{3}\pi R_p^3 \rho_p g \underline{e}_z \tag{3.2}$$

where g is the gravitation acceleration.

The third force is the buoyancy force:

$$\begin{aligned}\underline{F}_b &= -\int_0^{2\pi}\int_0^{\pi} P(z)\,\underline{e}_r R_p^2 \sin\theta d\theta d\phi \\ &= -2\pi R_p^2 \left(\int_0^{\beta} P_u(z)\cos\theta\sin\theta d\theta + \int_{\beta}^{\pi} P_l(z)\cos\theta\sin\theta d\theta\right)\underline{e}_z\end{aligned}$$

with the pressure in the upper and lower phase given by:

$$\begin{aligned}P_u(z) &= P_0 - g\rho_u z \\ P_l(z) &= P_0 - g\rho_l z\end{aligned}$$

where P_0 is the pressure far from the particle at the planar interface where $z = 0$. Additionally, for a point on the particle surface, z can be expressed as:

$$z = \zeta_m + R_p\cos\theta$$

where: $\zeta_m = \zeta_c - R\cos\beta$. The final expression for buoyancy force is:

$$\begin{aligned}F_{b,z} &= \frac{2}{3}\pi R_p^3 g\Delta\rho\cos^3\beta + \frac{2}{3}\pi R_p^3 g(\rho_l+\rho_u) \\ &\quad -\pi R_p^2\xi_m g\Delta\rho\sin^2\beta\end{aligned} \tag{3.3}$$

where $\Delta\rho = \rho_l - \rho_u$. The equilibrium condition for the vertical forces yields: $\sum F = F_\gamma + F_g + F_b = 0$ or:

$$\begin{aligned}&\left(\cos\beta - \tfrac{1}{3}\cos^3\beta\right) + \frac{2\left(\rho_l+\rho_u-2\rho_p\right)}{3\Delta\rho} \\ &-\frac{\zeta_c}{R_p}\sin^2\beta - \frac{2}{\left(qR_p\right)^2}\sin\beta\sin(\beta-\alpha_c) = 0\end{aligned} \tag{3.4}$$

where $q = \sqrt{g\Delta\rho/\gamma}$ is the so-called reciprocal capillary length. There are two unknown parameters: ξ_c and β. Hence we need a second equation to obtain a solution. To this end we consider the profile of the interface $z(r)$ near the particle. To calculate the profile one has to solve the Young-Laplace equation (see section 4 of Chapter 2):

$$\frac{1}{r}\frac{d}{dr}\left(r\frac{dz/dr}{\sqrt{1+\left(dzdr\right)^2}}\right) = q^2 z \tag{3.5}$$

This equation can be derived from a force balance considering the vertical forces acting on a hypothetical cylindrical liquid annulus around the particle, similar to the analysis in Chapter 2. It is a second order nonlinear partial differential equation but it can be simplified under some assumptions. It was proven by Chan et al. [4] that when the Bond number ($Bo = Rp^2q^2$) is small ($Bo \ll 1$), the meniscus slope is small, too (small meniscus deformation), i.e. $(dz/dr)^2 \ll 1$. In this case one can linearize Eq. (3.5) and an analytical expression for ξ_c can be obtained:

$$\frac{1}{r}\frac{d}{dr}\left(r\frac{dz}{dr}\right) = q^2 z \tag{3.6}$$

Eq.(3.6) is a Bessel equation that has an analytical solution:

$$z(r) = aI_0(qr) + bK_0(qr) \tag{3.7}$$

where I_0 and K_0 are the modified Bessel functions of the first and second kind, both of zeroth order. The boundary conditions for Eq.(3.7) are determined by the meniscus that has to meet the particle surface at a well defined angle and becomes flat at infinity:

$$\frac{dz}{dr} = \sin(\alpha_c - \beta) \quad \text{at} \quad r = R_p \sin\beta \tag{3.8}$$

$$z = 0 \quad \text{at} \quad r \to \infty \tag{3.9}$$

With these boundary conditions the solution reads:

$$z(r) = \frac{\zeta_c K_0(qr)}{K_0(qR_p \sin\beta)} \tag{3.10}$$

where ζ_c is determined by:

$$\left.\frac{dz}{dr}\right|_{R_p \sin\beta} = \sin(\alpha_c - \beta) = -k\zeta_c \frac{K_1(qR_p \sin\beta)}{K_0(qR_p \sin\beta)} \tag{3.11}$$

From the last equation together with Eq. (3.4) the following set of equations is formed:

$$\begin{aligned} \left(\cos\beta - \tfrac{1}{3}\cos^3\beta\right) + \frac{2\left(\rho_l + \rho_u - 2\rho_p\right)}{3\Delta\rho} \\ -\frac{\zeta_c}{R_p}\sin^2\beta - \frac{2}{(qR_p)^2}\sin\beta\sin(\beta - \alpha_c) \end{aligned} = 0 \tag{3.12}$$

$$\sin(\alpha_c - \beta) K_0(qR_p \sin\beta) + q\zeta_c K_1(qR_p \sin\beta) = 0$$

Now the values for ζ_c and β can be determined for given ρ_l, ρ_u, ρ_p, R_p, γ and α_c. It was checked that for all cases of interest indeed $(dz/dr)^2 \ll 1$. In Table 3.1 the results for ζ_c and β are presented for glass particles at a water/air (w/a) and a water/oil (w/o) interface. The particles considered have a radius $R_p = 115\ \mu m$ and a density $\rho_p = 2480$ kg/m^3. As one can see $\alpha_c \approx \beta$ for our case and thus the position of the particle at the interface is determined by the contact angle α_c. In Figure 3.2 the calculated interface profile, using Eq.(3.10), is shown.

System	γ mN/m	$\Delta\rho$ kg/m^3	q^{-1} mm	α_c	β	ζ_c μm
Water/Air/Glass	71	1089	2.6	55°	54.9°	-0.73
Water/Oil/Glass	44	317	3.8	40°	39.7°	-1.28

Table 3.1: *Calculated interface parameters for glass particles at w/a and w/o interface.*

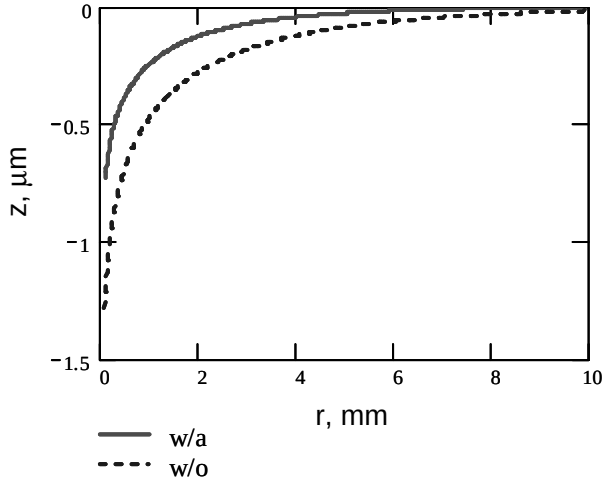

Figure 3.2: *Calculated interface profile for a glass particle with* $R_p = 115$ μm *and density* $\rho_p = 2480$ kg/m^3. *Two cases are considered w/a interface (with solid line) and w/o interface (with dashed line). The input parameters are shown in Table 3.1.*

3.3 Description of the interface slope near a three phase contact line

For two particles in close proximity their interface profiles will overlap which leads to a non flat tpc-line along the particles. The situation is depicted in Figure 3.3 for two similar spheres. In that case the boundary conditions are a more complicated function of the interface slope. Below the correct boundary conditions will be calculated We start with the simplest case of an interface meeting a flat wall, followed by an interface meeting a cylinder and, eventually, a sphere.

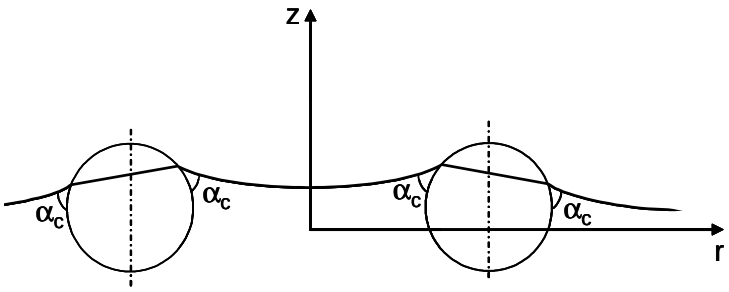

Figure 3.3: *Overlap of the interface profiles of two particles.*

3.3.1 Flat wall geometry

Suppose the liquid-liquid interface contacts a solid wall, in the $\underline{e}_y$-$\underline{e}_z$ plane, at the origin of a Cartesian coordinate system, while the interface is described by

$$z = f(x, y)$$

The interface has an arbitrary shape. The slope of the three phase contact line (tpc-line) along the wall is given by $\tan\phi = \partial f/\partial y = f_y$. A second orthogonal coordinate system is introduced to describe the contact angle and the resulting surface tension force on that wall:

$$\begin{aligned} \underline{e}_\xi &= \underline{e}_x \\ \underline{e}_\eta &= \cos\phi\,\underline{e}_y + \sin\phi\,\underline{e}_z \\ \underline{e}_\zeta &= -\sin\phi\,\underline{e}_y + \cos\phi\,\underline{e}_z \end{aligned}$$

In Figure 3.4 the two coordinate systems are presented. The direction $\underline{e}_\eta$ has been chosen tangential to the tpc-line in point P.

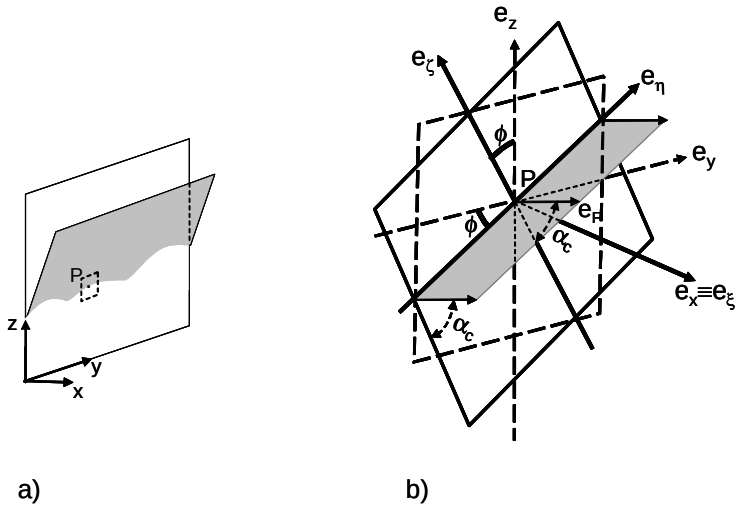

Figure 3.4: *A sketch of the coordinate systems used to describe an arbitrary interface meeting a flat wall. a) shows the wall while b) is a close look of the surface element at position P. With grey color is presented the interface surface.*

In the new coordinate system the interface is described by

$$\zeta = g(\xi, \eta)$$

and the contact angle α_c is given by

$$\tan(\alpha_c - \pi/2) = \partial g/\partial\xi = g_\xi \tag{3.13}$$

In order to express α_c in the (x, y, z) coordinates we compare the representation of the displacement $d\underline{\mathrm{r}}$ in both coordinate systems:

$$\begin{aligned} d\underline{\mathrm{r}} &= dx\,\underline{\mathrm{e}}_x + dy\,\underline{\mathrm{e}}_y + (f_x dx + f_y dy)\,\underline{\mathrm{e}}_z \\ &= dx\,\underline{\mathrm{e}}_\xi + dy\left(\cos\phi\,\underline{\mathrm{e}}_\eta - \sin\phi\,\underline{\mathrm{e}}_\zeta\right) \\ &\quad + (f_x dx + f_y dy)\left(\sin\phi\,\underline{\mathrm{e}}_\eta + \cos\phi\,\underline{\mathrm{e}}_\zeta\right) \\ &= dx\,\underline{\mathrm{e}}_\xi + ((f_x dx + f_y dy)\sin\phi + dy\cos\phi)\,\underline{\mathrm{e}}_\eta \\ &\quad + ((f_x dx + f_y dy)\cos\phi - dy\sin\phi)\,\underline{\mathrm{e}}_\zeta \\ &= d\xi\,\underline{\mathrm{e}}_\xi + d\eta\,\underline{\mathrm{e}}_\eta + dg(\xi,\eta)\underline{\mathrm{e}}_\zeta \end{aligned}$$

Hence:

$$\begin{aligned} d\xi &= dx \\ d\eta &= (f_x dx + f_y dy)\sin\phi + dy\cos\phi \\ dg &= (f_x dx + f_y dy)\cos\phi - dy\sin\phi \end{aligned} \tag{3.14}$$

From last equation we can calculate $\partial g/\partial\xi = g_\xi$:

$$g_\xi = \left(\frac{dg}{d\xi}\right)_{d\eta=0} = \left(\frac{(f_x dx + f_y dy)\cos\phi - dy\sin\phi}{dx}\right)_{d\eta=0} \tag{3.15}$$

From Eq. (3.14) one obtains:

$$dy = \frac{-f_x\sin\phi}{\cos\phi + f_y\sin\phi}dx = \frac{-f_x f_y}{1+f_y^2}dx \tag{3.16}$$

where we have used the following relations:

$$\begin{aligned} \sin\phi &= \frac{\tan\phi}{\sqrt{1+\tan^2\phi}} = \frac{f_y}{\sqrt{1+f_y^2}} \\ \cos\phi &= \frac{1}{\sqrt{1+\tan^2\phi}} = \frac{1}{\sqrt{1+f_y^2}} \end{aligned}$$

Combining Eqs. (3.15) and (3.16) will give:

$$\begin{aligned} g_\xi &= \frac{f_x\left(1+f_y^2\right)\cos\phi\,dx - f_x f_y\left(f_y\cos\phi - \sin\phi\right)dx}{\left(1+f_y^2\right)dx} \\ &= \frac{f_x}{\sqrt{1+f_y^2}} \end{aligned}$$

or finally for the boundary condition on the wall:

$$\tan(\alpha_c - \pi/2) = \frac{f_x}{\sqrt{1+f_y^2}} \tag{3.17}$$

The unit vector $\underline{\mathrm{e}}_F$ in the direction of the surface tension force can be also expressed in the new coordinate system by:

$$\begin{aligned}\underline{\mathrm{e}}_F &= \sin\alpha_c\,\underline{\mathrm{e}}_\xi - \cos\alpha_c\,\underline{\mathrm{e}}_\zeta \\ &= \frac{1}{\sqrt{1+g_\xi^2}}\underline{\mathrm{e}}_x + \frac{g_\xi}{\sqrt{1+g_\xi^2}}\left(\frac{-f_y}{\sqrt{1+f_y^2}}\underline{\mathrm{e}}_y + \frac{1}{\sqrt{1+f_y^2}}\underline{\mathrm{e}}_z\right)\end{aligned}$$

With:

$$\begin{aligned}\frac{1}{\sqrt{1+g_\xi^2}} &= \sqrt{\frac{1+f_y^2}{1+f_y^2+f_x^2}} \\ \frac{g_\xi}{\sqrt{1+g_\xi^2}} &= \frac{f_x}{\sqrt{1+f_y^2+f_x^2}}\end{aligned}$$

one obtains:

$$\underline{\mathrm{e}}_F = \frac{\left(1+f_y^2\right)\underline{\mathrm{e}}_x - f_x f_y \underline{\mathrm{e}}_y + f_x \underline{\mathrm{e}}_z}{\sqrt{\left(1+f_y^2+f_x^2\right)\left(1+f_y^2\right)}} \tag{3.18}$$

and the force due to the surface tension γ along a segment dl of the tpc-line is equal to:

$$\begin{aligned}d\underline{\mathrm{F}}^{[\gamma]} &= \gamma dl \underline{\mathrm{e}}_F \\ &= \gamma\sqrt{\left(1+f_y^2\right)}dy\frac{\left(1+f_y^2\right)\underline{\mathrm{e}}_x - f_x f_y\underline{\mathrm{e}}_y + f_x\underline{\mathrm{e}}_z}{\sqrt{\left(1+f_y^2+f_x^2\right)\left(1+f_y^2\right)}} \\ &= \gamma dy\frac{\left(1+f_y^2\right)\underline{\mathrm{e}}_x - f_x f_y\underline{\mathrm{e}}_y + f_x\underline{\mathrm{e}}_z}{\sqrt{1+f_y^2+f_x^2}}\end{aligned} \tag{3.19}$$

Let's now consider a liquid column with cross section $dxdy$ oriented along the z-axis which crosses the liquid-liquid interface. Then the net force on that column due to surface tension is:

$$\begin{aligned}d\underline{\mathrm{F}}^{[\gamma]} &= d\underline{\mathrm{F}}^{[x]}(x+dx/2,y) - d\underline{\mathrm{F}}^{[x]}(x-dx/2,y) \\ &\quad + d\underline{\mathrm{F}}^{[y]}(x,y+dy/2) - d\underline{\mathrm{F}}^{[y]}(x,y-dy/2) \\ &= \frac{\partial\left(d\underline{\mathrm{F}}^{[x]}(x,y)\right)}{\partial x}dx + \frac{\partial\left(d\underline{\mathrm{F}}^{[y]}(x,y)\right)}{\partial y}dy\end{aligned}$$

with

$$\begin{aligned}d\underline{\mathrm{F}}^{[x]}(x,y) &= \gamma dy\frac{\left(1+f_y^2\right)\underline{\mathrm{e}}_x - f_x f_y\underline{\mathrm{e}}_y + f_x\underline{\mathrm{e}}_z}{\sqrt{1+f_y^2+f_x^2}} \\ d\underline{\mathrm{F}}^{[y]}(x,y) &= \gamma dx\frac{\left(1+f_x^2\right)\underline{\mathrm{e}}_y - f_y f_x\underline{\mathrm{e}}_x + f_y\underline{\mathrm{e}}_z}{\sqrt{1+f_y^2+f_x^2}}\end{aligned}$$

Hence

$$d\underline{\mathrm{F}}^{[\gamma]} = \gamma dxdy \begin{pmatrix} \frac{\partial}{\partial x}\left[\frac{(1+f_y^2)\underline{\mathrm{e}}_x - f_x f_y \underline{\mathrm{e}}_y + f_x \underline{\mathrm{e}}_z}{\sqrt{1+f_y^2+f_x^2}}\right] \\ +\frac{\partial}{\partial y}\left[\frac{(1+f_x^2)\underline{\mathrm{e}}_y - f_y f_x \underline{\mathrm{e}}_x + f_y \underline{\mathrm{e}}_z}{\sqrt{1+f_y^2+f_x^2}}\right] \end{pmatrix} \tag{3.20}$$

or in components:

$$\begin{aligned} dF_x^{[\gamma]} &= \gamma dxdy \left(\frac{\partial}{\partial x}\left[\frac{\left(1+f_y^2\right)}{\sqrt{1+f_y^2+f_x^2}}\right] + \frac{\partial}{\partial y}\left[\frac{-f_y f_x}{\sqrt{1+f_y^2+f_x^2}}\right]\right) \\ dF_y^{[\gamma]} &= \gamma dxdy \left(\frac{\partial}{\partial x}\left[\frac{-f_x f_y}{\sqrt{1+f_y^2+f_x^2}}\right] + \frac{\partial}{\partial y}\left[\frac{\left(1+f_x^2\right)}{\sqrt{1+f_y^2+f_x^2}}\right]\right) \\ dF_z^{[\gamma]} &= \gamma dxdy \left(\frac{\partial}{\partial x}\left[\frac{f_x}{\sqrt{1+f_y^2+f_x^2}}\right] + \frac{\partial}{\partial y}\left[\frac{f_y}{\sqrt{1+f_y^2+f_x^2}}\right]\right) \end{aligned}$$

The force due to gravity and pressure on the column is equal to:

$$dF_z^{[p]} = -dxdy\, g\Delta\rho\, f(x,y)$$

so the force balance in vertical direction reads:

$$\frac{\partial}{\partial x}\left[\frac{f_x}{\sqrt{1+f_y^2+f_x^2}}\right] + \frac{\partial}{\partial y}\left[\frac{f_y}{\sqrt{1+f_y^2+f_x^2}}\right] = \frac{g\Delta\rho}{\gamma} f(x,y) \tag{3.21}$$

which is just the Young-Laplace equation in Carthesisan coordinates.

3.3.2 Cylinder geometry

Suppose the liquid-liquid interface contacts a solid cylinder with its axis oriented in the z-direction, in the $\underline{\mathrm{e}}_\vartheta$-$\underline{\mathrm{e}}_z$ plane, while the interface is described by:

$$z = f(r,\vartheta)$$

The slope of the tpc-line along the cylinder is given by $\tan\phi = \partial f/(r\partial\vartheta) = f_\vartheta/r$. A second orthogonal coordinate system is introduced to describe the contact angle and the resulting surface tension force on the wall:

$$\begin{aligned} \underline{\mathrm{e}}_\xi &= \underline{\mathrm{e}}_r \\ \underline{\mathrm{e}}_\eta &= \cos\phi\, \underline{\mathrm{e}}_\vartheta + \sin\phi\, \underline{\mathrm{e}}_z \\ \underline{\mathrm{e}}_\zeta &= -\sin\phi\, \underline{\mathrm{e}}_\vartheta + \cos\phi\, \underline{\mathrm{e}}_z \end{aligned}$$

Again, $\underline{\mathrm{e}}_\eta$ has been chosen tangential to the tpc-line in point P (Figure 3.5).

In this coordinate system the interface is described by

$$\zeta = g(\xi,\eta)$$

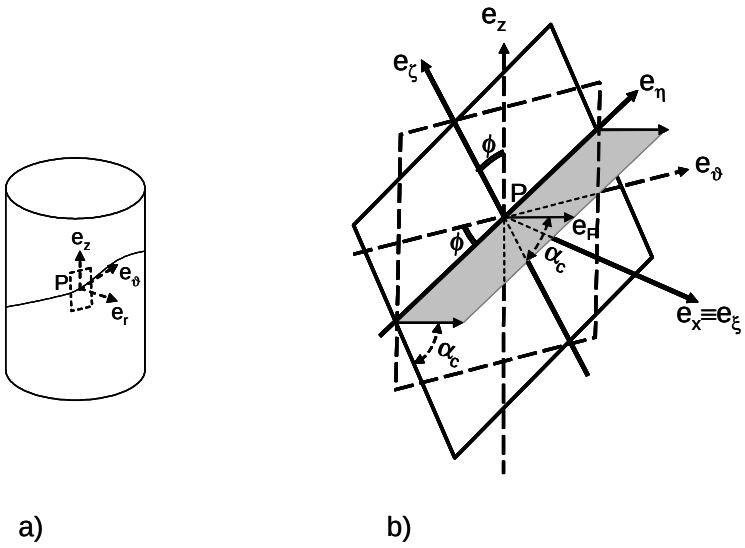

Figure 3.5: *A sketch of the coordinate systems used to describe an arbitrary interface meeting a cylinder. As before a) shows the cylinder while b) is a close look of the surface element at position P. With grey color is shown the interface.*

and the contact angle α_c is given by

$$\tan(\alpha_c - \pi/2) = \partial g/\partial \xi = g_\xi$$

The unit vector in the direction of the surface tension force is expressed by:

$$\underline{\mathrm{e}}_F = \sin\alpha_c\, \underline{\mathrm{e}}_\xi - \cos\alpha_c\, \underline{\mathrm{e}}_\zeta$$

In order to express α_c in the (r, ϑ, z) coordinates we compare the representation of $d\underline{\mathrm{r}}$ in both coordinate systems:

$$\begin{aligned}
d\underline{\mathrm{r}} &= dr\, \underline{\mathrm{e}}_r + rd\vartheta\, \underline{\mathrm{e}}_\vartheta + (f_r dr + f_\vartheta d\vartheta)\, \underline{\mathrm{e}}_z \\
&= dr\, \underline{\mathrm{e}}_\xi + rd\vartheta \left(\cos\phi\, \underline{\mathrm{e}}_\eta - \sin\phi\, \underline{\mathrm{e}}_\zeta\right) \\
&\quad + (f_r dr + f_\vartheta d\vartheta) \left(\sin\phi\, \underline{\mathrm{e}}_\eta + \cos\phi\, \underline{\mathrm{e}}_\zeta\right) \\
&= dr\, \underline{\mathrm{e}}_\xi + (rd\vartheta\cos\phi + (f_r dr + f_\vartheta d\vartheta)\sin\phi)\ \underline{\mathrm{e}}_\eta \\
&\quad + ((f_r dr + f_\vartheta d\vartheta)\cos\phi - rd\vartheta\sin\phi)\ \underline{\mathrm{e}}_\zeta \\
&= d\xi\, \underline{\mathrm{e}}_\xi + d\eta\, \underline{\mathrm{e}}_\eta + dg\, \underline{\mathrm{e}}_\zeta
\end{aligned}$$

Hence

$$\begin{aligned}
d\xi &= dr \\
d\eta &= rd\vartheta\cos\phi + (f_r dr + f_\vartheta d\vartheta)\sin\phi \\
dg &= (f_r dr + f_\vartheta d\vartheta)\cos\phi - rd\vartheta\sin\phi
\end{aligned}$$

From last equation we can calculate $\partial g/\partial\xi = g_\xi$:

$$g_\xi = \left(\frac{dg}{d\xi}\right)_{d\eta=0} = \left(\frac{(f_r dr + f_\vartheta d\vartheta)\cos\phi - rd\vartheta\sin\phi}{dr}\right)_{d\eta=0}$$

Because $d\eta = r d\vartheta \cos\phi + (f_r dr + f_\vartheta d\vartheta)\sin\phi = 0$ one obtains:

$$\begin{aligned}(r\cos\phi + f_\vartheta \sin\phi)\, d\vartheta &= -f_r \sin\phi\, dr \\ d\vartheta &= \frac{-f_r \sin\phi}{r\cos\phi + f_\vartheta \sin\phi} dr \\ &= \frac{-f_r f_\vartheta}{r^2 + f_\vartheta^2} dr\end{aligned}$$

and

$$\begin{aligned}g_\xi &= f_r \cos\phi - (f_\vartheta \cos\phi - r\sin\phi)\, \frac{f_r f_\vartheta}{r^2 + f_\vartheta^2} \\ &= f_r \cos\phi \left(1 - (f_\vartheta - r\tan\phi)\, \frac{f_\vartheta}{r^2 + f_\vartheta^2}\right) \\ &= \frac{r f_r}{\sqrt{r^2 + f_\vartheta^2}}\end{aligned} \tag{3.22}$$

The unit vector $\underline{\mathrm{e}}_F$ now becomes:

$$\begin{aligned}\underline{\mathrm{e}}_F &= \sin\alpha_c\, \underline{\mathrm{e}}_\xi - \cos\alpha_c\, \underline{\mathrm{e}}_\zeta \\ &= \frac{1}{\sqrt{1+g_\xi^2}} \underline{\mathrm{e}}_r + \frac{g_\xi}{\sqrt{1+g_\xi^2}} \left(\frac{-f_\vartheta}{\sqrt{r^2+f_\vartheta^2}} \underline{\mathrm{e}}_\vartheta + \frac{r}{\sqrt{r^2+f_\vartheta^2}} \underline{\mathrm{e}}_z\right)\end{aligned}$$

With:

$$\begin{aligned}\frac{1}{\sqrt{1+g_\xi^2}} &= \sqrt{\frac{r^2+f_\vartheta^2}{r^2+f_\vartheta^2+r^2 f_r^2}} \\ \frac{g_\xi}{\sqrt{1+g_\xi^2}} &= \frac{r f_r}{\sqrt{r^2+r^2 f_r^2+f_\vartheta^2}}\end{aligned}$$

one obtains:

$$\underline{\mathrm{e}}_F = \frac{\left(r^2+f_\vartheta^2\right)\underline{\mathrm{e}}_r - f_\vartheta r f_r \underline{\mathrm{e}}_\vartheta + r^2 f_r \underline{\mathrm{e}}_z}{\sqrt{\left(r^2+f_\vartheta^2+r^2 f_r^2\right)\left(r^2+f_\vartheta^2\right)}} \tag{3.23}$$

and the force due to the surface tension γ along a segment $dl = \sqrt{r^2+f_\vartheta^2}\, d\vartheta$ of the tpc-line is equal to:

$$\begin{aligned}d\underline{\mathrm{F}}^{[\gamma]} &= \gamma dl \underline{\mathrm{e}}_F = \gamma\sqrt{r^2+f_\vartheta^2}\, d\vartheta \frac{\left(r^2+f_\vartheta^2\right)\underline{\mathrm{e}}_r - f_\vartheta r f_r \underline{\mathrm{e}}_\vartheta + r^2 f_r \underline{\mathrm{e}}_z}{\sqrt{\left(r^2+f_\vartheta^2+r^2 f_r^2\right)\left(r^2+f_\vartheta^2\right)}} \\ &= \gamma d\vartheta \frac{\left(r^2+f_\vartheta^2\right)\underline{\mathrm{e}}_r - f_\vartheta r f_r \underline{\mathrm{e}}_\vartheta + r^2 f_r \underline{\mathrm{e}}_z}{\sqrt{r^2+f_\vartheta^2+r^2 f_r^2}}\end{aligned} \tag{3.24}$$

If one considers a cylinder with radius R immersed in the liquids, the interface slope near the cylinder is related to the contact angle by Eq.(3.22):

$$\cot(\alpha_c) = -\tan(\alpha_c - \pi/2) = \left.\frac{-r\,(\partial\zeta/\partial r)}{\sqrt{r^2 + (\partial\zeta/\partial\vartheta)^2}}\right|_{r=R} \tag{3.25}$$

3.3.3 Spherical geometry

Suppose the liquid-liquid interface contacts a solid sphere, in the $\underline{e}_\vartheta$-$\underline{e}_\beta$ plane, while the interface, expressed in cylindrical coordinates (r, ϑ, z), is described by:

$$z = f(r, \vartheta)$$

The interface near the sphere expressed in spherical coordinates (R, ϑ, β) is given by:

$$\beta = h(R, \vartheta)$$

The slope of the tpc-line along the sphere is given by $\tan\phi = (-Rd\beta)/(R\sin\beta\partial\vartheta) = -h_\vartheta/\sin\beta$. A third orthogonal coordinate system is introduced to describe the contact angle and the resulting surface tension force on the wall:

$$\begin{aligned} \underline{e}_\xi &= \underline{e}_R \\ \underline{e}_\eta &= \cos\alpha\,\underline{e}_\vartheta - \sin\alpha\,\underline{e}_\beta \\ \underline{e}_\zeta &= -\sin\alpha\,\underline{e}_\vartheta - \cos\alpha\,\underline{e}_\beta \end{aligned}$$

while

$$\begin{aligned} \underline{e}_R &= \sin\beta\underline{e}_r + \cos\beta\underline{e}_z \\ \underline{e}_\vartheta &= \underline{e}_\vartheta \\ \underline{e}_\beta &= \cos\beta\underline{e}_r - \sin\beta\underline{e}_z \end{aligned}$$

The coordinate systems are sketched in Figure 3.6.

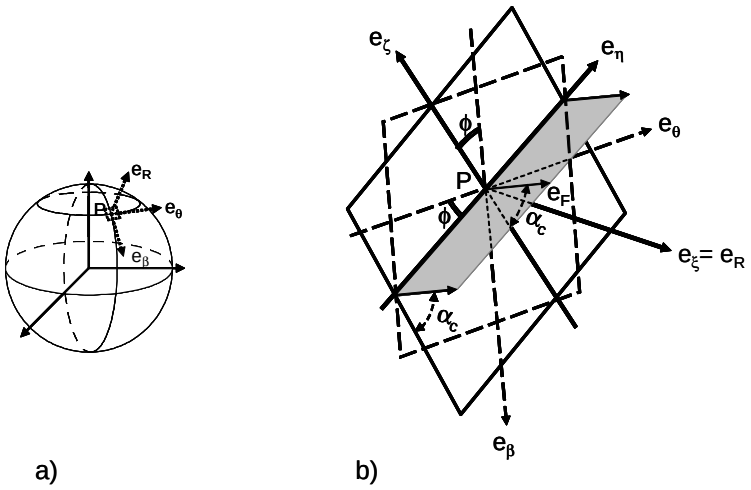

Figure 3.6: *A sketch of the coordinate systems used to describe an arbitrary interface meeting a sphere. As before a) shows the sphere while b) is a close look of the surface element at position P. With grey color is shown the interface surface.*

In the (ξ, η, ζ) coordinate system the interface is described by:

$$\zeta = g(\xi, \eta)$$

and the contact angle α_c is given by

$$\tan(\alpha_c - \pi/2) = \partial g/\partial \xi = g_\xi$$

while the unit vector in the direction of the surface tension force is expressed by:

$$\underline{\mathrm{e}}_F = \sin\alpha_c\,\underline{\mathrm{e}}_\xi - \cos\alpha_c\,\underline{\mathrm{e}}_\zeta$$

In order to express α_c in the r, ϑ, z coordinates we compare the representation of $d\underline{\mathrm{r}}$ in the three coordinate systems:

$$\begin{aligned}
d\underline{\mathrm{r}} &= dr\,\underline{\mathrm{e}}_r + r d\vartheta\,\underline{\mathrm{e}}_\vartheta + df\underline{\mathrm{e}}_z \\
&= (dr\,\sin\beta + df\,\cos\beta)\,\underline{\mathrm{e}}_R + r d\vartheta\,\underline{\mathrm{e}}_\vartheta + (dr\,\cos\beta - df\,\sin\beta)\,\underline{\mathrm{e}}_\beta \\
&= dR\underline{\mathrm{e}}_R + R\sin\beta d\vartheta\,\underline{\mathrm{e}}_\vartheta + Rdh\underline{\mathrm{e}}_\beta \\
&= dR\underline{\mathrm{e}}_R + R\sin\beta d\vartheta\,\left(\cos\phi\underline{\mathrm{e}}_\eta - \sin\phi\underline{\mathrm{e}}_\zeta\right) \\
&\quad -Rdh\left(\sin\phi\underline{\mathrm{e}}_\eta + \cos\phi\underline{\mathrm{e}}_\zeta\right) \\
&= dR\underline{\mathrm{e}}_R + (R\sin\beta d\vartheta\cos\phi - Rdh\sin\phi)\,\underline{\mathrm{e}}_\eta \\
&\quad + (-R\sin\beta d\vartheta\sin\phi - Rdh\cos\phi)\,\underline{\mathrm{e}}_\zeta \\
&= d\xi\,\underline{\mathrm{e}}_\xi + d\eta\,\underline{\mathrm{e}}_\eta + dg\,\underline{\mathrm{e}}_\zeta
\end{aligned}$$

Hence

$$\begin{aligned}
dR &= dr\,\sin\beta + df\,\cos\beta \\
R\sin\beta d\vartheta &= r d\vartheta \\
Rdh &= dr\,\cos\beta - df\,\sin\beta
\end{aligned}$$

and

$$\begin{aligned}
d\xi &= dR \\
d\eta &= R\sin\beta d\vartheta\cos\phi - Rdh\sin\phi \\
dg &= -R\sin\beta d\vartheta\sin\phi - Rdh\cos\phi
\end{aligned}$$

From last equation we can calculate $\partial g/\partial\xi = g_\xi$:

$$g_\xi = \left(\frac{dg}{d\xi}\right)_{d\eta=0} = \left(\frac{-R\sin\beta d\vartheta\sin\phi - Rdh\cos\phi}{dR}\right)_{d\eta=0}$$

Because $d\eta = R\sin\beta d\vartheta\cos\phi - Rdh\sin\phi = 0$ one obtains:

$$\begin{aligned}
\sin\beta d\vartheta &= h_R dR\tan\phi + h_\vartheta d\vartheta\tan\phi \\
(\sin\beta - h_\vartheta\tan\phi)\,d\vartheta &= h_R dR\tan\phi \\
d\vartheta &= \frac{h_R\tan\phi}{\sin\beta - h_\vartheta\tan\phi}dR
\end{aligned}$$

and, with $\tan\phi = -h_\vartheta/\sin\beta$:

$$\begin{aligned}
g_\xi &= \frac{-R\sin\beta d\vartheta\sin\phi - Rdh\cos\phi}{dR} \\
&= \cos\phi\left[-Rh_R - (R\sin\beta\tan\phi + Rh_\vartheta)\,\frac{d\vartheta}{dR}\right] \\
&= \frac{-R\sin\beta\,h_R}{\sqrt{\sin^2\beta + h_\vartheta^2}}
\end{aligned}$$

Next one has to express h_R and h_ϑ in $f(r,\vartheta)$:

$$\begin{aligned} h_R &= \left(\frac{dh}{dR}\right)_{d\vartheta=0} \\ &= \left(\frac{dr\,\cos\beta - f_r dr\,\sin\beta - f_\vartheta d\vartheta\,\sin\beta}{R\,(dr\,\sin\beta + f_r dr\,\cos\beta + f_\vartheta d\vartheta\,\cos\beta)}\right)_{d\vartheta=0} \\ &= \frac{\cos\beta - f_r\,\sin\beta}{R\,(\sin\beta + f_r\,\cos\beta)} \end{aligned}$$

$$\begin{aligned} h_\vartheta &= \left(\frac{dh}{d\vartheta}\right)_{dR=0} \\ &= \left(\frac{dr\,\cos\beta - f_r dr\,\sin\beta - f_\vartheta d\vartheta\,\sin\beta}{R\,d\vartheta}\right)_{dR=0} \end{aligned}$$

Since $dR = dr\sin\beta + f_r dr\cos\beta + f_\vartheta d\vartheta\cos\beta = 0$ we get:

$$dr = \frac{-f_\vartheta\cos\beta}{\sin\beta + f_r\cos\beta} d\vartheta$$

and

$$h_\vartheta = \left(\frac{dh}{d\vartheta}\right)_{dR=0} = \frac{-f_\vartheta}{R\,(\sin\beta + f_r\cos\beta)}$$

Hence the contact angle α_c is related to $\partial\zeta/\partial r$ and $\partial\zeta/\partial\vartheta$ according:

$$\begin{aligned} \cot(\alpha_c) &= -\tan(\alpha_c - \pi/2) = -g_\xi \\ &= \frac{R\sin\beta\, h_R}{\sqrt{\sin^2\beta + h_\vartheta^2}} \\ &= \frac{r\,(\cos\beta - f_r\,\sin\beta)}{\sqrt{r^2\,(\sin\beta + f_r\,\cos\beta)^2 + f_\vartheta^2}} \end{aligned} \tag{3.26}$$

3.4 Calculation of the interface shape around two particles

For particles not too close together the interface profile is just a sum of the profiles around each particle at infinite separation. This is the so called linear superposition approximation or Nikolson approximation [1],[4]. The interface profile around two floating particles in close proximity can still be written as linear combination of the profile functions for isolated particles. The coefficients in the solution are determined by the boundary conditions on the surface of the particles. The exact boundary conditions were received in section 3.3.

The governing equation for the shape $\zeta(x,y)$ of the interface between two liquids as it was shown (Eq. (3.21)) is given by:

$$\frac{\partial}{\partial x}\left[\frac{\partial\zeta/\partial x}{\sqrt{1+\left(\frac{\partial\zeta}{\partial x}\right)^2+\left(\frac{\partial\zeta}{\partial y}\right)^2}}\right] + \frac{\partial}{\partial y}\left[\frac{\partial\zeta/\partial y}{\sqrt{1+\left(\frac{\partial\zeta}{\partial x}\right)^2+\left(\frac{\partial\zeta}{\partial y}\right)^2}}\right] = \frac{g\Delta\rho}{\gamma}\zeta$$

If the slopes $\partial\zeta/\partial x$ and $\partial\zeta/\partial y$ are small, this differential equation reduces to the two dimensional Helmholz equation:

$$\frac{\partial^2\zeta}{\partial x^2} + \frac{\partial^2\zeta}{\partial y^2} = q^2\zeta$$

with $q = \sqrt{g\Delta\rho/\gamma}$ the inverse capillary length. In dimensionless cylindrical coordinates (we scale r and ζ on R_p), this reads:

$$\frac{1}{r}\frac{\partial}{\partial r}(r\frac{\partial\zeta}{\partial r}) + \frac{1}{r^2}\frac{\partial^2\zeta}{\partial\vartheta^2} = (qR_p)^2\zeta \tag{3.27}$$

The general solution of this linear differential equation is given by:

$$\zeta(r,\vartheta) = \sum_{m=0}^{\infty} \left[a_m\cos(m\vartheta) + b_m\sin(m\vartheta)\right] \mathrm{K}_m(qR_p r)$$

where $\mathrm{K}_m(x)$ is the modified Bessel function of the second kind and order m.

If we consider one particle in the origin the solution should have cylindrical symmetry and the only term that survives is the $m = 0$ term. The solution then coincide with the one given by Eq.(3.10). Consider now two particles with radius R, one positioned at $(x, y) = (d/2, 0)$ and one at $(x, y) = (-d/2, 0)$. The coordinate system is illustrated in Figure 3.7. Now we can write the general solution as linear combination of the single solutions:

$$\zeta(x,y) = \sum_{m=0}^{\infty} c_m \left[\mathrm{K}_m(qR_p\, r)\cos(m\vartheta) + \mathrm{K}_m(qR_p\, r^*)\cos(m\vartheta^*)\right] / \mathrm{K}_m(qR_p) \tag{3.28}$$

where

$$\begin{aligned} r &= \sqrt{(x-d/2)^2 + y^2} \\ \vartheta &= \arctan(y/\,(x-d/2)) \\ r^* &= \sqrt{r^2 + d^2 + 2rd\cos\vartheta} \\ \vartheta^* &= \pi - \arctan(r\sin\vartheta/\,(r\cos\vartheta + d)) \end{aligned}$$

Here (r, ϑ) and (r^*, ϑ^*) are the cylindrical coordinates of position (x, y) with respect to the first particle and the second particle. Note that the first and second term between square brackets in Eq.(3.28) have the same coefficient c_m. This is due to the symmetry of the problem, i.e. $\zeta\left(x\left(r,\vartheta\right), y\left(r,\vartheta\right)\right) = \zeta\left(x\left(r^*,\vartheta^*\right), y\left(r^*,\vartheta^*\right)\right)$.

The functions K_m have been normalized on $\mathrm{K}_m(qR_p)$ for convenience such that their values are of order one for $r \to R_p$.The $\sin(m\vartheta)$ terms have been dropped because of symmetry reasons. Since both r^* and ϑ^* are a function of r and ϑ, Eq.(3.28) can be written as:

$$\zeta(r,\vartheta) = \sum_{m=0}^{\infty} c_m Z_m(r,\vartheta) \tag{3.29}$$

where $Z_m(r,\vartheta)$ has been defined as:

$$Z_m(r,\vartheta) = \left[\mathrm{K}_m(qR\, r)\cos(m\vartheta) + \mathrm{K}_m(qR\, r^*(r,\vartheta))\cos(m\vartheta^*(r,\vartheta))\right] / \mathrm{K}_m(qR)$$

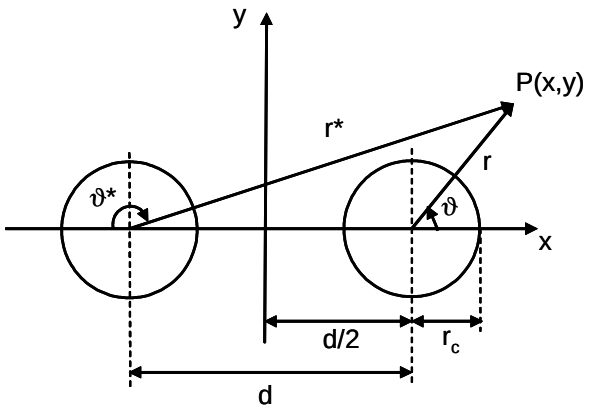

Figure 3.7: *The coordinate system used for the calculation of the interface profile for two particles. The particles are presented in top view.*

We are now looking for the specific solution that satisfies the boundary condition (see Eq.(3.26)):

$$\cot(\alpha_c) = \frac{r\ (\cos\beta - (\partial\zeta/\partial r)\sin\beta)}{\sqrt{r^2\left(\sin\beta + (\partial\zeta/\partial r)\cos\beta\right)^2 + (\partial\zeta/\partial\vartheta)^2}} \quad \text{at} \quad r = r_c \tag{3.30}$$

or $\partial\zeta/\partial r = F(\alpha_c, \beta, \zeta_\vartheta)$ at $r = r_c$. From Eq.(3.30) it follows that the function $F(\alpha_c, \beta, \partial\zeta/\partial\vartheta)$ is given by:

$$\begin{aligned} F &= \frac{\tan\beta\left(1+\tan^2\alpha_c\right)}{\tan^2\alpha_c\tan^2\beta - 1} \\ &\quad \pm\left[\left(\frac{\tan^2\alpha_c\left(1+\tan^2\beta\right)}{\tan^2\alpha_c\tan^2\beta - 1}\right)^2 + \frac{\left(1+\tan^2\beta\right)\left(\zeta_\vartheta/r\right)^2}{\tan^2\alpha_c\tan^2\beta - 1}\right]^{1/2} \\ &= \frac{\tan\alpha_c - \tan\beta}{1+\tan\alpha_c\tan\beta} \\ &\quad + \frac{\tan\alpha_c\left(1+\tan^2\beta\right)}{\tan^2\alpha_c\tan^2\beta - 1}\left(1 - \sqrt{1 + \frac{\left(\tan^2\alpha_c\tan^2\beta - 1\right)\left(\zeta_\vartheta/r\right)^2}{\tan^2\alpha_c\left(1+\tan^2\beta\right)}}\right) \\ &\simeq \frac{\tan\alpha_c - \tan\beta}{1+\tan\alpha_c\tan\beta} - \frac{\left(\zeta_\vartheta/r\right)^2}{2\tan\alpha_c} \end{aligned}$$

where ζ_M is the dimensionless z-coordinate of the center of the particle. The contact line is given by: $r_c^2 + (\zeta_c - \zeta_M)^2 = 1$ with $\zeta_c = \zeta(r_c, \vartheta)$, and $\tan(\beta(\vartheta)) = r_c/(\zeta_c - \zeta_M)$. The $(-)$ sign has been used to obtain a physical realistic solution. On the other hand from Eq. (3.29) it follows that:

$$\frac{\partial\zeta}{\partial r} = \sum_{m=0}^{\infty} c_m \frac{\partial}{\partial r} Z_m(r, \vartheta)$$

Combining the expressions for the $\partial\zeta/\partial r$ one receives:

$$\sum_{m=0}^{\infty} c_m \frac{\partial}{\partial r} \left[Z_m(r,\vartheta) \right]_{r_c(\vartheta)} = F(\alpha_c, \beta, \zeta_\vartheta) \tag{3.31}$$

with $r_c(\vartheta) = \sqrt{1-(\zeta_c - \zeta_M)^2}$. Eq.(3.31) should be true for all values of ϑ. Hence we write this equation as a Fourier expansion:

$$\sum_{m,\,k} c_m Q_{mk} \cos(k\vartheta) = \sum_k A_k \cos(k\vartheta) \tag{3.32}$$

with the coefficients Q_{mk} and A_k given by:

$$\begin{aligned} Q_{mk} &= \frac{1}{\pi\,(1+\delta_{k0})} \int_0^{2\pi} \frac{\partial}{\partial r} \left[Z_m(r,\vartheta) \right]_{r_c(\vartheta)} \cos(k\vartheta)\, d\vartheta \\ A_k &= \frac{1}{\pi\,(1+\delta_{k0})} \int_0^{2\pi} F(\alpha_c, \beta, \partial\zeta/\partial\vartheta) \cos(k\vartheta)\, d\vartheta \end{aligned}$$

Eq.(3.32) is true for all values of ϑ if:

$$\sum_m c_m Q_{mk} = A_k$$

Note that the coefficients Q_{mk} and A_k both depend on $c_0, .., c_M$, hence the problem is not linear. To solve this set first we assume that the series c_n converges to 0 for $n \to \infty$, so the series is cut off at $n = M$. Now the finite set can be solved by iteration because the matrix Q_{mk} is diagonal dominant. Because the monopole solution is given by:

$$\begin{aligned} Q_{00} &= -q\mathrm{K}_1(qR\,\sin\beta)/\mathrm{K}_0(qR) \\ A_0 &= \tan\phi_c \\ c_0 &= A_0/Q_{00} = \frac{-\tan\phi_c \mathrm{K}_0(qR)}{qR\,\mathrm{K}_1(qR\,\sin\beta)} \end{aligned}$$

and

$$c_k Q_{kk} = A_k - \sum_{m\neq k} c_m Q_{mk}$$

a scheme to solve this set of equations, is given by:

1. Start
2. initiate for all k: $c'_k := \delta_{k0}\, A_0/Q_{00}$
3. for all k: $c_k := c'_k$
4. calculate for all k and n: $Q_{nk}(c_0, .., c_M)$, $A_k(c_0, .., c_M)$
5. for all k: $c'_k := \left(A_k - \sum_{n\neq k} c_n Q_{nk} \right) / Q_{kk}$
6. if for any k: $|c'_k - c_k| > \epsilon$ go to step 3
7. Stop

Once knowing the coefficients $c_0, .., c_M$ the interface profile is also known:

$$\zeta(x,y) = \sum_{n=0}^{M} c_n \left[\mathrm{K}_n(qR\,r)\cos(n\vartheta) + \mathrm{K}_n(qR\,r^*)\cos(n\vartheta^*) \right] / \mathrm{K}_n(qR)$$

3.5 Calculation of the force between two particles

Let us consider the interactions between two spheres situated at an interface at a distance d. As before the coordinate plane xy coincide with the flat interface far away from the particles. The interface shape is described by $\zeta(x, y)$ and it is given by Eq. (3.28). Two types of forces are exerted on each sphere: the interfacial tension force and the hydrostatic pressure. The resultant of these forces in x-direction gives us the capillary interaction force. Here it will be calculated by considering a large rectangular volume that surrounds one of the spheres and has the middle plane between the spheres as a bounding surface, see Figure 3.8. A similar approach was used in [5].

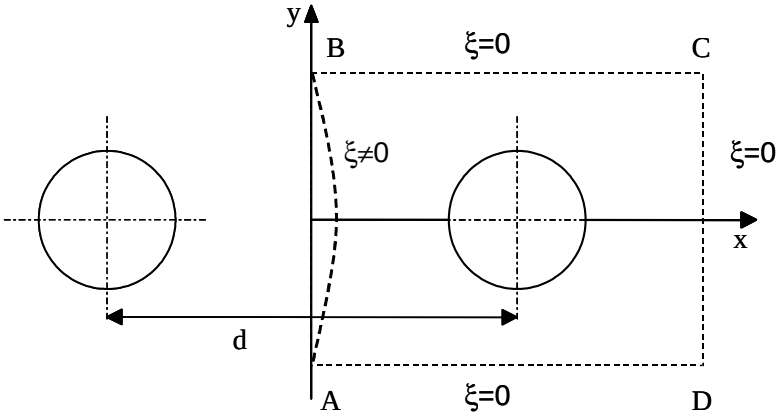

Figure 3.8: *Layout for the contour integration of the capillary force.*

The size of the integration contour ABCD is large enough to ensure that AD, BC and CD are lying in the regions where the interface is flat ($\zeta = 0$). Only along the segment AB the interface is not flat ($\zeta \neq 0$) and it is given by the function $\zeta(0, y) = \zeta_{0y}$.

The x-component of the force due to the hydrostatic pressure is given by:

$$\underline{F}^{(p)} = \underline{\mathrm{e}}_x \int_S P ds$$

where S is the area of the plane zy between the y-axis and ζ_{0y} curve and:

$$\begin{aligned} P &= P_0 - \rho_l g z \quad \text{at} \quad z < \zeta_{0y} \\ P &= P_0 - \rho_u g z \quad \text{at} \quad z > \zeta_{0y} \end{aligned}$$

Then in dimensionless form (we scale y and z on R_p) :

$$F^{(p)} = R_p^3 \int_{-\infty}^{\infty} \int_0^{\zeta_{0y}} (-\rho_l g z + \rho_u g z)\, dz dy = -\Delta\rho g R_p^3 \int_0^{\infty} \zeta_{0y}^2 dy \tag{3.33}$$

The x-component of the interfacial tension acting along the contour ABSD is given by:

$$\underline{F}^{(\gamma)} = \underline{\mathrm{e}}_x \int_{ABCD} \gamma dl$$

The integrals along the segments BC and DA cancel each other because of the symmetry of the system. The line segment dl can be expressed as: $dl = \sqrt{dy^2 + d\zeta^2} = dy\sqrt{1 + (d\zeta/dy)^2}$. Consequently:

$$F^{(\gamma)} = 2\gamma R_p \int_0^\infty \left(\frac{dl}{dy} - 1\right) dy = 2\gamma R_p \int_0^\infty \left(\sqrt{1 + \left(\frac{d\zeta}{dy}\right)^2} - 1\right) \tag{3.34}$$

where again scaling on R_p was used. Combining Eqs. (3.33) and (3.34) one will receive the capillary force for two identical particles:

$$F_c = F^{(p)} + F^{(\gamma)} = 2\gamma R_p \int_0^\infty \left(\sqrt{1 + \left(\frac{d\zeta}{dy}\right)^2} - 1\right) dy + \Delta\rho g R_p^3 \int_0^\infty \zeta_{0y}^2 dy$$

This expression can be simplified further by substituting $\sqrt{1 + (d\zeta/dy)^2} \approx 1 + \frac{1}{2}(d\zeta/dy)^2$ and $g\Delta\rho = \gamma q^2$:

$$\frac{F_c}{\gamma R_p} = \int_0^\infty \left(\frac{d\zeta_{0y}}{dy}\right)^2 dy + (qR_p)^2 \int_0^\infty \zeta_{0y}^2 dy \tag{3.35}$$

where ζ_{0y} is given by (see Eq. 3.28):

$$\zeta(0, y) = \sum_{n=0}^{M} 2\, c_n\, \mathrm{K}_n(qR\, r_{0y}) \cos(n\vartheta_{0y}) / \mathrm{K}_n(qR)$$

with $r_{0y} = r(0, y)$ and $\vartheta_{0y} = \vartheta(0, y)$.

3.6 Summary

In this chapter we considered a single particle trapped at an interface. The interface deformation created by the particle is calculated from a set of equations. These are obtained from the vertical force balance acting on the particle and from the interface shape around the particle.

Moreover a theoretical expression was derived for the capillary force between two spheres captured at the interface. The capillary force was calculated by integrating the pressure and interfacial tension contribution over an arbitrary volume. An analytical procedure was developed to solve the linearized Young-Laplace equation which describes the interface shape. The linearization is valid as long as the interface slope is small. The solution is expressed as a series of Bessel functions with coefficients determined by the boundary condition for the contact angle at the particles surface. This approach is appropriate for any distance between the particles thus it can describe the interactions between particles in an aggregate.

The calculation of the interface profile and the interaction forces for a multiple particle system can be done using a similar method as for the two particle case. It will be treated in the next chapter.

References

[1] M.M. Nicolson, *Proc. Cambridge Philos. Soc.* 45, 288, **1949**.

[2] Rapacchietta A.V., Neumann A.W., Omenyi S.N , *JCIS*, **1977**, 59(3).

[3] Princen H.M. "The equilibrium shape of interfaces, drops and bubbles" in Surface and colloid science, vol. 2 (Matijevic E.,Ed.), Interscience, New York, **1969**

[4] D.Y. Chan, J.D. Henry, and l.R.White, *JCIS*, **1981**, 79(2), 411.

[5] Velev O. D., Denkov N. D., Paunov V. N., Kralchevsky P. A., Nagayama K., *Langmuir*, **1993**, 9, 3702.

Chapter 4

Capillary forces between spherical particles floating at a liquid-liquid interface*

Abstract

We study the capillary forces acting on sub-millimeter particles (0.02-0.6 mm) trapped at a liquid-liquid interface due to gravity-induced interface deformations. An analytical procedure is developed to solve the linearized capillary (Young-Laplace) equation and calculate the forces for an arbitrary number of particles, allowing also for a background curvature of the interface. The full solution is expressed in a series of Bessel functions with coefficients determined by the contact angle at the particle surface. For sub-millimeter spherical particles, it is shown that the forces calculated using the lowest order term of the full solution (linear superposition approximation; *LSA*) are accurate to within a few percents. Consequently the many particle capillary force is simply the sum of the isolated pair interactions. To test these theoretical results, we use video microscopy to follow the motion of individual particles and pairs of interacting particles at a liquid-liquid interface with a slight macroscopic background curvature. Particle velocities are determined by the balance of capillary forces and viscous drag. The measured velocities (and thus the capillary forces) are well described by the *LSA* solution with a single fitting parameter.

4.1 Introduction

In many cases, one observes the formation of aggregates of particles at a liquid interface due to attractive capillary forces. Capillary forces appear whenever the particles distort the liquid interface. The resulting self-assembly of particles has various industrial applications (e.g., enhanced oil recovery, waste water treatment, paint coatings [1], food products [2], or ore flotation [3], etc.). New important applications include the use in nanotechnology [4] and in modeling of processes in biological systems [5, 6]. For a review about the importance of the self-assembly in different areas, one can see [7].

Theoretically, determining the strength of interaction forces between bodies at an interface requires solving the Young-Laplace equation, which describes the interface shape.

*This chapter has been published in *Langmuir* **2005**, 21, 11190.

This equation is a second order nonlinear differential equation that can be solved numerically [8]. Analytical solutions can only be obtained for highly symmetric situations or using approximations. The most common approximation is the linearization of the Young-Laplace equation, valid when the interface slope is small. The first to derive an analytical expression for the capillary force in the present context, was Nicolson [9], for two floating bubbles. He expressed the interface profile as a sum of the profiles around the isolated bubbles, the so-called linear superposition approximation (*LSA*). Chan and coworkers [10] showed that the error introduced by using the linear Young-Laplace equation is small for small particles (small Bond numbers) and extended the use of the *LSA* to floating cylinders and spheres. The *LSA* is not valid for large interface slopes and very small distances between particles (where the boundary conditions are violated [9, 10, 11]).

A number of studies on the capillary interactions between different bodies has been done by Kralchevsky and coworkers (see references [11, 12] for an overview). They calculated the exact force for two cylinders and spheres numerically and compared it with the approximated formula. It was concluded that for short distances between the particles the approximated formula underestimates the force considerably. In the case of floating spheres they calculate the interaction by replacing the spheres with equivalent cylinders [13]. As we will show, this approximation leads to a violation of the boundary conditions and thus to erroneous results.

More complex boundary conditions were recently considered in studies [14, 15, 16] examining the interactions between micrometer- and nanometer-sized particles with an undulated contact line in the absence of gravity. The meniscus shape is expressed as a multipole expansion in analogy with methods used in electrostatics. The leading term considered is the quadrupole–quadrupole interaction.

To our knowledge, there are few experimental studies of the capillary force between freely floating spherical particles. Velev and coworkers [17] measured the equilibrium distance between a floating particle and a vertical wall as a function of the wall immersion and compared their result with theoretical calculations. In a similar experiment Petkov and coworkers [18] determined the drag coefficient of sub-millimeter particles at the liquid interface by measuring the velocity of the particles under the action of capillary forces. The capillary force was varied by changing the position of the vertical wall. Joseph and coworkers [19] investigate the rate of approach of two particles at a liquid interface. The aggregation kinetics between many particles at an interface was studied by Vincze and coworkers [20], who examined the dynamic development of cluster structure. In the experiments of Velev and coworkers [21] and Dushkin and coworkers [22] the particles vertical positions at the interface were defined by attachment to some holder. The capillary force measured thus originated from the wettabilty rather than the weight of the particles.

In this study we concentrate on the capillary interactions between two or more submillimeter spherical particles trapped at an interface. Multiple particle interactions have not been studied extensively, despite the fact that in the case of aggregates they should be very important.

The final goal of our research, which will be discussed in a future publication, is to study aggregates trapped at an interface between two liquids [23]. The behavior of such aggregates in shear flow is a function of the hydrodynamic and capillary interactions between the particles that form the aggregate.

In the present paper we describe a method for calculating the capillary forces between multiple objects, cylinders or spheres, at a liquid-liquid interface with a certain background profile. For this purpose we solve the linearized non- homogeneous Young-

Laplace equation analytically using a series of modified Bessel functions. The coefficients of this series are determined by considering the exact boundary conditions on the objects. This approach results in robust and accurate scheme for the force calculation even for small distances between the objects. We also present experimental data for the motion of one spherical particle and a pair of interacting particles floating at a liquid liquid-interface with a curved background profile. The force calculations are compared with the experimental results, which confirm the validity of the model. Moreover we can determine the drag force on the particles which is modified due to the presence of the interface. The paper is organized as follows: the calculation of the capillary forces is explained in Sec.4.2, we describe the experimental set-up and procedures in Sec. 4.3 and the results are presented and discussed in Sec. 4.4. The paper ends in Sec. 4.5 with our conclusions, while some mathematical aspects of the theory are described in three appendices.

4.2 Force calculation

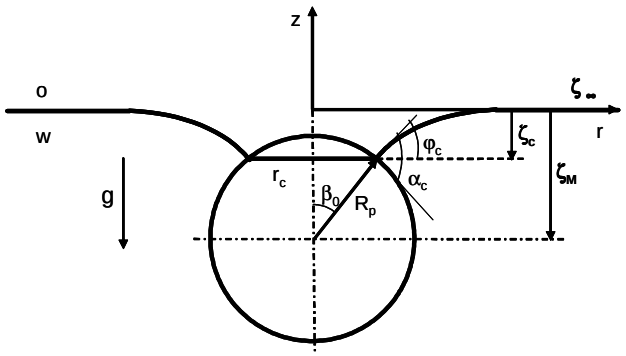

Figure 4.1: *A sketch of a single particle at the interface. R_p is the radius of the particle, α_c is the contact angle, β_0 the central cone angle, r_c the radius of the tpc-line, ϕ_c the slope of the interface at the tpc-line, ζ_c the z coordinate of the tpc-line and ζ_M the z coordinate of the center of the particle and ζ_∞ the height of the interface where the interface deformation is zero.*

In this section we discuss the calculation of the gravity-induced capillary force on a particle floating at a liquid-liquid interface due to the presence of other particles. The influence of each particle on the interface shape is represented by a series of singular solutions of the governing linearized differential equation, with the singularities located at the center of the particle considered. The full interface profile is described by a linear combination of these solutions. The coefficients are determined from the boundary condition on the particle: the contact angle of the interface with the particle surface is constant. The influence of a background profile due to a container, can be taken into account by another series of singular solutions. By doing so one obtains an analytical solution for the interface profile where the coefficients, representing the strength of the individual contributions, can be calculated numerically. Given an interface profile, the capillary force on each particle can be calculated by integrating the surface tension along the three-phase-contact-line (tpc-line) around the particle and the pressure over the particle surface.

4.2.1 Particles at a liquid-liquid interface

The interface between two liquids on which the particles are floating, can be described with $z = \zeta(x, y)$, where x and y are the axes in the horizontal plane and z-axis is oriented vertical upwards. The basic system of a single particle at the interface is illustrated in Figure 4.1. To calculate this profile one has to in general solve the Young-Laplace equation [24]:

$$\begin{aligned} \frac{\partial}{\partial x}\frac{\partial\zeta/\partial x}{\sqrt{1+\left(\frac{\partial\zeta}{\partial x}\right)^2+\left(\frac{\partial\zeta}{\partial y}\right)^2}}+\frac{\partial}{\partial y}\frac{\partial\zeta/\partial y}{\sqrt{1+\left(\frac{\partial\zeta}{\partial x}\right)^2+\left(\frac{\partial\zeta}{\partial y}\right)^2}} \\ = \quad \frac{g\Delta\rho}{\gamma}\left(\zeta-\zeta_\infty\right) \end{aligned} \tag{4.1}$$

where γ is the interfacial tension between the two liquids, $\Delta\rho = \rho_l - \rho_u$ is the density difference between the lower and upper liquid, g is the acceleration due to gravity and ζ_∞ is the height of the interface in regions where the curvature of the interface is zero. When the buoyancy and gravity forces on the particles are considerably smaller than the maximum interfacial tension force, (i.e. if $4/3\,\pi R_p^3 g(\rho_p - \rho_l) \ll 2\pi R_p\gamma$), the interface slope $\underline{\nabla}\zeta$ near the particles is very small. Here R_p is the radius of the particle and ρ_p is its density. For our experimental parameters, listed in Table 4.1, this condition holds because $R_p \ll 2\ mm$. Therefore one can reduce Eq.(4.1) to the two-dimensional Helmholtz equation, which in cylindrical coordinates becomes:

$$\frac{1}{r}\frac{\partial}{\partial r}\left(r\frac{\partial\zeta}{\partial r}\right)+\frac{1}{r^2}\frac{\partial^2\zeta}{\partial\vartheta^2}=q^2\left(\zeta-\zeta_\infty\right) \tag{4.2}$$

where $q = \sqrt{g\Delta\rho/\gamma}$ is the inverse capillary length. In the following we define $\zeta_\infty = 0$ as indicated in Figure 4.1. The general solution of this linear differential equation is obtained by using separation of variables [25]:

$$\begin{aligned} \zeta(r,\vartheta) \quad = \quad & \sum_{m=0}^{\infty}\left(a_m\mathrm{I}_m(qr)+b_m\mathrm{K}_m(qr)\right)\cos(m\vartheta) \\ & + \\ & \sum_{m=0}^{\infty}\left(c_m\mathrm{I}_m(qr)+d_m\mathrm{K}_m(qr)\right)\sin(m\vartheta) \end{aligned} \tag{4.3}$$

where $I_m(x)$ and $K_m(x)$ are modified Bessel functions of the first and second kinds, both of order m. The coefficients a_m, b_m, c_m and d_m are determined from the boundary conditions. In the simplest case of one particle at the origin, the solution has cylindrical symmetry ($m = 0$) and must decay to zero for $r \gg R_p$. In this case the only term that remains in the solution is the K_0 term. However, for N particles, with the ith particle positioned at (x_i, y_i), the general solution can be written as a linear combination of singular solutions located at the particle positions:

$$\zeta(x,y)=\sum_{i=1}^{N}\sum_{m=-\infty}^{\infty}c_m^{(i)}Q_m(r_i,\vartheta_i) \tag{4.4}$$

with:

$$\begin{aligned} Q_{-m}(r,\vartheta) &= \frac{\mathrm{K}_m(qr)}{\mathrm{K}_m(qR_p)}\sin(m\vartheta) \\ Q_0(r,\vartheta) &= \frac{\mathrm{K}_0(qr)}{\mathrm{K}_0(qR_p)} \\ Q_m(r,\vartheta) &= \frac{\mathrm{K}_m(qr)}{\mathrm{K}_m(qR_p)}\cos(m\vartheta) \end{aligned}$$

where $m > 0$. Here (r_i, ϑ_i) are the cylindrical coordinates of the position (x, y) with respect to particle i: $r_i = ((x - x_i)^2 + (y - y_i)^2)^{1/2}$ and $\vartheta_i = \arctan((y - y_i) / (x - x_i))$. The functions $Q_m(r, \vartheta)$ have been normalized for convenience such that their values are of order one for $r \longrightarrow R_p$. The coefficients $c_m^{(i)}$ in Eq.(4.4) are determined by the boundary condition on the particles (see Figure 4.2 and Appendix 4B for the full derivation).

4.2.2 Background profile

In general the interface profile due to the container (the background profile) is not flat because the contact angle at the tpc-line along the walls differs from $\pi/2$. The background profile ζ_∞ for a circular container (i.e. a Petri dish) is given by:

$$\zeta_\infty(r) = \frac{[\partial\zeta_\infty/\partial r]_{\mathrm{ref}}}{q\,\mathrm{I}_1(qr_{\mathrm{ref}})}\,\mathrm{I}_0(qr) \tag{4.5}$$

where the center of the container is located at $r = 0$ and r_{ref} is some reference position as indicated in Figure 4.3. Eq.(4.5) can be obtained from Eq.(4.3) using the appropriate boundary conditions at $r = 0$ and $r = r_{\mathrm{ref}}$ and is only valid if $(\partial\zeta_\infty/\partial r)^2 \ll 1$. For practical reasons the slope is not determined at the wall of the container but at r_{ref} close to the wall. Since I_0 is an increasing function with increasing r, one can state that if $[\partial\zeta_\infty/\partial r]^2_{\mathrm{ref}} \ll 1$, this condition is fulfilled for $r \leq r_{\mathrm{ref}}$.

Taking into account the background profile, the general solution of Eq.(4.2) is given by:

$$\zeta(x,y) = \sum_{m=-\infty}^{\infty}\left(c_m^{(0)}P_m(r,\vartheta) + \sum_{i=1}^{N} c_m^{(i)}Q_m(r_i,\vartheta_i)\right) \tag{4.6}$$

with:

$$\begin{aligned} P_{-m}(r,\vartheta) &= \frac{\mathrm{I}_m(qr)}{\mathrm{I}_m(qr_{\mathrm{ref}})}\sin(m\vartheta) \\ P_0(r,\vartheta) &= \frac{\mathrm{I}_0(qr)}{\mathrm{I}_0(qr_{\mathrm{ref}})} \\ P_m(r,\vartheta) &= \frac{\mathrm{I}_m(qr)}{\mathrm{I}_m(qr_{\mathrm{ref}})}\cos(m\vartheta) \end{aligned}$$

where $m > 0$. Here (r, ϑ) are the coordinates of the position (x, y) with respect to the center of the dish: $r = (x^2 + y^2)^{1/2}$ and $\vartheta = \arctan(y/x)$. The functions $P_m(r, \vartheta)$ have been normalized for convenience. The coefficients $c_m^{(i)}$ are now determined from the boundary conditions on the particles and on the walls of the container. This involves several mathematical steps which are further explained in Appendix 4A, where the slope of the interface at the tpc-line, $[\partial\zeta/\partial r_j]$ at $r_j = r_{\mathrm{tpc}}(\vartheta_j)$, is related to the contact angle α_c.

4.2.3 Capillary force on a particle

To calculate the total capillary force on a particle it is convenient to integrate the surface tension along the tpc-line and the pressure over the particle surface. The contribution of the interfacial tension along the tpc-line is given by (see Eq.(4.30) from Appendix 4C):

$$\underline{\mathrm{F}}^{[\gamma]} = \gamma \int_0^{2\pi} dl\, \underline{\mathrm{e}}_F\, d\vartheta \tag{4.7}$$

where $\underline{\mathrm{e}}_F$ is the unit vector in the interface normal to the tpc-line as sketched in Figure 4.2. This unit vector can be expressed in the Cartesian unit vectors:

$$\underline{\mathrm{e}}_F = n_x(\vartheta)\underline{\mathrm{e}}_x + n_y(\vartheta)\underline{\mathrm{e}}_y + n_z(\vartheta)\underline{\mathrm{e}}_z$$

where the functions $n_\alpha(\vartheta)$, $\alpha \in \{x, y, z\}$, as well as dl are given in Appendix 4C by Eqs.(4.27) and (4.29).

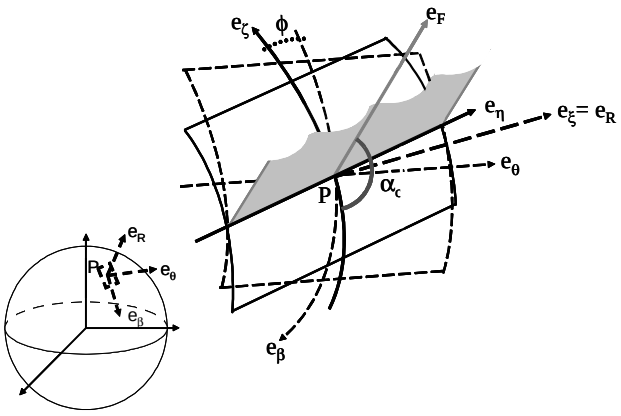

Figure 4.2: *A sketch of the coordinate systems used to describe the relation between the slope* $\underline{\nabla}\zeta$ *of the interface near the tpc-line and the contact angle* α_c *at a point* P*. The tpc-line is along the* $\mathbf{e}_\eta$ *vector, the gray surface represents the interface.*

The contribution of the pressure distribution over the particle surface is :

$$\underline{\mathrm{F}}^{[p]} = -\int_0^{2\pi}\int_0^{\pi} p(\chi,\vartheta) R_p^2 \underline{\mathrm{e}}_R \sin\chi\, d\chi\, d\vartheta$$

where $p(\chi,\vartheta) = p_0 + gR_p\,\rho\,(z_M + \cos\chi)$ with p_0 a reference pressure, z_M the z-coordinate of the center of the particle and $\rho = \rho_u$ for $0 < \chi < \beta(\vartheta)$ and $\rho = \rho_l$ for $\beta(\vartheta) < \chi < \pi$, χ being the azimuth with respect to the z-axis. Expressed in components one obtains for

the pressure contribution to the force:

$$\begin{aligned}
\frac{F_x^{[p]}}{g\Delta\rho R_p^3} &= \int_0^{2\pi} \left(\tfrac{1}{2} z_M \left[\sin\beta\cos\beta - \beta\right] - \tfrac{1}{3}\sin^3\beta\right) \cos\vartheta \, d\vartheta \\
\frac{F_y^{[p]}}{g\Delta\rho R_p^3} &= \int_0^{2\pi} \left(\tfrac{1}{2} z_M \left[\sin\beta\cos\beta - \beta\right] - \tfrac{1}{3}\sin^3\beta\right) \sin\vartheta \, d\vartheta \\
\frac{F_z^{[p]}}{g\Delta\rho R_p^3} &= \int_0^{2\pi} \left(\tfrac{1}{3}\cos^3\beta - \tfrac{1}{2} z_M \sin^2\beta\right) d\vartheta + \frac{2\pi\left(\rho_u + \rho_l\right)}{3\Delta\rho}
\end{aligned}$$

The net capillary force on the particle is given by:

$$\underline{\mathrm{F}}^{[\mathrm{cap}]} = \left(F_x^{[\gamma]} + F_x^{[p]}\right) \underline{\mathrm{e}}_x + \left(F_y^{[\gamma]} + F_y^{[p]}\right) \underline{\mathrm{e}}_y \tag{4.8}$$

The sum of the z components of the force can be used as a check on the particle weight.

Summarizing, we obtain the capillary force acting on a particle floating in an ensemble of particles at a liquid-liquid interface by calculating the interface profile $\zeta(x, y)$ using Eq.(4.6). The coefficients $c_m^{(i)}$ in this equation are determined as described in Appendix 4B. Once knowing $\zeta(x, y)$ the capillary force on a particle can be calculated by integrating the pressure distribution over its surface and the interfacial tension along its tpc-line, as described above and in Appendix 4A. Details of the actual force calculation have been given in Appendix 4C.

4.2.4 The *LSA*

In the Linear Superposition Approximation (*LSA*) only the zero order Bessel contributions of the particles to the interface profile are taken into account. In this approximation the expression for the capillary force on the ith particle due to the presence of the jth particle reduces to [13, 15]:

$$\underline{\mathrm{F}}_{\mathrm{lsa}}^{[\mathrm{i,j}]} = -2\pi\gamma\, Q_p^2\, q\, \mathrm{K}_1(qr_{ij})\, \hat{\mathrm{r}}_{ij} \tag{4.9}$$

where $\hat{\mathrm{r}}_{ij}$ is the unit vector along the center to center line pointing from particle j to particle i and r_{ij} is the center to center distance between the particles. The coefficient Q_p is defined as

$$Q_p = \frac{-\tan(\alpha_c - \beta_o)}{q\, \mathrm{K}_1(qR_p \sin\beta_o)} \tag{4.10}$$

where $r_c = R_p \sin\beta_o$ is the radius of the circle formed by the tpc-line for a single particle and α_c the contact angle of the particle. In practice we have $\tan(\alpha_c - \beta_o) \ll 1$ and $qR_p \sin\beta_o \ll 1$, such that $\tan(\alpha_c - \beta_o) \simeq \sin(\alpha_c - \beta_o)$ and $\mathrm{K}_1(x) \simeq 1/x$. This leads to $Q_p = -R_p \sin\beta_o \sin(\alpha_c - \beta_o)$, an expression used previously by others [11, 12].

The expression for the capillary force on the particle due to the background profile using the *LSA* reduces to a simple form, too :

$$\underline{\mathrm{F}}_{\mathrm{lsa}}^{[\mathrm{bg}]} = 2\pi\gamma\, Q_p Q_d\, q\, \mathrm{I}_1(qr)\, \hat{\mathrm{r}} \tag{4.11}$$

where Q_p has been given above and:

$$Q_d = \frac{\left[\partial\zeta_\infty/\partial r\right]_{r_{\mathrm{ref}}}}{q\, \mathrm{I}_1(qr_{\mathrm{ref}})} \tag{4.12}$$

A similar idea for the force calculation between a wall and a particle was considered by Chan and coworkers [10]. The net capillary force on particle i within the *LSA* is expressed as:

$$\underline{\mathrm{F}}_{\mathrm{lsa}}^{[\mathrm{i}]} = 2\pi\gamma\, qQ_p[Q_d\, \mathrm{I}_1(qr_i)\, \hat{\mathrm{r}}_i - Q_p \sum_{j\neq i} \mathrm{K}_1(qr_{ij})\, \hat{\mathrm{r}}_{ij}] \tag{4.13}$$

The validity of the *LSA* will be evaluated below by comparing with the full model, i.e. Eq.(4.8) versus Eq.(4.13).

4.3 Experimental

4.3.1 Materials

The experimental system consists of two immiscible liquids layered on top of each other with spherical particles suspended at the interface. The liquid phases used were pentadecane (Acros organics) and a water-salt-glycerol mixture. 35 wt.% glycerol (Merck) was added to deionized water to match the viscosity of the pentadecane (2.34 mPas). The viscosity match aids in estimating the drag force on the particles at the interface. 0.15 M NaCl (Merck) was added to the water phase to suppress possible electrostatic effects. Glass particles (Tamson) with an average radius of 320 μm were used. The interfacial tension and the densities of the experimental system are listed in Table 4.1.

	This study	System of Paunov and coworkers	
R_p	317	10	μm
ρ_l	1090	1000	kg/m^3
ρ_u	773	0	kg/m^3
ρ_p	2900	3000	kg/m^3
γ	0.044	0.072	N/m
α_c	40	30, 60, 90	deg
qR_p	0.0843	0.0037	-

Table 4.1: *Properties of the particle-fluid systems used by us and by Paunov et al. [13]. R_p is the particle radius, ρ_l, ρ_u, ρ_p are the densities of the lower phase, upper phase and the particle, respectively. γ is the interfacial tension, α_c is the contact angle and q is the inverse capillary length.*

4.3.2 Experimental setup and procedure

The experimental setup is illustrated in Figure 4.3. It consists of a glass Petri dish (diameter 85 mm) placed upon a horizontal anti-vibration table. The two liquid phases are immiscible and naturally layer due to the density difference. The dish is covered with a transparent plastic lid with a small hole through which we deposit the particles at the interface (about 32 mm from the center of the dish). A microscope (Olympus SZX9) with a CCD camera is mounted above the vessel and connected to an image acquisition system, to record the motion of the particles at the interface.

The measurement protocol used is described below. The two liquids are left to equilibrate in the dish for one hour. At this point, a single glass particle is deposited at the interface and it moves towards the middle of the dish due to the curvature of the interface.

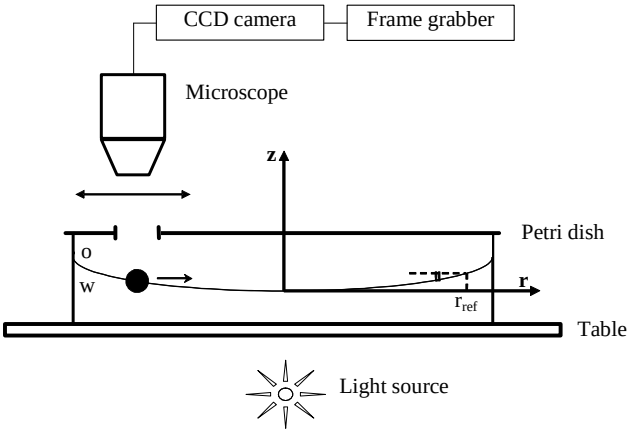

Figure 4.3: *Schematic layout of the experimental setup.*

When the particle reaches its equilibrium position near the center of the dish, a second particle is deposited at the interface, at the same initial position as the first. It also moves towards the center and interacts with the first particle. The motion of both particles has been recorded. The experiments are repeated eight times in order to check reproducibility and to collect statistically significant data. From the acquired images the coordinates (x_i^n, y_i^n) of the nth particle are extracted as a function of the time t_i. These coordinates are used to calculate the radial distance from the center of the dish r_i^n, the distance between the two particles d_i and their average velocities $v_{i+1/2}^n = \left(r_{i+1}^n - r_i^n\right) / \left(t_{i+1} - t_i\right)$.

For time scales larger than $t_o = \left(4/3\pi\rho_p R_p^3\right) / \left(6\pi\eta R_p\right) \simeq 25$ ms the inertia of the particles is negligible. In this case the capillary interaction force balances the drag force and can therefore be calculated by applying Stokes drag law:

$$\underline{\mathrm{F}}_d = -6\pi\eta\, R_p\, f_d\, \underline{\mathrm{v}}. \tag{4.14}$$

A correction coefficient f_d was introduced to account for the presence of the interface. The presence of the interface breaks the symmetry of the flow pattern around the particle, leading to an increased drag. When the equator plane of the particle coincides with the interface one expects $f_d = 1$ [26]. In our experiments we suppose f_d to be of order unity, but larger than one. The trajectory of the first particle is used to map out the influence of the interaction with the background profile. The two-particle interaction can be singled out from this background influence.

4.3.3 Profile near a single particle

In order to describe the vertical position of the particles with respect to the interface we require a value for the contact angle of the liquid-liquid interface with the particle surface. This contact angle has been measured by pouring the oil and the water phases into a square cuvette (Starna Gmbh). The fluids were left to equilibrate for one hour. A single glass particle was deposited at the interface and after another hour images of the particle were recorded from the side with the microscope and the CCD camera. A typical example of such an image is shown in Figure 4.4. From the captured pictures, the

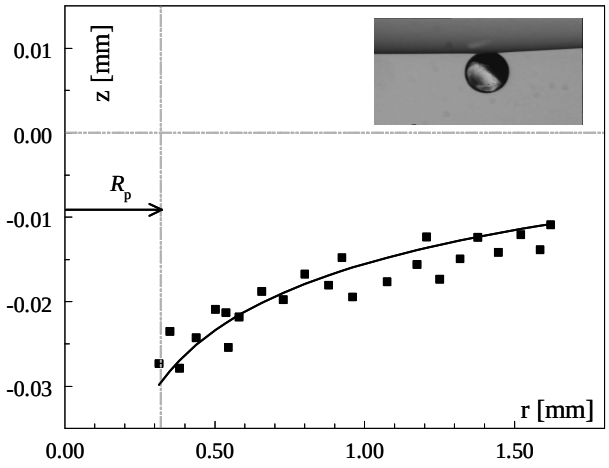

Figure 4.4: *The distortion of the interface caused by the particle. The symbols are the experimental data (after substracting the background profile), and the line represents the theoretical solution. Inset: An image of a glass particle at the glycerol solution-pentadecane interface in a cuvette.*

equilibrium contact angle was determined to be $\alpha_c = 40 \pm 4^o$. Given the contact angle one can calculate also the radius r_c of the tpc-line and the angle β_o by considering the force balance on the particle and the interface profile near the particle (similar to the approach used in [27]).

Further image analysis provided the interface profile near the particle. By subtraction of the background profile (the interface without the particle) we obtain the deformation of the interface due to the particle. This profile was compared with the theoretical solution (see Sec. 4.2), $\zeta(r) = Q_p \mathrm{K}_0(qr)$. As can be observed from Figure 4.4, the calculated curve is in good agreement with the experimental results.

Previous researchers [28, 29] have shown the presence of an electrostatic force at the liquid-liquid interface that is transmitted through the oil phase. The electrostatic effects in the water phase were suppressed by the addition of salt. Such an electrodipping force, as stated in [28], will push the particle further into the water phase. We compared the theoretical value of Q_p (-8.9 μm from Eq.(4.10)) with the value from the best fit to the data in Figure 4.4: -9.7 ± 1.5 μm and conclude that this possible electrostatic force is not significant for the capillary interactions in our system.

4.3.4 Background profile

The undisturbed interface profile was determined independently from an additional experiment using light refraction from the interface [30, 31]. The Petri dish was completely filled such that the upper phase contacts the cover glass. This prevents the appearance of a second free interface (oil/air). A vertical narrow laser beam (He-Ne) crosses the liquid-liquid interface at a radial position r_{ref} approximately 35 mm from the center of the dish. The refracted beam, see Figure 4.5, travels about 1.65 m through the air

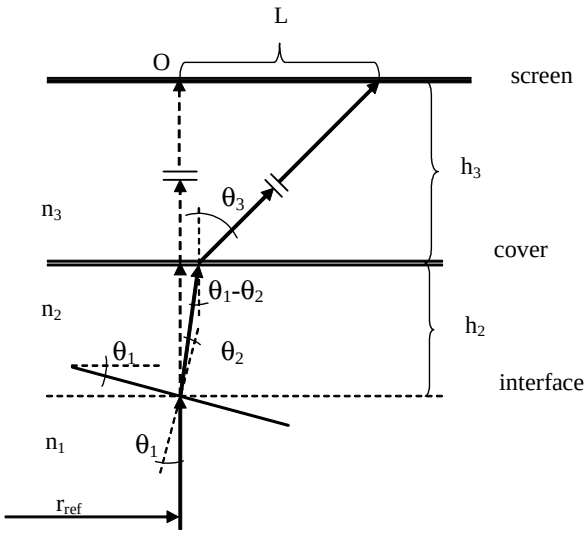

Figure 4.5: *Schematic representation of the path of the light beam defining the symbols used in the calculation of $L(\theta_1)$. The refraction from the glass cover is negligible and not shown for simplicity.*

before it reaches a screen. The resulting light spot is shifted a distance L from the reference position, i.e. the position of the light spot when the dish is empty. Using Snell's law ($n_3 \sin\theta_3 = n_2 \sin(\theta_1 - \theta_2)$ and $n_2 \sin\theta_2 = n_1 \sin\theta_1$) we express the distance $L = h_3 \sin\theta_3 + h_2 \sin\theta_2$ in the interface slope $\tan\theta_1$ at $r_{\rm ref}$. The symbols θ_1, θ_2, θ_3, and h_2, h_3 are defined in Figure 4.5; $n_1 = 1.38$, $n_2 = 1.43$ and $n_3 = 1.00$ are the refractive indices of water, pentadecane and air, respectively. To obtain an error estimate, the experiments were repeated six times with different Petri dishes. The average measured displacement is $L = 15 \pm 5$ mm and the corresponding angle of the interface at $r_{\rm ref}$ is $\theta_1 = 10 \pm 4^o$.

Knowing the interface slope at this position allows us to calculate the whole profile using Eq.(4.5), which is valid when the slope is small. Here $[\partial\zeta_\infty/\partial r]^2_{\rm ref} = \tan^2(\theta_1) \simeq 0.03$ and therefore the interface is well described by Eq.(4.5) for $r \leq r_{\rm ref}$.

4.4 Results and Discussion

4.4.1 Calculations

To begin with we consider the capillary interaction between a pair of particles. As discussed in Sec. 4.2 the influence of the second particle on the interface profile near the first particle has been expressed by higher order Bessel contributions, see Eq.(4.4). The coefficients of these contributions are determined by the boundary condition along the three-phase contact line around the particle, where the contact angle is supposed to be constant.

To examine the influence of the higher order Bessel contributions to the profile, the deviation of the contact angle $\alpha_c(\vartheta)$ from the input value α_0 for two touching particles has been plotted in Figure 4.6 as a function of the angular coordinate ϑ, defined in the

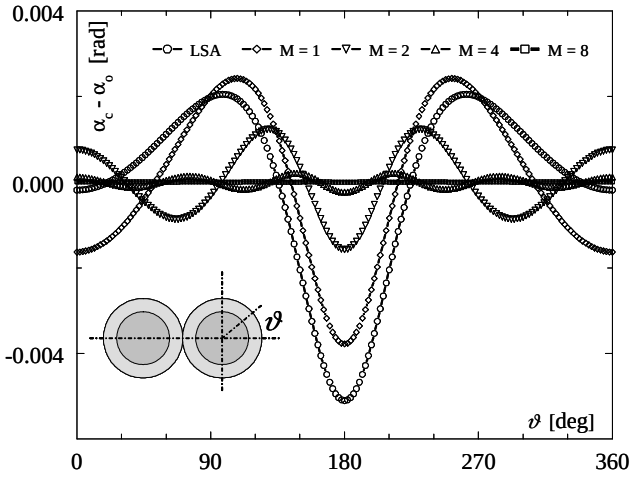

Figure 4.6: *The calculated deviation of the contact angle α_c from the input value $\alpha_0 = 40^o$ as a function of the angular coordinate ϑ, for the experimentally investigated system. Shown are the results obtained by using the LSA ($M = 0$) and the curves for $M = 1$, 2, 4 and 8.*

inset. The properties of our experimental system, listed in Table 4.1, were used in these calculations. The result for the linear superposition approximation ($M = 0$) has been shown together with the results for $M = 1$, 2, 4 and 8. Here M is the number of higher order Bessel contributions taken into account. As can be seen from the graph, including just the first order contribution hardly improves the solution. The solution requires $M \geq 4$ in order to correctly match the boundary condition. The coefficients $c_m^{(i)}$ converge to zero fairly rapidly which trend is obvious from the listed values for $c_m^{(1)}$ and $c_m^{(2)}$ in Table 4.2, for $M = 8$ and $d/R_p = 2$. Only the coefficients with positive m values have been listed because these represent the $\cos(m\vartheta)$ contributions. Due to the axial symmetry in the two-particle problem, all $\sin(m\vartheta)$ contributions (negative m values) have to be zero. We observe from the graph that even for the lowest order the deviations from the right contact angle α_0 are smaller than 1^o. Given our knowledge of $\alpha_c = 40 \pm 4^o$ this is negligible.

m	$c_{+m}^{(1)}/c_0^{(1)}$	$c_{+m}^{(2)}/c_0^{(1)}$
1	-0.00401129	0.00401129
2	0.00261464	0.00261456
3	-0.00051941	0.00051939
4	0.00009941	0.00009940
5	-0.00001940	0.00001940
6	0.00000388	0.00000388
7	-0.00000079	0.00000079
8	0.00000016	0.00000016

Table 4.2: *The values for $c_{+m}^{(i)}$ scaled by $c_0^{(1)} = -6.4897\,\mu$m for two particles in contact.*

We compared our method with the method of Paunov and coworkers [13] based on energy minimization. We calculated the capillary force between two particles for the

same situation as they considered. The parameters of their system are given in Table 4.1. They model the spherical particles as cylinders oriented perpendicular to the undisturbed interface (see the inset in Figure 4.7a).

The relative difference, $F/F_{\rm lsa}$, between the full calculation, $F(d)$, and the *LSA* calculation, $F_{\rm lsa}(d)$ was calculated as a function of the interparticle distance d, for two cases. First a constant interface slope at the approximated tpc-line was assumed, as if the particles have a cylindrical shape. The results have been plotted in Figure 4.7a. In the second case α_c was fully matched at the correct tpc-line. These results are shown in Figure 4.7b. By comparing both figures one observes that due to the simplification of the boundary conditions, the higher order Bessel contributions are strongly overestimated in Figure 4.7a. With the correct boundary condition (Figure 4.7b) the deviation from the *LSA* at contact, $d/R_p = 2$, is only 0.3, 3.6 and 10.4 % for $\alpha_c = 30$, 60 and 90^o, respectively. Hence, for all practical applications one can use the *LSA* for these systems when $\alpha_c \lesssim 60^o$. By comparing Figure 4.7a with Figure 2 of [13] one observes that our results confirm exactly the results of Paunov and coworkers, if one assumes the cylindrical approximation. However the right solution for spherical particles has been depicted in Figure 4.7b.

The results for our experimental conditions are also presented in Figure 4.7. One should note that the error introduced by using the *LSA* at small interparticle separations is less than 2 %, if the correct boundary conditions are used, as can be observed from Figure 4.7b. Hence, although the exact solution converges more slowly to the *LSA* at large distances than for the situation of [13], the approximation is useful even for small distances between the spherical particles.

Although in Figure 4.7a the force between our particles converges in the same way to the *LSA* approximation as for Paunov's system, this is not the case in Figure 4.7b. We think this is due to the weight of the particles. When the spherical boundary conditions are applied, during the separation of the particles the vertical position of the particles has to be corrected in order to obey the force balance in vertical direction. Therefore the higher order contributions to the disturbance of the interface between the two particles decays more slowly and so the interaction force. This effect is the stronger the heavier the particles. When cylindrical boundary conditions are applied this effect does not occur since the cylinders can not be adjusted in vertical direction. We checked this explanation by reducing the size (and so the weight) of our particles to that of Paunov's particles and by increasing the size of Paunov's particles that of ours. In both cases the difference in convergence, when using spherical boundary conditions, disappeared.

The proposed method is also well suited to calculate the capillary force between cylinders or hairs at a liquid-liquid interface (e.g. the hairs on a plant leaf [5]). In this case the *LSA* is not sufficient, as can be concluded from the 90^o curve in Figure 4.7a. The full solution at contact is about a factor of four larger than the *LSA* solution, and a full analysis is necessary.

In Figure 4.8 a cluster of eight particles is considered. The net capillary force on each of the eight particles is indicated by an arrow originating from the center of the particle. The difference between the full and the *LSA* solution is less than a few percent for all particles and not visible on the scale of the graph. Within this limit the capillary interaction for many particles is pair-additive. The bar in the upper left corner indicates that the forces on the particles are typically on the order of 50 nN. The arrow on the central particle points exactly to the particle which has no symmetrical counter particle (the outer right particle), a consequence of the fact that the net force on each particle is

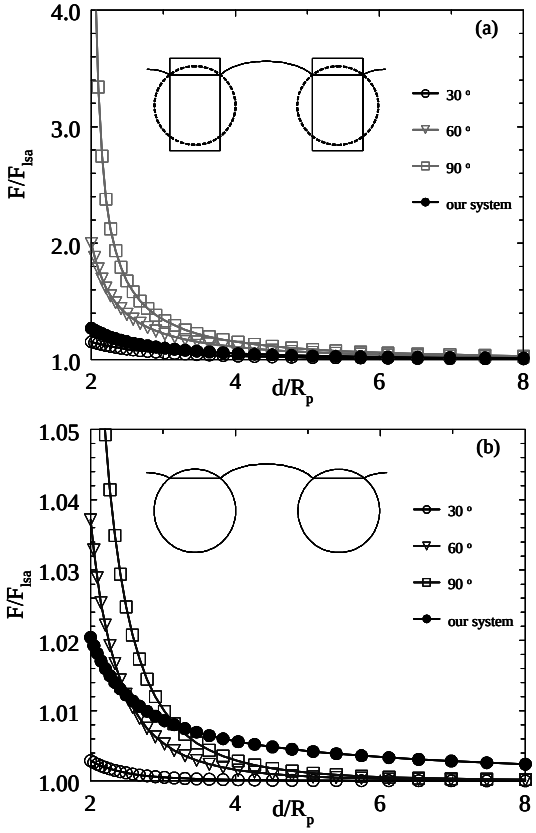

Figure 4.7: *Plot of the ratio of the exact force and the LSA force, F/F_{lsa}, as a function of the interparticle distance d/R_p, for the system of ref.* [13]*, with $\alpha_c = 30$, 60 and 90^o, and our system with $\alpha_c = 40^o$; in (a) the calculations were done using the cylindrical boundary condition, in (b) using the spherical boundary condition.*

simply the sum of all pair interactions.

4.4.2 Experimental results

- A single particle

When a single particle is placed at the interface, it starts to move towards the center of the dish along an approximately straight line. The radial velocity of the particle is shown in Figure 4.9 for 8 independent experiments.

The particle velocities are higher in the initial stages (at larger r values) and gradually diminish to zero when the particle reaches the center of the dish. This is due to the capillary interaction with the background profile. By comparing the measured velocity with the theoretical prediction, Eq.(4.14), we obtain the correction coefficient f_d. The interaction between the particle and the background profile $\underline{\mathrm{F}}_{\mathrm{lsa}}^{[\mathrm{bg}]}$ is given by Eq.(4.11).

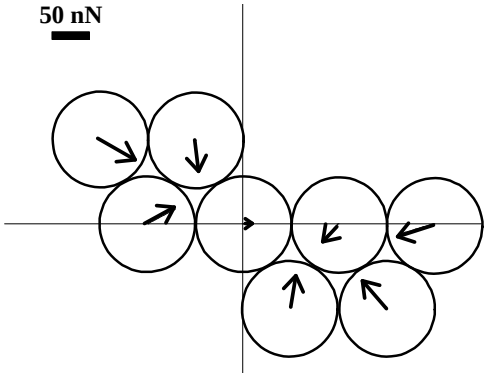

Figure 4.8: *The calculated interactions between particles in a stationary 8-particle aggregate. The arrows indicate the net force on the particles. The difference between the LSA and the exact solution is less than 2 % and is not visible on this scale.*

Combining both equations one obtains the following expression:

$$v(r) = \frac{-\gamma Q_p Q_d \, q \, \mathrm{I}_1(qr)}{3\eta \, R_p \, f_d} \tag{4.15}$$

where Q_p and Q_d have been defined in Eqs.(4.10) and (4.12), respectively.

The curve in Figure 4.9 represents Eq.(4.15), which contains only one unknown parameter, f_d. We find $f_d = 1.4 \pm 0.5$, which is of the same order of magnitude as our estimate in Sec. 4.3. The uncertainty in f_d is mainly due to the inaccuracy of the measured background slope at the reference point: $\theta_1 = 10 \pm 4°$, which affects the accuracy of Q_d.

- Interacting particles

When a second particle is introduced, it will also move towards the center of the dish. However, instead of going to zero as the particle nears the center (and the first particle), the velocity increases when the particle approaches the middle of the dish. Initially the particle shows the same behavior as the first particle due to the background force. However, for distances smaller than half of the dish radius the attractive interaction force with the other particle, $\underline{\mathrm{F}}_{\mathrm{lsa}}^{[1,2]}$, becomes dominant and the velocity increases rapidly. In Figure 4.10 the relative velocity $v_{\mathrm{rel}} = v_1 - v_2$ has been plotted as a function of the distance d between the two particles, again for a series of 8 independent measurements. To explain the observed dependence of v_{rel} on d, the forces acting on both particles are considered:

$$\underline{\mathrm{F}}_d^{[1]} = \underline{\mathrm{F}}_{\mathrm{lsa}}^{[\mathrm{bg}]}(\underline{\mathrm{r}}_1) + \underline{\mathrm{F}}_{\mathrm{lsa}}^{[1,2]}(\underline{\mathrm{d}}) \tag{4.16}$$

$$\underline{\mathrm{F}}_d^{[2]} = \underline{\mathrm{F}}_{\mathrm{lsa}}^{[\mathrm{bg}]}(\underline{\mathrm{r}}_2) + \underline{\mathrm{F}}_{\mathrm{lsa}}^{[2,1]}(\underline{\mathrm{d}}) \tag{4.17}$$

where $\underline{\mathrm{d}} = \underline{\mathrm{r}}_1 - \underline{\mathrm{r}}_2$ and $\underline{\mathrm{F}}_{\mathrm{lsa}}^{[\mathrm{bg}]}$ is again the background force, Eq.(4.11). The capillary interaction force $\underline{\mathrm{F}}_{\mathrm{lsa}}^{[1,2]}(\underline{\mathrm{d}})$ between the two particles in the *LSA* is given by Eq.(4.9). $\underline{\mathrm{F}}_d$ is the drag force on particle 1 or 2, respectively.

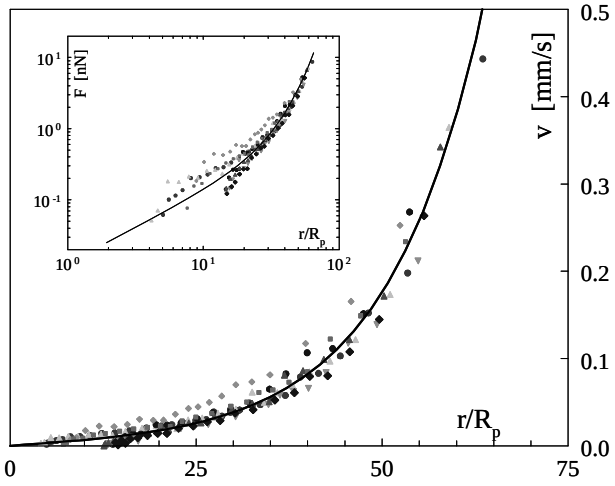

Figure 4.9: *The measured velocity $v(r)$ of a single particle in a Petri dish as a function of the radial distance r from the center of the dish. The different symbols represent 8 different measurements. The curve is the best fit of Eq.(4.15) resulting in $f_d = 1.4 \pm 0.5$. The inset shows the corresponding force as a function of r, on a log-log scale.*

When the particles are moving towards each other, they also interacts hydrodynamically; the drag force on the first particle depends not only on its own velocity but also on that of the second particle. Since the particles approach each other along a center line of the Petri dish, the problem is one dimensional and the velocities of particles 1 and 2 are given by [1]:

$$\begin{aligned} 6\pi\eta\, R_p\, f_d\, v_1 &= A_{11}(d)F_d^{[1]} + A_{12}(d)F_d^{[2]} \\ 6\pi\eta\, R_p\, f_d\, v_2 &= A_{21}(d)F_d^{[1]} + A_{22}(d)F_d^{[2]} \end{aligned}$$

where $A_{ij}(d)$ are the hydrodynamic mobility functions along the line of centers. For equal sized particles symmetry arguments show that $A_{11} = A_{22}$ and $A_{12} = A_{21}$. Moreover $\lim_{x\to\infty} A_{ij}(x) = \delta_{ij}$ where $\delta_{ij} = 1$ if $i = j$ and $\delta_{ij} = 0$ otherwise. Taking the difference of the last two equations and using Eqs.(4.16) and (4.17) one obtains the relative velocity $v_{\rm rel} = v_1 - v_2$:

$$v_{\rm rel} = G\left(\frac{2F_{\rm lsa}^{[1,2]}(d) + F_{\rm lsa}^{[\rm bg]}(r_1) - F_{\rm lsa}^{[\rm bg]}(r_2)}{6\pi\eta\, R_p\, f_d}\right)$$

where $G = A_{11} - A_{12}$. Since $dF_{\rm lsa}^{[\rm dish]}/dr \ll F_{\rm lsa}^{[1,2]}(d)/d$ near the center of the dish, the contribution of the background force can be neglected and the following expression for the relative velocity as a function of the interparticle distance is obtained:

$$v_{rel} = \frac{2\gamma\, Q_p^2\, q\, {\rm K}_1(qd)}{3\eta R_p f_d} G(d) \tag{4.18}$$

where Eq.(4.9) has been used for the interparticle force. The function $G(d)$ was tabulated by Batchelor [32]. An interpolation formula for these tabulated data that shows the

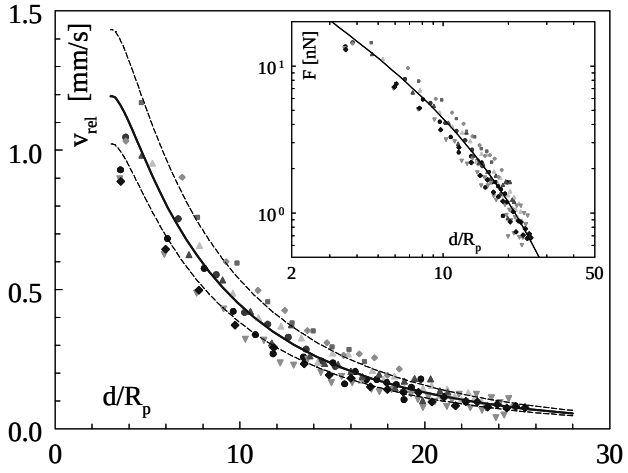

Figure 4.10: *The measured velocity v_{rel} as a function of the interparticle distance d between two particles in a Petri dish. The different symbols represent 8 different measurements. The black curve is the best fit of Eq.(4.18) resulting in $f_d = 1.2 \pm 0.2$. The dashed curves represent the error bounds on this fit. The inset shows the corresponding inter-particle force as a function of r, on a log-log scale.*

correct asymptotic behavior for both $x \to 2$ and $x \to \infty$ is given by:

$$G(x) = 1 - \tfrac{3}{2}x^{-1} + x^{-3} - \tfrac{15}{4}x^{-4} - \tfrac{4.46}{1000}\left(x - 1.7\right)^{-2.867}$$

with $x = d/R_p$. The curve in Figure 4.10 represents Eq.(4.18). Again, there is only a single unknown parameter, f_d, which is used as a fitting parameter. The best fit is been obtained for $f_d = 1.2 \pm 0.2$, which is in agreement with the value found from the fit in Figure 4.9. The uncertainty of 0.2 is mainly due to the spread of the experimental data points.

We received similar f_d values for a single particle and two interacting particles. This was expected because we use the same particles and liquid phases in both experiments. According to [33], the drag on a particle at a liquid-liquid interface is a function of the viscosity of the two liquids and the three phase contact angle only. Hence we expected the agreement between the two experiments.

In our case f_d is slightly bigger than one. Petkov and coworkers [18] report values of f_d for the water-air interface. Depending on the contact angle they measured drag coefficients between 0.54 and 0.68 for glass particles. Drag coefficients larger than unity were received when surfactant was added ($f_d = 1.6$) or heavier copper beads were used ($f_d = 1.77$). Danov and coworkers [34] developed a theory for the drag of a solid sphere moving at spherical or flat interface for Stokes flow. They compute numerically the translational drag force and hydrodynamic torque acting on a particle as a function of the particle position at the liquid-liquid interface for several viscosity ratio's and viscous or nonviscous interfaces. The friction coefficient received by us (viscosity ratio of one) is in agreement with their theory (see Figure 5 in [34]).

4.5 Conclusions

We are able to calculate the capillary interactions between several objects at a liquid-liquid interface. The proposed approach is universal and can be used to describe the interactions between a particle and a larger aggregate or to describe the interaction between a particle and cylindrical walls, as in a Couette device. The only restriction is that the interface curvature in the region of interest should be small. In Sec.4.2.1 we showed that for submillimeter-sized particles the disturbance to a flat interface due to the presence of particles causes a slope $|\underline{\nabla}\zeta| \ll 1$. The slope of the background profile due to the geometry of the container can be larger than one. However, because the particles will collect in a region of low curvature, the gradient $\underline{\nabla}\zeta$ in this region is also small. This restriction is therefore not a severe limitation of the method for the considered systems.

In our calculations we considered spheres as well as cylinders at a liquid-liquid interface. For two cylinders at small separations the Linear Superposition Approximation, *LSA*, strongly underestimates the capillary force, and one should use the full calculation as described in Sec. 4.2. With this method capillary problems can be addressed like the wetting of hairy plant tissues [5], where the wetting is controlled by the capillary interactions between the hairs and their deformation.

However, for spheres it was shown that the *LSA* can be used, even at very small separations between the particles. It introduces a small error, less than 2 %, but considerably lowers the computational efforts. The method is well suited to describe many particle capillary interaction. Because the *LSA* holds for spherical particles, this interaction is simply pair wise additive.

The theoretical results for one sphere and a pair of spheres at an interface with background curvature are corroborated by our experimental results as shown in Figures 4.9 and 4.10. The capillary force on a particle at the liquid-liquid interface was estimated by measuring the particle velocities, taking into account the non-negligible hydrodynamic interaction between the approaching particles. The best value for the fitting parameter in the expression for the drag force is $f_d = 1.2 \pm 0.2$. This indicates that the presence of the liquid-liquid interface enhances the drag force on the particles only slightly. This value for f_d is in agreement with the value calculated by Danov *et al.*[34] for similar conditions as ours.

The experimental method is restricted to non-colloidal particles because negligible thermal motion of the particles is required to obtain reproducible results. Moreover, very small distances between the particles cannot be probed due to the limitations of the optical microscopy technique. On the other hand, the experimental procedure is simple and does not require any attachment of the particles which could influence their position at the interface. This simple approach can be used also for measuring the capillary interactions between multiple particles.

Acknowledgment.We thank Dr. I. Carpen for critically reading the manuscript and her valuable remarks. This work has been supported by the Foundation for Fundamental Research on Matter (FOM), which is financially supported by the Netherlands Organization for Scientific Research (NWO).

Appendix 4A. Interface slope at the tpc-line

In the derivation given in Sec.4.2 the liquid-liquid interface is described in cylindrical coordinates (r, ϑ, z) by $z = f(r, \vartheta)$. However, to describe the tpc-line along a particle,

the interface near that spherical particle can be expressed most conveniently in spherical coordinates (R, ϑ, β) as $\beta = h(R, \vartheta)$. The slope of the tpc-line along the sphere with respect to the horizontal plane is given by $\tan\phi = (-Rd\beta)/(R\sin\beta d\vartheta) = -h_\vartheta/\sin\beta$, where $h_\vartheta = \partial h/\partial\vartheta$. A third orthogonal coordinate system is introduced to describe the contact angle and the resulting surface tension force on the wall at a certain point P on the tpc-line, see also Figure 4.2:

$$\begin{aligned}
\underline{\mathrm{e}}_\xi &= \underline{\mathrm{e}}_R \\
\underline{\mathrm{e}}_\eta &= \cos\phi\,\underline{\mathrm{e}}_\vartheta - \sin\phi\,\underline{\mathrm{e}}_\beta \\
\underline{\mathrm{e}}_\zeta &= -\sin\phi\,\underline{\mathrm{e}}_\vartheta - \cos\phi\,\underline{\mathrm{e}}_\beta \\
\\
\underline{\mathrm{e}}_R &= \sin\beta\underline{\mathrm{e}}_r + \cos\beta\underline{\mathrm{e}}_z \\
\underline{\mathrm{e}}_\vartheta &= \underline{\mathrm{e}}_\vartheta \\
\underline{\mathrm{e}}_\beta &= \cos\beta\underline{\mathrm{e}}_r - \sin\beta\underline{\mathrm{e}}_z
\end{aligned}$$

In the (ξ, η, ζ) coordinate system the interface is described by $\zeta = g(\xi, \eta)$, where at the point P the η-axis is parallel to both the liquid-liquid interface and the spherical surface while the ξ-axis (ζ-axis) is normal (parallel) to the spherical surface. In this geometry the contact angle α_c is defined by

$$\tan(\alpha_c - \pi/2) = \partial g/\partial\xi = g_\xi$$

while the unit vector in the interface perpendicular to the tpc-line is given by:

$$\underline{\mathrm{e}}_F = \sin\alpha_c\,\underline{\mathrm{e}}_\xi - \cos\alpha_c\,\underline{\mathrm{e}}_\zeta \tag{4.19}$$

This unit vector points in the direction of the surface tension force. In order to express α_c in the r, ϑ, z coordinates we compare the representation of $d\underline{\mathrm{r}}$ in the three coordinate systems:

$$\begin{aligned}
d\underline{\mathrm{r}} &= dr\,\underline{\mathrm{e}}_r + rd\vartheta\,\underline{\mathrm{e}}_\vartheta + df\underline{\mathrm{e}}_z \\
&= dR\underline{\mathrm{e}}_R + R\sin\beta d\vartheta\,\underline{\mathrm{e}}_\vartheta + Rdh\underline{\mathrm{e}}_\beta \\
&= d\xi\,\underline{\mathrm{e}}_\xi + d\eta\,\underline{\mathrm{e}}_\eta + dg\,\underline{\mathrm{e}}_\zeta
\end{aligned}$$

By expressing $(\underline{\mathrm{e}}_r, \underline{\mathrm{e}}_\vartheta, \underline{\mathrm{e}}_z)$ in $\left(\underline{\mathrm{e}}_R, \underline{\mathrm{e}}_\vartheta, \underline{\mathrm{e}}_\beta\right)$ and $\left(\underline{\mathrm{e}}_R, \underline{\mathrm{e}}_\vartheta, \underline{\mathrm{e}}_\beta\right)$ in $\left(\underline{\mathrm{e}}_\xi, \underline{\mathrm{e}}_\eta, \underline{\mathrm{e}}_\zeta\right)$ one obtains:

$$\begin{aligned}
dR &= dr\,\sin\beta + df\,\cos\beta \\
R\sin\beta d\vartheta &= rd\vartheta \\
Rdh &= dr\,\cos\beta - df\,\sin\beta \\
\\
d\xi &= dR \\
d\eta &= R\sin\beta d\vartheta\cos\phi - Rdh\sin\phi \\
dg &= -R\sin\beta d\vartheta\sin\phi - Rdh\cos\phi
\end{aligned}$$

From the last equation one can calculate $\partial g/\partial\xi = g_\xi$:

$$g_\xi = \left(\frac{-R\sin\beta d\vartheta\sin\phi - Rdh\cos\phi}{dR}\right)_{d\eta=0}$$

Because $d\eta = R\sin\beta d\vartheta\cos\phi - Rdh\sin\phi = 0$ one obtains:

$$d\vartheta = \frac{h_R\tan\phi}{\sin\beta - h_\vartheta\tan\phi}dR$$

and, with $\tan\phi = -h_\vartheta/\sin\beta$:

$$\begin{aligned} g_\xi &= \frac{-R\sin\beta d\vartheta\sin\phi - Rdh\cos\phi}{dR} \\ &= \frac{-R\sin\beta\, h_R}{\sqrt{\sin^2\beta + h_\vartheta^2}} \end{aligned}$$

Next one has to express h_R and h_ϑ in $f(r,\vartheta)$:

$$\begin{aligned} h_R &= \left(\frac{dh}{dR}\right)_{d\vartheta=0} = \frac{\cos\beta - f_r\,\sin\beta}{R\,(\sin\beta + f_r\,\cos\beta)} \\ h_\vartheta &= \left(\frac{dh}{d\vartheta}\right)_{dR=0} = \frac{-f_\vartheta}{R\,(\sin\beta + f_r\cos\beta)} \end{aligned}$$

Hence the contact angle α_c is related to $\partial\zeta/\partial r$ and $\partial\zeta/\partial\vartheta$ according to the relation:

$$\cot(\alpha_c) = \frac{\cos\beta - f_r\,\sin\beta}{\sqrt{(\sin\beta + f_r\,\cos\beta)^2 + (f_\vartheta/r)^2}} \tag{4.20}$$

Appendix 4B. Calculation of $c_m^{(i)}$

The coefficients $c_m^{(i)}$ can be determined from the boundary conditions on the particles. The liquid-liquid interface should contact the particle in such a way that the contact angle α_c is constant along the tpc-line. In Eq.(4.20) α_c has been expressed in the interface slope, where $\beta(\vartheta) = \arctan\left(r_c/\left(\zeta_c - \zeta_M\right)\right)$ and r_c is defined by $r_c^2 + (\zeta_c - \zeta_M)^2 = R_p$; ζ_M is the z-coordinate of the center of the particle:

$$z_M = \frac{1}{2\pi}\int_0^{2\pi} \zeta\left(R_P\sin\beta_0, \vartheta\right)\, d\vartheta - R_P\cos\beta_0 \tag{4.21}$$

where β_0 and $\zeta_c = \zeta(r_c,\vartheta)$ are given in Figure 4.1. One therefore has to consider the slope $f_r = \partial\zeta/\partial r$ at the surface of the particle. Again under the assumption that the spatial derivatives of $\zeta(r,\vartheta)$ are small, it follows from Eq.(4.20) that:

$$\left(\frac{\partial\zeta}{\partial r_j}\right)_{r_c^{(j)}} = \frac{\tan\alpha_c - \tan\beta_j}{1 + \tan\alpha_c\tan\beta_j} - \frac{(f_\vartheta/r)_j^2}{2\tan\alpha_c}$$

and also:

$$\left(\frac{\partial\zeta}{\partial r_j}\right)_{r_c^{(j)}} = \sum_{m=-\infty}^{\infty}\left(c_m^{(0)}\left[\frac{\partial P_m(r,\vartheta)}{\partial r_j}\right]_{r_c^{(j)}} + \sum_{i=1}^{N} c_m^{(i)}\left[\frac{\partial Q_m(r_i,\vartheta_i)}{\partial r_j}\right]_{r_c^{(j)}}\right) \tag{4.22}$$

From the boundary condition on the rim of the dish we obtain:

$$\left(\frac{\partial\zeta}{\partial r}\right)_{r_{\rm ref}} = \sum_{m=-\infty}^{\infty}\left(c_m^{(0)}\left[\frac{\partial P_m(r,\vartheta)}{\partial r_j}\right]_{r_{\rm ref}} + \sum_{i=1}^{N} c_m^{(i)}\left[\frac{\partial Q_m(r_i,\vartheta_i)}{\partial r_j}\right]_{r_{\rm ref}}\right) \tag{4.23}$$

In Eqs.(4.22) and (4.23) both the left and right hand sides are functions of ϑ_j; therefore the coordinates (r_i,ϑ_i) should be expressed in r_j and ϑ_j where $r_j = r_c(\vartheta_j)$. To compare

the ϑ_j dependence of the left and right hand sides of these equations, they have been expanded in a Fourier series:

$$\begin{aligned} A_0^{(j)} &+ \sum_{k=1}^{\infty} \left[A_k^{(j)} \cos(k\vartheta_j) + A_{-k}^{(j)} \sin(k\vartheta_j) \right] \\ &= \sum_{i=0}^{N} \sum_{m=-\infty}^{\infty} c_m^{(i)} \left(B_{m,0}^{(i,j)} + \sum_{k=1}^{\infty} \left[B_{m,k}^{(i,j)} \cos(k\vartheta_j) + B_{m,-k}^{(i,j)} \sin(k\vartheta_j) \right] \right) \end{aligned} \tag{4.24}$$

where for $j > 0$:

$$A_k^{(j)} = \frac{1}{\pi} \int_0^{2\pi} \left(\frac{\partial \zeta}{\partial r_j} \right)_{r_c^{(j)}} \mathcal{H}(k,\vartheta)\, d\vartheta$$

with $\mathcal{H}(k,\vartheta) = \cos(k\vartheta)$ for $k > 0$, $\mathcal{H}(k,\vartheta) = 1/2$ for $k = 0$ and $\mathcal{H}(k,\vartheta) = \sin(-k\vartheta)$ for $k < 0$. The coefficients $B_{m,k}^{(i,j)}$ are defined by:

$$B_{m,k}^{(i,j)} = \frac{1}{\pi} \int_0^{2\pi} \left[\frac{\partial Q_m(r_i,\vartheta_i)}{\partial r_j} \right]_{r_c^{(j)}} \mathcal{H}(k,\vartheta)\, d\vartheta$$

for $i > 0$. Moreover:

$$\begin{aligned} A_k^{(0)} &= \delta_{k0} \left(\frac{\partial \zeta}{\partial r} \right)_{r_{\rm ref}} \\ B_{m,k}^{(0,j)} &= \frac{1}{\pi} \int_0^{2\pi} \left[\frac{\partial P_m(r,\vartheta)}{\partial r_j} \right]_{r_c^{(j)}} \mathcal{H}(k,\vartheta_j)\, d\vartheta_j \end{aligned}$$

with $\delta_{k0} = 1$ if $k = 0$ and $\delta_{k0} = 0$ otherwise. Both sides of Eq.(4.24) are identical if all the individual $\cos(k\vartheta_j)$ and $\sin(k\vartheta_j)$ terms in the summation are identical, which results in a set of equations for the unknowns $c_m^{(i)}$:

$$\sum_{i=0}^{N} \sum_{m=-M}^{M} c_m^{(i)} B_{m,k}^{(i,j)} = A_k^{(j)} \tag{4.25}$$

where we have assumed that the series $c_{\pm m}^{(i)}$ converge to 0 for $m \gg 1$ and the summation can be stopped at $m = M$. Note that the coefficients $A_k^{(j)}$ and $B_{m,k}^{(i,j)}$ (weakly) depend on the coefficients $c_m^{(i)}$ via the calculation of $r_j = r_c(\vartheta_j)$, hence the problem is not linear. The set of Eqs.(4.25) can be solved iteratively because $B_{k,k}^{(j,j)} \geq B_{m,k}^{(i,j)}$ for all i, j, m and k. Since the monopole solution is given by:

$$\begin{aligned} c_k^{(0)}(mp) &= \delta_{k0} \frac{\tan\phi_{bg} \mathrm{I}_0(q r_{\rm dish})}{q\, \mathrm{I}_1(q r_{\rm dish})} \\ c_k^{(j)}(mp) &= \delta_{k0} \frac{-\tan\phi_c \mathrm{K}_0(q R_p)}{q\, \mathrm{K}_1(q r_c^{(o)})} \end{aligned}$$

these values are used as starting values. The updating step is constructed from:

$$c_k^{(j)} B_{k,k}^{(j,j)} = A_k^{(j)} - \sum_{i \neq j} \sum_m c_m^{(i)} B_{m,k}^{(i,j)} - \sum_{m \neq k} c_m^{(j)} B_{m,k}^{(j,j)}$$

Because the coefficients $A_k^{(j)}$ and $B_{m,k}^{(i,j)}$ depend on $c_m^{(i)}$ these coefficients should be recalculated before every updating step. Now the calculation scheme is complete and reads as follows:

1. Start
2. Initiate for all j and k : $c_k^{*(j)} := c_k^{(j)}(mp)$
3. For all j and k : $c_k^{(j)} := c_k^{*(j)}$
4. Calculate for all i, j, k and m : $A_k^{(j)}$ and $B_{m,k}^{(i,j)}$
5. For all j and k :
$$c_k^{*(j)} = \frac{A_k^{(j)} - \sum\limits_{i,m} c_m^{(i)} B_{m,k}^{(i,j)} \left(1 - \delta_{ij}\delta_{mk}\right)}{B_{k,k}^{(j,j)}}$$
6. If for any j and k : $\left|c_k^{*(j)} - c_k^{(j)}\right| > \epsilon$ go to step 3.
7. Stop

Although the algorithm works fine it becomes more efficient, without significant loss of numerical accuracy, when the slope $\partial\zeta/\partial r$ is evaluated not at the actual tpc-line $r_c^{(j)}(\vartheta)$, but at a fixed radius $r_c^{(o)} = R_p \sin\beta_0$, by applying a Taylor expansion. In this case the coefficients $B_{m,k}^{(i,j)}$ become independent of the coefficients $c_m^{(i)}$ and have to be calculated only once.

Appendix 4C. Calculation of $\underline{\mathrm{F}}^{[\mathrm{cap}]}$

To obtain an expression for the interfacial tension force on a spherical particle, one has to evaluate Eq.(4.19)

$$\underline{\mathrm{e}}_F = \sin\alpha_c\, \underline{\mathrm{e}}_R + \cos\alpha_c \left(\sin\phi\, \underline{\mathrm{e}}_\vartheta + \cos\phi\, \underline{\mathrm{e}}_\beta\right) \tag{4.26}$$

with

$$\begin{aligned} \sin\phi &= \frac{f_\vartheta/r}{\sqrt{\left(\sin\beta + f_r\, \cos\beta\right)^2 + \left(f_\vartheta/r\right)^2}} \\ \cos\phi &= \frac{\sin\beta + f_r\, \cos\beta}{\sqrt{\left(\sin\beta + f_r\, \cos\beta\right)^2 + \left(f_\vartheta/r\right)^2}} \end{aligned}$$

Evaluating Eq.(4.26) one obtains:

$$\underline{\mathrm{e}}_F = n_x(\vartheta)\underline{\mathrm{e}}_x + n_y(\vartheta)\underline{\mathrm{e}}_y + n_z(\vartheta)\underline{\mathrm{e}}_z$$

with

$$\begin{aligned} n_x(\vartheta) &= \sin\alpha_c \sin\beta\cos\vartheta \\ &- \cos\alpha_c \left(\sin\phi\sin\vartheta + \cos\phi\cos\beta\cos\vartheta\right) \\ n_y(\vartheta) &= \sin\alpha_c \sin\beta\sin\vartheta \\ &+ \cos\alpha_c \left(\sin\phi\cos\vartheta + \cos\phi\cos\beta\sin\vartheta\right) \\ n_z(\vartheta) &= \sin\alpha_c \cos\beta - \cos\alpha_c\cos\phi\sin\beta \end{aligned} \tag{4.27}$$

where $\beta(\vartheta)$ can be expressed in terms of f_r and f_ϑ:

$$\tan\beta = \frac{\tan^2\alpha_c - \frac{1}{2}\left(f_\vartheta/r\right)^2 - f_r\,\tan\alpha_c}{\tan\alpha_c\left(1+\frac{1}{2}\left(f_\vartheta/r\right)^2 + f_r\,\tan\alpha_c\right)} \tag{4.28}$$

Moreover the infinitesimal length dl is given by:

$$dl = \left(R\sin\beta\, d\vartheta\right)/\left(\cos\phi\right) \tag{4.29}$$

so that the force contribution $d\underline{\mathrm{F}}^{[\gamma]}$ is given by:

$$d\underline{\mathrm{F}}^{[\gamma]} = \gamma dl\,\underline{\mathrm{e}}_F = \frac{\gamma R\sin\beta}{\cos\phi}\,\underline{\mathrm{e}}_F\,d\vartheta \tag{4.30}$$

Integrating this equation over ϑ yields the net surface tension force $\underline{\mathrm{F}}^{[\gamma]}$ on the particle with radius R.

The contribution of the pressure distribution over the particle surface is :

$$\underline{\mathrm{F}}^{[p]} = -\int_0^{2\pi}\int_0^{\pi} p(\chi,\vartheta)R_p^2\underline{\mathrm{e}}_R\,\sin\chi\,d\chi\,d\vartheta$$

where $p(\chi,\vartheta) = p_0 + gR_p\,\rho\,(z_M+\cos\chi)$ with p_0 a reference pressure, z_M the z-coordinate of the center of the particle and $\rho=\rho_u$ for $0<\chi<\beta(\vartheta)$ and $\rho=\rho_l$ for $\beta(\vartheta)<\chi<\pi$, χ being the azimuth with respect to the z-axis. The tpc-line along the particle is defined by $\beta(\vartheta)$ as given in Eq.(4.28). The value for z_M in this expression is obtained from Eq.(4.21). Finally the capillary force is obtained from:

$$\underline{\mathrm{F}}^{[\mathrm{cap}]} = \int_0^{2\pi}\frac{\gamma R\sin\beta}{\cos\phi}\,\underline{\mathrm{e}}_F\,d\vartheta + \underline{\mathrm{F}}^{[p]}$$

This force has been calculated numerically using an integration algorithm based on a Gaussian quadrature. All the programming was done in C using the lcc-win32 package (free available and described by Jacob Navia, Q Software Solutions GmbH).

References

[1] Russel, W.B.; Saville, D.A.; Schowalter, W.R. *Colloidal dispersions*, Cambridge University Press: Cambridge, **1989**.

[2] Tadros, Th.F. *Solid-liquid dispersion*, Academic press, **1987**.

[3] Wills B.A., *Mineral processing technology*, 6th ed.; Oxford: Butterworth-Heinemann, **1997**.

[4] Fendler, J.H. *Curr. Opin. Colloid Interface Sci.* **1996**, 1(2), 202-207.

[5] Otten A., Herminghaus S. *Langmuir*, **2004**, 20, 2405-2408.

[6] Kim K.S. Neu J., Oster G. *Biophysical J.* **1998**, 75, 2274-2291.

[7] Whitesides G.M. Grzybowski B. *Science* **2002**, 295, 2418-2421.

[8] Boucher, E.A.; Evans, M.J.; Jones, T.G.J. *Adv. Colloid Interface Sci.* **1987**, 27(1-2), 43-79.

[9] Nicolson, M.M. *Proc. Cambridge Philos. Soc.* **1949**, 45, 288-295.

[10] Chan, D.Y.C.; Henry, J.D.; White, L.R. *J. Colloid Interface Sci.* **1981**, 79, 411-418.

[11] Kralchevsky, P.A.; Nagayama K. *Particles at fluid interfaces and membranes:* Attachment of Colloid Particles and Proteins to Interfaces and Formation of Two-Dimensional Arrays , Elsevier:Amsterdam, **2001**.

[12] Kralchevsky, P.A.; Nagayama, K. *Adv. Colloid Interface Sci.* **2000**, 85, 145-192.

[13] Paunov, V.N.; Kralchevsky, P.A.; Denkov, N.D.; Nagayama, K. *J. Colloid Interface Sci.* **1993**, 157, 100-112.

[14] Stamou, D.; Duschl, C.; Johannsman, D. *Phys. Rev. E* **2000**, 62, 5263-5272.

[15] Kralchevsky, P.A.; Denkov, N.D.; Danov, K.D. *Langmuir* **2001**, 17, 7694-7705.

[16] Fournier, J.-B.; Galatola, P. *Phys. Rev. E* **2002**, 65, 031601.

[17] Velev, O.D.; Denkov, N.D.; Paunov, V.N.; Kralchevsky, P.A.; Nagayama, K. *J. Colloid Interface Sci.* **1994**, 167, 66-73.

[18] Petkov, J.T.; Denkov, N.D; Danov, K.D.; Velev, O.D.; Aust, R., Durst, F.; *J. Colloid Interface Sci.* **1995**, 172, 147-154.

[19] Joseph, D.D.; Wang, J.; Bai, R.; Yang, B.H. *J. Fluid Mech.* **2003**, 496, 139-163.

[20] Vincze, A.; Agod, A.; Kertesz, J.; Zrinyi, M.; Horvolgyi, Z. *J. Chem. Phys.* **2001**, 114, 520-529.

[21] Velev, O.D.; Denkov, N.D.; Paunov, V.N.; Kralchevsky, P.A.; Nagayama, K., *Langmuir* **1993**, 9, 3702-3709.

[22] Dushkin, C.D.; Kralchevsky, P.A.; Paunov, V.N.; Yoshimura, H.; Nagayama, K. *Langmuir* **1996**, 12, 641-651.

[23] Vassileva, N.D.; D. van den Ende, *Proceedings of The XIV international congress on Rheology*, **2004**.

[24] Kralchevsky, P.A.; Paunov,V.N.; Ivanov, I.B.; Nagayama, K. *J. Colloid Interface Sci.* **1992**, 151(1), 79-94.

[25] Moon, P.; Spencer, D.E. *Field theory handbook, including coordinate systems, differential equations, and their solutions*, 2nd ed.; Springer-Verlag: New York, **1988**.

[26] Aveyard, R.; Binks, B.P.; Clint, J.P.; Fletcher, P.D.I.; Neumann B., Paunov V.N. *Langmuir* **2002**, 18, 9587-9593.

[27] Princen, H.M. *The equilibrium shape of interfaces, drops, and bubbles. Rigid and deformable particles at interfaces*, In: Surface and colloid science (ed Matijevic E) Vol. 2; Wiley-Interscience: New York, **1969**.

[28] Nikolaides, M.G ; Bausch, A.R.; Hsu, M.F.; Dinsmore, A.D.; Brenner, M.P.; Gay, G.; Weitz, D.A. *Nature* **2002**, 420, 299-301.

[29] Danov, K.D.; Kralchevsky, P.A.;Boneva, P. *Langmuir* **2004**, 20, 6139-6151.

[30] Merzkirch W. *Flow visualization*, Academic Press:London, **1974**.

[31] Lange, P.A. *Rev. Sci. Instrum.* **1982**, 53, 651-655.

[32] Batchelor, G.K. *J. Fluid Mech.* **1976**, 74, 1-29.

[33] Danov, K.D.; Aust, R.; Durst, F.; Lange, U. *J. Colloid Interface Sci.* **1995**, 175, 36-45.

[34] Danov, K.D.; Dimova, R.; Pouligny, B. *Physics of fluids* , **2000**, 12, 2711-2722.

Chapter 5

Restructuring and break-up of two-dimensional aggregates in shear flow*

Abstract

We consider single two-dimensional aggregates, containing glass particles, placed at a water/air interface. We have investigated the critical shear rate for break-up of aggregates with different sizes in a simple shear flow. All aggregates break-up nearly at the same shear rate (1.8 $\pm$ 0.2 s^{-1}) independent of their size. The evolution of the aggregate structure before break-up was also investigated. With increasing shear rate the aggregates adopt a more circular shape, and the particles order in a more dense, hexagonal structure. A simple theoretical model was developed to explain the experimental observed break-up. In the model the aggregate is considered as solid circular disk that will break near its diameter. The capillary and drag force on the two parts of the aggregate were calculated and from this force balance the critical shear rate was found. The model shows a weak size dependence of the critical shear rate for the considered aggregates. This is consistent with the experimental observations.

5.1 Introduction

In many disperse systems with practical importance (paints, dairy products) we observe the formation of aggregates of particles [1, 2]. Aggregate behavior is also an important issue in many solid-liquid separation processes as mineral processing or waste water treatment [3, 4], where one has to deal with both colloidal and non-colloidal particles. Another area of application is the use of particles (organized in 2D structures) as stabilizing agents of foams and emulsions (known as Pickering emulsions) encountered in many industrial and natural processes such as food, cosmetic and pharmaceutical products. To improve the properties of these products or the efficiency of these processes one needs a detailed knowledge of the behavior and properties of the aggregates involved. The behavior of an aggregate in shear flow is a complex phenomenon. The aggregate may deform, restructure or break-up. Our goal is to find the relationship between the aggregate changes and the shear flow. We are studying aggregates confined at a liquid-air interface. Their motion in

*This chapter has been published in *Langmuir* **2006**, 22, 4959.

vertical direction is strongly restricted, thus they can be considered as two-dimensional (2D). These 2D aggregates are used as a model for three-dimensional (3D) suspensions, because they are more convenient for investigation. They can easily be observed and analyzed with conventional techniques.

When a 3D aggregate is subjected to a shear flow the hydrodynamic stresses acting on its surface may cause break-up of the aggregate if they exceed the attraction forces between the particles. Two general break-up mechanisms have been identified: "erosion" and "rupture". Erosion consists of shearing off single particles or small fragments from the aggregate surface while rupture means breaking of the aggregate in two or more large parts. It is believed that different forces are responsible for the two mechanisms. The erosion is caused by the shear force of the fluid on the surface of the aggregate. It is a slow process and dominates at moderate stresses. Rupture occurs when the hydrodynamic stress exceed the cohesive force and is assumed to be caused by the pressure difference inside the aggregate [5, 6].

In the 3D break-up models proposed in literature the flocs are described by two limiting cases, a solid impermeable sphere [7] or a uniform porous sphere [8]. Bagster and Tomi [7] calculated that for a homogeneous impermeable sphere the rupture occurs on a plane trough the center of the sphere while the critical shear rate does not depend on its size. In another simple model the aggregate has been considered as two rigid spheres [9]. Blaser calculated the break-up forces assuming that the flocs behave as solid ellipsoids [10, 11].

These theories were complemented by a vast amount of computer simulations studying different aspects of the aggregate behavior [12, 13, 14, 15]. Most of the simulations predict an aggregate densification with increasing shear flow. However, for strong shearing forces the simulations of Doi and Chen [15] showed a reduction of the coordination number and no densification.

Experimentally, the restructuring and break-up of aggregates was studied in [16, 17, 18, 19, 20, 21, 22]. Hoekstra and coworkers [16] investigated 2D systems with both a strongly attractive potential (rigid bonds between the particles) and a weakly attractive potential in which the particles can still slide over each other in an extensional flow. For both systems the shear flow causes anisotropy in the aggregate structure. To probe this anisotropy the Fourier transforms of the aggregate images were studied. The evolution of the coordination number as a function of the applied shear flow indicated a densification of the rigid flocs. Break-up was found to occur at the weakest link in the aggregate (at a single contact between the particles) and erosion was not observed. When surfactant was added to the system, no densification was seen. Hansen and coworkers [17] studied 2D colloidal aggregation in a Couette cell. The cluster size and structure was followed varying the shear rate. The weakly aggregated systems showed rearrangement into a more compact structure and a densification with increasing shear rate while the strongly aggregated systems did not display a significant change in structure. Stancik investigated the effect of shear [18] and elongational flow [19] on the structure of a monolayer of particles at a water/oil interface. The lattice structure was observed to pass from a hexagonal array through a liquid-like state, at start-up of the flow, to a semi-ordered state during steady flow. Aveyard [20, 21] also studied monolayers of particles at an interface when compressed in a Langmuir trough. At the water/air interface the particles were packed in a hexagonal array while at the water/oil interface they went through a transition from a hexagonal to a rhombohedral structure. The monolayer collapses by folding and corrugation when the surface pressure equals the interfacial tension, but the particles did not migrate from the interface under the compression. In the work of Yeung

and Pelton [22] a micro-mechanical technique was used to pull apart 3D single flocs. They showed that the floc strength does not depend on its size. The break up mechanism was dependent on the aggregate structure. A compact floc tended to break by surface erosion while more open flocs were broken into equal fragments. Blaser [10] considered flocs in shear and elongational flow. He found that in simple shear flow the flocs rotate as solid ellipsoids and were bent more than stretched. In contrary in elongational flow the flocs do not rotate and are aligned and stretched along the extensional axis.

In this paper we present experimental results for aggregate restructuring and break-up in simple shear flow and compare them with a simple model for solid body break-up. We investigate single 2D aggregates ranging in size between 20 and 400 particles, at relatively low shear rates using video microscopy. From the recorded microscopic images we extract the coordinates of the particles which are used to characterize the structural changes of the aggregate as a function of the applied shear rate. The critical shear rate for break-up is measured too. The aggregates all break at nearly the same shear rate independent of their size. The experimental findings are compared with a simple theoretical model. In this model a force balance between the external hydrodynamic forces due to the shear flow and the internal forces due to capillary interactions is formulated. From this balance the critical shear rate for break-up can be predicted. The aggregate can be considered as solid as long as no significant rearrangement of particles occurs. The capillary force stems from the deformation of the w/a interface around the particles. We consider the multiple particle capillary force as pair wise additive in agreement with our recent findings [23]. The external hydrodynamic force is assumed to be given by the drag force acting on every particle which for creeping flow is given by the Stokes formula. For simplicity it was assumed that the aggregate will break in two nearly equal parts.

The paper is organized as follows. In section 5.2 the experimental setup and procedures are presented. In section 5.3 the experimental results are discussed and compared with model calculations. The paper ends with some conclusions.

5.2 Materials and Methods

5.2.1 Materials

All experiments were conducted with spherical glass particles trapped at a liquid-air interface. The liquid phase was a mixture of water and glycerol (35 wt. % , Merck) with a density of 1090 kg/m^3, viscosity 2.34 mPas and surface tension of 71 mN/m. The glass particles (Polysciences Inc, with a radius $R_p = 115 \pm 10\,\mu$m, density 2480 kg/m^3) were small enough to be trapped at the water-air (w/a) interface. The contact angle of the particles at the w/a interface was determined to be $55^o \pm 2.5^o$.

5.2.2 Experimental Setup and Procedure

The experimental setup is illustrated in Figure 5.1. It consists of a Couette device with two concentric cylinders ($R_i = 24$ mm, $R_o = 45$ mm) that can be rotated in opposite directions. This creates a controlled shear flow, with a stagnant zone at a controllable radial position, in the gap between the cylinders when a liquid is inserted.

Thin stainless steel rings were attached to the cylinders to create a pinning edge for the liquid-air interface. The flatness of the interface was controlled by adding or removing liquid and measured from the refraction of a laser beam at the interface, as explained in

[23]. During the course of a single experiment water is slowly evaporating, causing the interface to curve slightly. However, this does not influence our experiments significantly. The interface is illuminated through the transparent bottom of the outer cylinder, while it is observed from above using a CCD camera equipped with a zoom lens. The camera was connected to an image acquisition system.

By adding particles to the w/a interface, an aggregate was formed spontaneously due to the strong capillary attraction between the particles. In principle it is possible to keep the aggregate in the stagnant zone and so in the field of view of the camera. However, the aggregate will stay on the same spot only if the total shear forces on all the particles cancel each other. When the aggregate rotates a little bit, due to the irregular shape of the aggregate, the shear forces change. Hence, in order to keep the aggregate at the same place, the rotational speed of the cylinders should be adjusted continuously, which in practice is not possible due to the relatively slow response of the flow field to the cylinder speeds. This was observed by other researchers [17], too. Instead the aggregate is allowed to rotate slowly in the Couette device. The CCD camera is kept stationary and the aggregate is recorded when it passes the field of view. The rotational speed of the cylinders is set to minimize the velocity of the aggregate.

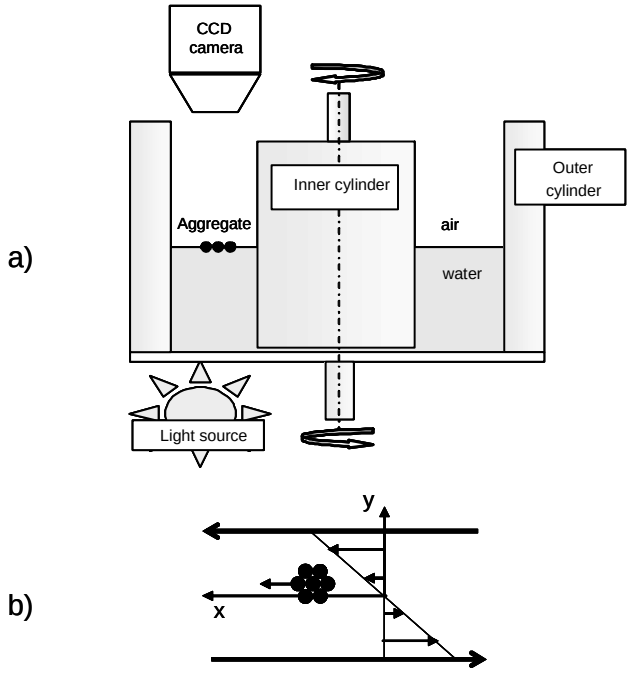

Figure 5.1: *a) The experimental set-up. b) The simple shear flow profile in the gap with the used coordinate system.*

Given the angular velocities of the two cylinders, the shear rate $\dot{\gamma}$ at a radial distance r can be calculated using [24]:

$$\dot{\gamma} = \frac{2R_i^2 R_o^2}{(R_o^2 - R_i^2)} (\omega_i - \omega_o) r^{-2}$$

where ω_i and ω_o are the angular velocities and R_i and R_o the radii of the inner and outer cylinder, respectively. A disadvantage of the wide gap geometry is the variation of the shear rate with distance r. For large aggregates the maximum relative variation of the shear rate inside an aggregate at the stagnant zone is given by:

$$\frac{\Delta\dot{\gamma}}{\dot{\gamma}} = \left|\frac{D}{\dot{\gamma}}\frac{d\dot{\gamma}}{dr}\right| = \frac{2D}{r_0}$$

where D is the diameter of the aggregate and r_0 the position of the stagnant zone. For a typical aggregate considered in this paper (2 mm diameter) the variation of the shear rate is about 10 % over the whole aggregate. The inertia of the aggregate can be neglected for the speeds applied.

The measuring protocol was as follows: after the formation of the aggregate it was sheared for 10 minutes at a fixed shear rate, starting at 0.1 s^{-1}, while images of the aggregate were captured. This time span was long enough to reach a steady state. After 10 minutes the shear rate was increased in steps of 0.10 s^{-1} and again kept constant during 10 minutes. The highest applied shear rate was 2.5 s^{-1}; enough to observe break-up of the aggregate.

5.2.3 Aggregate characterization

From the captured images the number and the coordinates of the particles inside the aggregate were determined using image processing software from Optimas. These coordinates were used for calculating several aggregate characteristics: aspect ratio, tilt angle with respect to the flow direction, coordination number, translational and orientational order. Below a short description of each of these characteristics is given.

⋆ Aspect ratio L/B: the aggregate shape was described as an ellipse with a semi-major axis L and a semiminor axis B. L/B has been calculated from the particle positions inside the aggregate [10, 25]:

$$\frac{L}{B} = \sqrt{\frac{\langle x^2\rangle + \langle y^2\rangle + \sqrt{\left(\langle x^2\rangle - \langle y^2\rangle\right)^2 + 4\langle xy\rangle^2}}{\langle x^2\rangle + \langle y^2\rangle - \sqrt{\left(\langle x^2\rangle - \langle y^2\rangle\right)^2 + 4\langle xy\rangle^2}}} \tag{5.1}$$

where $< x^2 >$, $< y^2 >$ and $< xy >$ are the second order central moments:

$$\langle x^2\rangle = \frac{1}{N}\sum_{i=1}^{N}\left(x_i - \langle x\rangle\right)^2 \qquad \langle y^2\rangle = \frac{1}{N}\sum_{i=1}^{N}\left(y_i - \langle y\rangle\right)^2$$

$$\langle xy\rangle = \frac{1}{N}\sum_{i=1}^{N}\left(x_i - \langle x\rangle\right)\left(y_i - \langle y\rangle\right)$$

N is the total number of particles in the aggregate and (x_i, y_i) the position of particle i inside the aggregate, while:

$$\langle x\rangle = \frac{1}{N}\sum_{i=1}^{N}x_i \qquad \text{and} \qquad \langle y\rangle = \frac{1}{N}\sum_{i=1}^{N}y_i$$

⋆ Tilt angle θ: the angle of the long axis of the aggregate with respect to the flow direction was calculated again using the second order moments [10, 25]:

$$\theta = \frac{1}{2}\tan^{-1}\left(\frac{2\langle xy\rangle}{\langle x^2\rangle - \langle y^2\rangle}\right) \tag{5.2}$$

By probing the tilt angle as a function of time, the rotation of the aggregate in the shear flow can be investigated.

⋆ The average coordination number Co is given by the average number of nearest neighbors per particle. A particle is considered a nearest neighbor when it is closer than first minimum in the pair correlation function $g(r)$ (in our case the first minimum is around 0.3 mm). A description of $g(r)$ is given in the next paragraph. The maximum average coordination number for an infinite 2D system is 6 (hexagonal close packing). For finite aggregates however the end effects will reduce the maximum attainable coordination number. In order to compensate for these effects in our aggregates, i.e. in order to be able to compare the coordination number of aggregates with different sizes, the measured coordination numbers were normalized on the theoretically calculated maximum coordination number for the same number of particles $Co_{\max}(N)$:

$$Co = 6\,\frac{Co_{\text{meas}}\,(N)}{Co_{\max}(N)} \tag{5.3}$$

$Co_{\max}(N)$ corresponds to a perfect hexagonal packing of disks with equal size. In Appendix 5A is explained how $Co_{\max}$ has been calculated.

⋆ For further characterization of the structure the pair correlation function, $g(r)$ was used. $g(r)$ is defined as [24, 26]:

$$g(r) = \frac{\langle n(r)\rangle}{n} \tag{5.4}$$

where $n(r)$ is the local density of particles at distance r from the reference particle and n is the average density of the aggregate (calculated as $n = N/(\pi LB)$). The pair correlation function $g(r)$ is usually used to characterize infinite areas covered with particles and do not extend into an empty area outside the aggregate. In these cases $g(r)$ will approach 1 for $r \to \infty$ values. In our case due to the finite aggregate size the $g(r)$ value will approach 0 for large r values. The finite size of our aggregates will also influence the magnitude of the peaks in $g(r)$. To minimize these finite size effects, only particles lying in a circle with radius $B/2$ from the center of the aggregate are considered in $g(r)$.

⋆ Another parameter to describe the structure inside the aggregate is the six fold symmetry complex order parameter ψ_6 [26]:

$$\psi_6^n = \frac{1}{z}\sum_{k=1}^{z}\exp(6i\phi_{nk})$$

where z is the number of nearest neighbors of particle n and ϕ_{nk} is the angle between the bond between particle n and k and the x-axis. ψ_6 is similar to the coordination number in that it is maximal (equal to 1) for perfect hexagonal packing. We need this parameter to calculate the orientational correlation function $g_6(r)$ which is given below. The orientational correlation function includes the information about the bond angles as calculated in ψ_6, but in addition it correlates the orientation of the crystal structure at

different positions inside the aggregate. It is maximal (equal to 1) when all the bonds are under 60^o or multiples of 60^o angles and the orientation of the crystal structure is everywhere the same:

$$g_6(r) = \frac{\left\langle \left(\psi_6^0\right)^* \psi_6 \right\rangle_{(r)}}{g(r)} \tag{5.5}$$

where ψ_6^0 is the parameter value of the central particle and the star denotes the complex conjugate. The averaging is done over all particles in a shell with a radius between r and $r + dr$ around the central particle. The function $g_6(r)$ was calculated as explained in the Appendix of [26] for all particles contained in the aggregate because, contrary to $g(r)$, $g_6(r)$ is not influenced by finite size effects.

⋆ Moreover, the Fourier transform of the 2D images was determined using the "ImageJ" software package. These Fourier images exhibit additional information on anisotropy and orientational order within the aggregates.

5.3 Results and Discussion

In this section the experimental results will be discussed. First the behavior of the aggregate will be described globally. Next, we look in more detail at the structure of the aggregate as a function of the rate of shear. Finally the experimental results for break-up will be compared with model calculations.

5.3.1 General Observations

Figure 5.2 reveals a sequence of images representing the general behavior of the aggregates at the applied shear rate. In Figure 5.2a the initial shape of an aggregate has been shown before starting the shear flow. This shape is preserved at low shear rates. With increasing shear rate the aggregate adopts a more circular shape and the ordering of the particles increases (Figure 5.2b and 5.2c). At a certain shear rate the hydrodynamic force starts to erode small parts and single particles from the rim of the aggregate (Figure 5.2d) and eventually at higher shear rates the aggregate will break-up (Figure 5.2e and 5.2f).

5.3.2 Structure Characterization

Below we present a more quantitative description of the structure of the aggregate as a function of the applied shear rate. We are interested in the evolution of the aggregate before break-up occurs. Thus the shear rates considered are less than 1.7 s^{-1}.

As explained in Section 5.2.3 the aspect ratio L/B is measure of the aggregate shape (for a circle $L/B = 1$). In Figure 5.3 the aspect ratio of several aggregates as calculated from the particle positions (x_i, y_i) using Eq. (5.1) has been shown as a function of the shear rate.

Initial ellipsoidal shapes gradually transform to a more circular shape whereas initial circular shapes stay circular. This is to be expected since the aggregate is rotating in the simple shear flow. Particles on the outside of the aggregate on the long, semimajor axis will experience the largest shear force and will be moved to sides of the aggregate which experience a lower shear force, i.e. the short, semiminor axis. The end result is a circular aggregate shape. In extensional flow other researchers found stretching of the

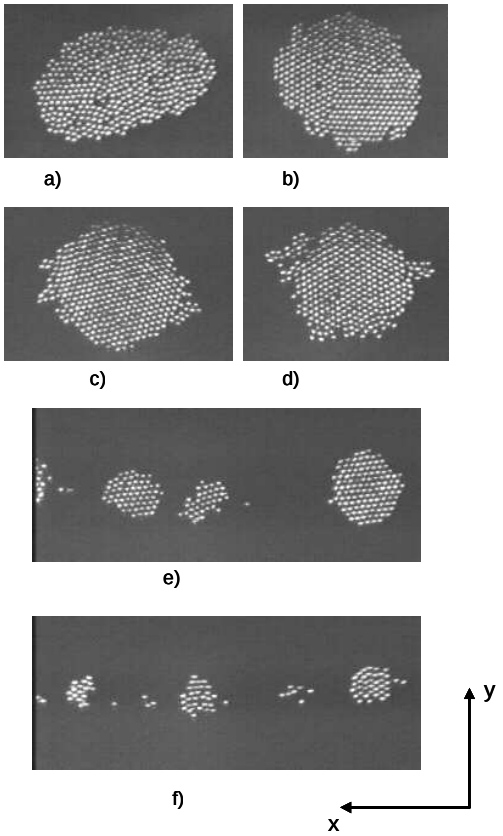

Figure 5.2: *Images of a typical aggregate at several successive shear rates- a)the initial state, b)* $\dot{\gamma} = 1.4\ s^{-1}$*, c)* $\dot{\gamma} = 1.7\ s^{-1}$*, d)* $\dot{\gamma} = 1.8\ s^{-1}$*, e)* $\dot{\gamma} = 1.9\ s^{-1}$ *and f)* $\dot{\gamma} = 2.0\ s^{-1}$ *(initially* $N = 409$*).*

aggregates [10, 16]. Thus the circular shape is characteristic for simple shear flow, in which the aggregate rotates.

The upper curve in Figure 5.3 suggest that for some cases a frictional yield force prevents the particles from sliding over each other at low shear rates.

In Figure 5.4 the average coordination number Co, calculated according Eq.(5.3) as explained Section 5.2.3, has been presented as a function of the applied shear rate. As one can see, the coordination number increases with increasing shear rate and comes close to 6, which corresponds to a hexagonal packing.

Why do the particles not immediately form a perfect hexagonal ($Co = 6$) circular ($L/B = 1$) aggregate at the initial stage? After all it is energetically the most favorable configuration. It is known that dense 2D systems tend to arrange into hexagonal order. If the particles would be able to slide along each other without any friction, it is expected that this perfect hexagonal structure would appear from the beginning. However, our aggregates at the initial stage, as are the aggregates at a specific shear rate, are stable. Our hypothesis is that there is some kind of friction force which prevents them from

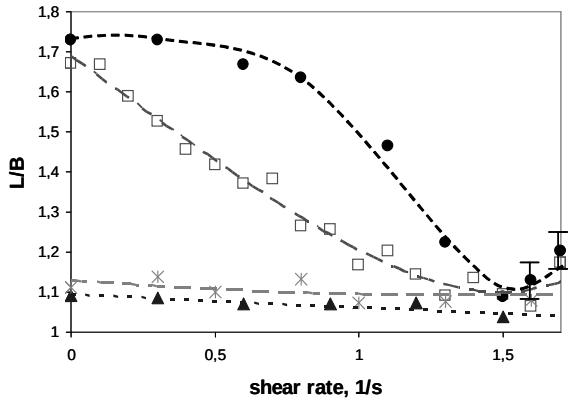

Figure 5.3: *The aspect ratio as a function of the applied shear rate. The measured values are given by the symbols, the lines are to guide the eye. The black circles correspond to* $N = 409$*, the squares to* $N = 189$*, the stars to* $N = 203$ *and the triangles to* $N = 285$*.*

further restructuring. This friction could be caused by the roughness of the particles. A particle cannot move if the sum of the external forces (capillary and drag force) is smaller than the static friction force. With increasing shear flow, more and more particles will experience external forces larger than the static friction force and will thus be able to slide along each other. Eventually, at sufficient shear rates, all particles will be able to slide and a perfect hexagonal aggregate will form. A similar increase in coordination number with increasing shear rate has been observed in [16].

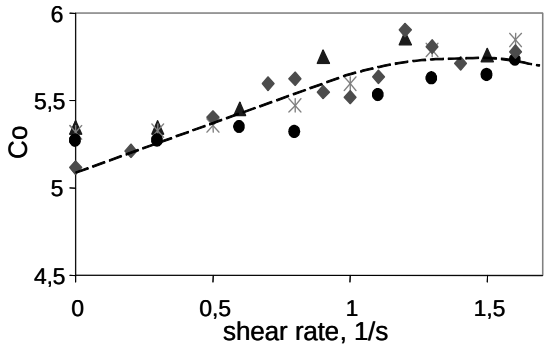

Figure 5.4: *The average coordination number as a function of the applied shear rate. The measured values are given by the symbols, the line is a guide to the eye. As before the black circles correspond to* $N = 409$*, the stars to* $N = 203$*, the triangles to* $N = 285$ *and the diamonds to* $N = 191$*.*

It is interesting to notice that there is a slight optimum in the coordination number around a shear rate of $\dot{\gamma} = 1.5\ \mathrm{s}^{-1}$. Similar effect is also observed in Figure 5.3 where there is a maximum in L/B again at $1.5\ \mathrm{s}^{-1}$. The critical shear rate for break-up is around 1.8

s^{-1}. Apparently, just before break-up of the aggregate, the shear forces become strong enough not only to overcome the barrier for sliding but also to break bonds between particles completely which leads to a deformation of the aggregate. The optimum in the curves in Figures 5.3 and 5.4 are a first indication of the onset for the break-up. The coordination number provides information only on the first shell of neighbor particles around the particle of interest. To investigate the presence of long range order the pair correlation function, $g(r)$ was calculated. $g(r)$ is defined as the probability of finding a particle at a position a distance r from another particle divided by the probability of finding a particle at that position irrespective of all other particle positions. So for $r \rightarrow \infty$, $g(r) \rightarrow 1$.

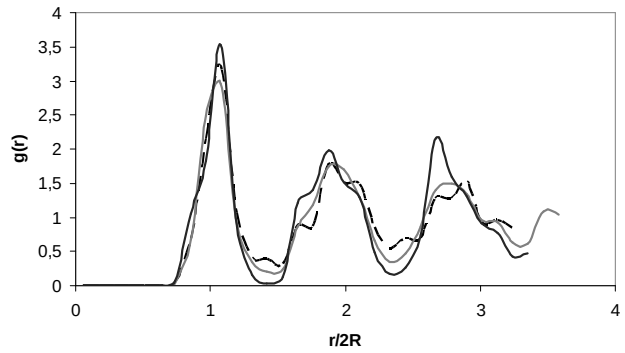

Figure 5.5: *Average $g(r)$ characteristic for different shear rates: the initial state (black dashed line), $\dot{\gamma} = 1.0 \pm 0.1\ s^{-1}$ (grey line) and $\dot{\gamma} = 1.5 \pm 0.2\ s^{-1}$ (solid line). The curves are averaged over 4 experiments with $N = 191$, 203, 285 and 409, respectively.*

Figure 5.5 shows $g(r)$ as determined using Eq.(5.4) for three stages: the initial, at 1.0 ± 0.1 s^{-1} and 1.5 ± 0.2 s^{-1}. The shown results have been obtained by averaging over four independent experiments. The oscillatory behavior that $g(r)$ show in our case implies that there is enhanced probability of finding particles at certain distances. The position of the 1st maximum in the figure indicates that the particles are nearly close packed. It is at about twice the particle radius. The order is preserved in the next shells too. However, there does not seem to be a significant difference in peak height at different shear rates. It can be seen though that the next peaks are getting more distinctive with increasing the shear rate hinting a small increase in the orientational order. As explained in Section 5.2 to prevent the end effects $g(r)$ was calculated only for the particles in the inner part of the aggregate. Thus we loose the long range order where more pronounced differences with the applied shear flow are expected.

Complementary to $g(r)$ the orientational correlation function $g_6(r)$ gives a quantitative measure of the orientational order of the system. Figure 5.6 shows $g_6(r)$, calculated using Eq.(5.5), as a function of the applied shear rate, for the same shear rates as given in Figure 5.5. Again, the results have been averaged over four experiments. There is a significant increase in the orientational order at larger distances for higher shear rates. The $g_6(r)$ of the initial aggregate shows a steep exponential decay while the decay becomes more moderate with increasing the applied shear flow. At the optimal shear rate (1.5 s^{-1}) the

decay line becomes almost horizontal showing once again that the shear flow forces the aggregates to a crystalline state.

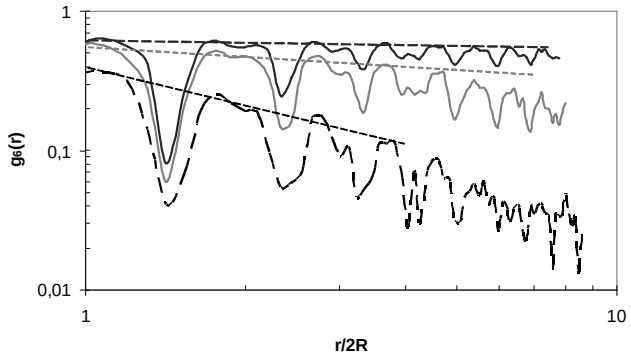

Figure 5.6: *Average $g_6(r)$ characteristic for different shear rates: the initial state (black dashed line), $\dot{\gamma} = 1.0 \pm 0.1\ s^{-1}$ (grey line) and $\dot{\gamma} = 1.5 \pm 0.2\ s^{-1}$ (solid line). The curves are an average from 4 experiments with $N = 191$, 203, 285 and 409, respectively. The straight dashed lines are drawn as a reference for the decay of the function.*

The change in the orientational order of the aggregates is also clearly seen in the Fourier transforms of the images shown in Figure 5.7. These Fourier images correspond to the aggregate configurations in Figures 5.2a, 5.2b and 5.2c, respectively. The Fourier image of the initial structure consist of a complete ring which indicates that the ordering of the particles is only local (Figure 5.7a) i.e. the aggregate has a 2D poly-crystalline structure. Applying a shear flow leads to a gradual better arrangement of the particles, and the ring gradually transforms to a series of bright spots. For 6-fold rotational symmetry (hexagonal structure) one expects 6 spots on the edges of a hexagon. Initially there are more than 6 spots, implying the presence of some domains with different orientation (Figure 5.7b). At higher shear rates the hexagon appears indicating that all the particles are oriented within the same domain (Figure 5.7c).Under influence of the shear flow the

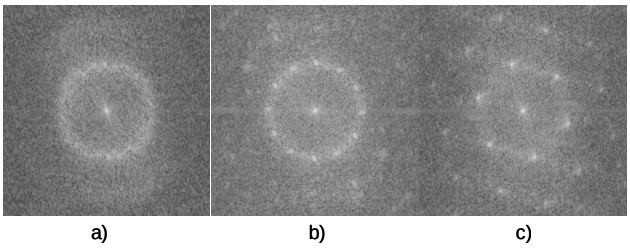

Figure 5.7: *Fourier transforms of aggregates for different shear rates: a) the initial state, b) $\dot{\gamma} = 1.4\ s^{-1}$, c) $\dot{\gamma} = 1.7\ s^{-1}$. $N = 409$.*

aggregate structure can be deformed. Fourier images are used to measure the anisotropy of the particle-particle distances inside the aggregate, as described in [18, 19]. Here we

consider as a measure of the anisotropy:

$$A = 1 - \lambda_- / \lambda_+$$

where λ_+ and λ_- are the shortest and longest reciprocal distance between neighboring particles in the aggregate. A will vary between 0 and 1; it is 0 for isotropic structures. In all cases the measured value for A is less than 0.15, while the experimental accuracy is also about 15%. Thus, within the accuracy of our method, all aggregates can be considered isotropic. In simple shear flow the circular aggregates are continuously rotating, thus the orientation of the compression and extensional axis with respect to the aggregate also varies in time. In contrast to experiments in elongation flow [16, 18, 19], this rotation enhances the isotropy inside the aggregates. This enhancement was also observed from the behavior of $g_6(r)$.

Stancik et al. [32] report Fourier images of 2D space filling structures. They observe a shear induced ordering and melting due to the sliding of particle lines along each other, caused by the boundaries of their equipment. In our case the whole aggregate can freely rotate resulting in a rotating hexagonal ordering in which the layers do not need to slide over each other. Hence in contrast to their observations we only a stationary (rotating) hexagonal structure in our Fourier images.

5.3.3 Solid body rotation

In the model for aggregate break-up presented later in section 5.3.5, the aggregate will be considered as solid disk. To check whether this assumption is valid, we measured the orientation angle of the aggregates as a function of time and compared it with the expression for solid body rotation of an ellipse in a simple shear flow [10, 24]:

$$\tan\theta = \frac{L}{B} \tan\left(\frac{2\pi\,(t - t_0)}{T}\right) \tag{5.6}$$

Here t is the time, t_0 the reference time and T the period of rotation. L/B can be compared with the measured from the experiments according to Eq. 5.6. Consequently, T can be compared with the theoretical prediction [24]:

$$T = \frac{2\pi}{\dot\gamma}\left(\frac{L}{B} + \frac{B}{L}\right) \tag{5.7}$$

In Figure 5.8 the angle θ and the aspect ratio L/B have been plotted as a function of the dimensionless time $\dot\gamma t$ for two different shear rates. The points represent the experiments. The experimentally obtained aspect ratio is independent of the orientation θ: $L/B = 1.3 \pm 0.1$. The measured period for rotation T scales with the inverse of $\dot\gamma$: $\dot\gamma T = 11.8 \pm 0.2$. The values for $\theta(\dot\gamma t)$ have been compared with the theoretical prediction, Eq.(5.6), given by the curved line in Figure 5.8. The values for L/B and T in Eq.(5.6) were used as fitting parameters: $L/B = 1.6$ and $\dot\gamma T = 11.84$, which is in fair agreement with the measured values. As one can see the rotation of the aggregate agrees well with a solid body rotation. Thus, the assumption, made in the modeling in section 5.3.5, that the aggregate behaves as solid body is justified for our experimental conditions.

5.3.4 Critical Shear rate for Break-up

The most interesting characteristic of an aggregate in shear flow is the critical shear rate at which the aggregate will break in relation to its size. We use the number of particles inside

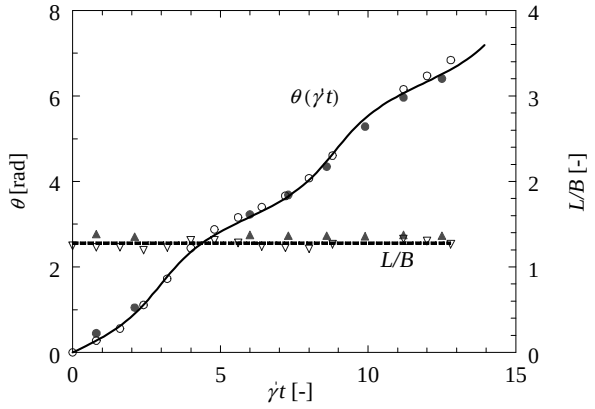

Figure 5.8: *Rotation and elongation of an aggregate for two different shear rates (*1.3 s^{-1}*, solid symbols, and* 1.6 s^{-1}*, open symbols): the bullets represent* $\theta(\dot{\gamma}t)$ *while the triangles give* L/B*. The symbols are the experimentally obtained data and the solid line is given by Eq.* (5.6)*. The experimental data scale correctly with* $\dot{\gamma}t$*.*

an aggregate as a measure of its size. Neglecting the initial erosion of some particles, we define the critical shear rate as the shear rate at which the aggregate reduces significantly its size, by breaking-up in two or more nearly equal sized fragments.

In Figure 5.9 the number of particles has been plotted as function of the shear rate. As one can see from the figure the larger aggregates ($N = 200 \div 400$) break all near the same critical shear rate independent of their size; $\dot{\gamma}_{\text{crit}} \approx 1.8 \pm 0.2$ s^{-1}. For small aggregates ($N < 50$) a broader range of critical shear rates has been observed: $\dot{\gamma}_{\text{crit}}$ ranges from 1.5 to 2.0 s^{-1}. For small aggregates the internal stresses near the center of the aggregate are rather low so it is possible to form also more open aggregates which are easier to break. For the larger aggregates, due to the relatively long range of the particle-particle interaction, the internal stresses near the center of the aggregate are relatively high, the particles are pushed closer together and the initial structure is always more close packed.

5.3.5 Modelling the critical shear rate

In this section a simple model is proposed to calculate the critical shear rate for aggregate break-up as a function of the number of particles inside the aggregate. In this model we focus on the normal capillary forces between the particles, because possible lateral sliding forces will scale with these attractive forces. The hydrodynamic force driving the break-up is the strongest when the elongation is perpendicular to the line of rupture.

Moreover the crystalline defect lines present at the initial stages have already disappeared during the restructuring at the lower shear rates before break-up occurs. Without defect lines, also the lateral displacement of the two halves asks first an initial separation of the individual particles on each side of the line of rupture. In that case also lateral break-up will occur at higher critical shear rates. This is in line with observations by Patina et al.[30, 31] Their results showed a strong tangential force between the particles

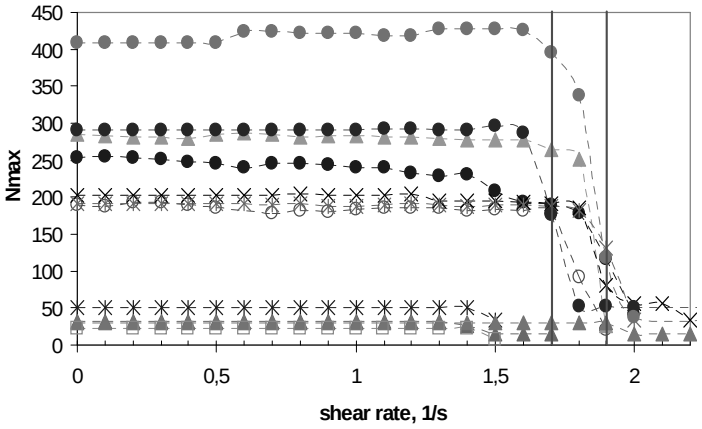

Figure 5.9: *Number of particles in an aggregate as a function of the shear rate.*

that they explained from surface roughness.

For our modelling we consider an aggregate with a circular shape and a hexagonal packing of the particles. We assume that the aggregate will break in the middle into two equal parts. Moreover we suppose that before break-up occurs, the particles inside the aggregate will not rearrange, thus the aggregate is considered as a solid body.

In Figure 5.10 the initial configuration has been given. The aggregate is divided into two equal parts (A and B) and it is subjected to a simple shear flow. The center of resistance of the aggregate is positioned at the origin of the flow field. Due to the shear flow the aggregate will rotate and, depending on the momentary orientation, the parts A and B are alternatively pushed together or pulled from each other by the flow.

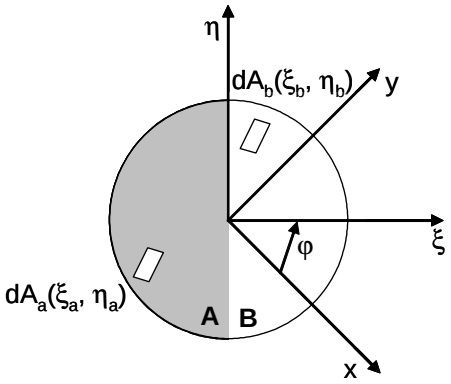

Figure 5.10: *Schematic representation of the aggregate and the coordinate systems used in the calculations.*

At rest all the particles in part A exert a force on all the particles in B, due to capillary interactions. The net capillary force between A and B is balanced by a normal force which acts on the contact line between A and B. In the elongational phase of the shear flow the flow field tries to separate part A from B, reducing the normal force between them. At a certain flow strength, the critical shear rate, this normal force becomes zero and the capillary force is completely balanced by the hydrodynamic force. A slight increase of the shear rate will result in separation of the two parts from each other. We will consider this critical shear rate, neglecting the dynamics of the cyclic compression and stretching and considering only the elongational component of the flow field.

Hence, to predict when break-up will occur, both of the capillary and hydrodynamic forces have to be calculated. The capillary force between A and B can be calculated by summing the particle-particle interactions between all particles in A with all particles in B. In the "Linear Superposition Approximation" (LSA) [27] the capillary force between particle a and b is given by:

$$F_{lsa}^{[a,b]} = 2\pi\sigma q Q^2 K_1(qr_{ab})$$

where $K_1(x)$ is the modified Bessel function of first order and r_{ab} is the distance between particles a and b. The coefficient Q is defined as: $Q = r_{cl}\sin\psi$ where r_{cl} is the radius of the three phase contact line around the particle and ψ is the angle between the liquid interface and the horizontal plane near the particles. The inverse capillary length is given by $q = (g\Delta\rho/\sigma)^{1/2}$ where g is the acceleration due to gravity, $\Delta\rho$ is the density difference between the lower and upper liquid and σ is the surface tension. In [23] we showed that the LSA expression is valid also for short distances between the particles and in the LSA the multiparticle interactions are just pair-wise additive. Using the above arguments the capillary force dF_c between a small area element dA_a located at (ξ_a, η_a) and an area element dA_b located at (ξ_b, η_b) (see Figure 5.10) is given by:

$$dF^{[c]} = 2\pi\sigma q Q^2 K_1(qr_{ab})\, n^2 dA_a dA_b \tag{5.8}$$

where $r_{ab} = [(\xi_b - \xi_a)^2 + (\eta_b - \eta_a)^2]^{1/2}$ is the distance between dA_a and dA_b. The number of particles per unit area n is given by $n = 1/A_{\text{spec}}$, where A_{spec} is the specific area of one particle in hexagonal packing: $A_{\text{spec}} = 2\sqrt{3}R_p^2$.

Here we consider only elements which are at least $2R_p$ apart ($r_{ab} \geq 2R_p$). To sum the interactions of every element dA_a in A, with every element dA_b in B, we have to integrate over the areas of both A and B. For the components of the force dF_c in the ξ- and η-direction we have:

$$F_{\xi}^{[c]} = C_1 \int_{A_b}\int_{A_a} K_1(qr_{ab})\cos\phi_{ab} dA_a dA_b$$

$$F_{\eta}^{[c]} = C_1 \int_{A_b}\int_{A_a} K_1(qr_{ab})\sin\phi_{ab} dA_a dA_b$$

where $C_1 = 2\pi\sigma q Q^2 n^2$ is a constant and ϕ_{ab} is the angle of the vector connecting both areas with the ξ-axis:

$$\tan\phi_{ab} = \frac{\eta_b - \eta_a}{\xi_b - \xi_a} \tag{5.9}$$

Due to symmetry arguments $F_{\eta}^{[c]}$, will be zero in our case.

We assume that the hydrodynamic force on parts A and B of the aggregate can be calculated as the sum of the drag force on the separate particles. For Stokes flow this drag force is given by:

$$\underline{\mathrm{F}}_d = 6\pi\mu R_p f_d \underline{\mathrm{V}} \tag{5.10}$$

where μ is the liquid viscosity and f_d is a friction coefficient to account for the partial immersion of the particle and the hydrodynamic screening of the other particles in the aggregate. $\underline{\mathrm{V}}$ is the local undisturbed flow velocity.

In simple shear flow the velocity is given by: $\underline{\mathrm{V}} = \dot{\gamma} y \underline{\mathrm{e}}_x$. This flow can be decomposed into a straining flow and a rotation [24]:

$$\underline{\mathrm{V}} = \tfrac{1}{2}\dot{\gamma}\left(y\underline{\mathrm{e}}_x + x\underline{\mathrm{e}}_y\right) + \tfrac{1}{2}\dot{\gamma}\left(y\underline{\mathrm{e}}_x - x\underline{\mathrm{e}}_y\right) \tag{5.11}$$

Since the aggregate can follow the rotation, this component of the flow does not exert any force on the aggregate. Eventual break up of the aggregate stems from the straining flow field. Therefore we only consider this component in the calculations (the first term on the right hand side). Because the force should be calculated in the body fixed (ξ, η) coordinate system, the (x, y) components of this straining field are expressed in the (ξ, η) components:

$$V_\xi = \tfrac{1}{2}\dot{\gamma}\left(\xi \sin 2\varphi + \eta \cos 2\varphi\right)$$
$$V_\eta = \tfrac{1}{2}\dot{\gamma}\left(\xi \cos 2\varphi - \eta \sin 2\varphi\right)$$

where φ is the angle between the ξ and the x direction.

To get the total drag force acting on part A we again integrate over the area of A:

$$F_\xi^{[d]} = C_2 \int_{A_a} V_\xi dA_a \tag{5.12}$$

$$F_\eta^{[d]} = C_2 \int_{A_a} V_\eta dA_a \tag{5.13}$$

where $C_2 = 3R_p f_d n$ is a constant. Due to symmetry the total drag force on part B, should be equal but opposite to that on part A.

The extensional drag force is maximum for $\varphi = 45^o$. In this case the line of fracture coincides with the compressional axis. Both $F_{c,\eta}$ and $F_{d,\eta}$ are zero in this case and we can express the critical shear rate as:

$$\dot{\gamma}_{\mathrm{crit}} = \frac{2C_1}{C_2} \frac{\int_{A_b}\int_{A_a} K_1\left(q r_{ab}\right)\cos\theta_{ab} dA_a dA_b}{\int_{A_a} \xi dA_a} \tag{5.14}$$

The integral expression for the critical shear rate, Eq. (5.14), has been evaluated numerically, where $\dot{\gamma}_{\mathrm{crit}}$ was expressed as a function of N, i.e. the number of particles inside the aggregate; N is related to the radius of the aggregate R_{agg} (assuming close hexagonal packing) by:

$$N = \frac{\pi R_{\mathrm{agg}}^2}{A_{\mathrm{spec}}}$$

For comparison of the model with the experimental data, we plot in Figure 5.11 the critical number N_c as a function of the shear rate $\dot{\gamma}$ instead of plotting $\dot{\gamma}_{\mathrm{crit}}$ as a function of N (as it was in Figure 5.9). The calculations (represented by the curves) have been compared with the experimentally obtained critical sizes (the symbols). As

one can observe, the calculated critical size is almost independent of the shear rate, which qualitatively matches the experimental results. This result is consistent with model calculations performed by Bagster and Tomi [7] which show that both the tensile and shear stresses are independent of the aggregate size.

The drag coefficient f_d was used as free parameter in the calculations. By matching the theory with the experimental data one obtains $f_d = 0.24 \pm 0.2$. Based on literature data [28] f_d of a half immersed single sphere at a w/a interface is about 0.5. In the present model the hydrodynamic drag force is assumed to act equally on all particles which overestimate the drag force [12]. In fact the outer particles of an aggregate shield the inner particles from the flow. Thus the drag coefficient is expected to be different for different particles depending on their position inside of the aggregate. This last consideration can be taken into account by assuming an average value for f_d. The outer particles will have the highest f_d ($f_d \approx 0.5$) while for the inner particles f_d is less than 0.5. Thus, we can match the critical shear rate of our model to the experimentally determined critical shear rate by assuming an average $< f_d > = 0.24 \pm 0.2$.

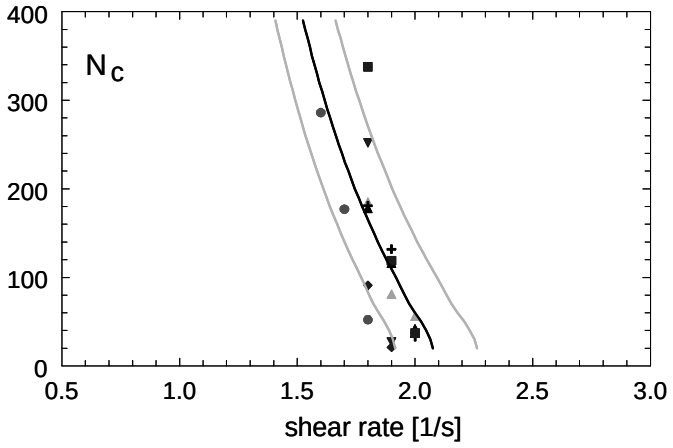

Figure 5.11: *Critical number of particles inside the aggregate versus shear rate as calculated from the theory for* $f_d = 0.24$ *(the black line) compared with the experimentally found critical shear rates (the symbols). The grey line on the right represents the calculations for* $f_d = 0.22$ *and the one on the left for* $f_d = 0.26$*, indicating the sensitivity of the critical shear rate on the value of* f_d*.*

It has been reported before that a pure extensional flow is more efficient in breaking up aggregates than a simple shear flow [24, 29]. In simple shear flow the efficiency of break-up is lowered by the rotation of the aggregates. Due to this rotation each part of the aggregate is exposed to the extensional flow only for a short time and then has time to recover (to attract again). This slows down the process of break-up and possibly also affects the critical shear rate itself.

Secondly, the particles can also rearrange. This reduces the effective shear rate as experienced by the aggregate. In other words: particles moving with the flow experience a smaller drag force than particles which are kept on the same position, which is the case for solid body approximation. The experimental data for the coordination number show

a decrease in order for shear rates higher than 1.5 s^{-1}; this supports the statement that particles indeed start to rearrange inside the aggregate.

Moreover, due to the small gap between the separating parts there is also a hydrodynamic drag force to overcome which was not taken into account. However, because the aggregate floats on the liquid/air interface, no pressure can built up in the gap between the separating parts; consequently this hydrodynamic drag force will be small.

All these effects are assumed to have only a small influence on the critical shear rate and have been absorbed in the fitting parameter f_d.

Although we studied the behavior of compact 2D aggregates, we think this is also useful for understanding the break-up behavior of more open 3D aggregates because, in contrast with dense 3D aggregates which are impermeable for the shear flow, all the particles in a 2D structure feel the surrounding flow directly due to the planar structure of these aggregates and as such it is comparable with permeable 3D structures.

5.4 Conclusions

The behavior of an aggregate in shear flow is a complex phenomenon. Only a few number of models exists that describe the behavior of a 2D aggregate in shear flow and even fewer experimental results are available. We are the first to investigate the behavior of aggregates in a simple shear flow for a wide range of aggregate sizes.

It was found that with increasing shear rate the aggregates become more circular, ordered and dense. The order parameters $g(r)$ and $g_6(r)$ show an increasing translational and orientational long range order with increasing shear rate. This effect can also be observed directly from the Fourier images. However, just before breaking (1.5 s^{-1}) a small increase in disorder was found. Opposite to pure elongational flow here no large anisotropy was shown before break-up.

Analysis of the rotational motion of some non-circular aggregates reveals a variation in rotational speed and a period of rotation which are consistent with a solid body rotation.

The aggregates break-up at roughly the same critical shear rate: 1.8 ± 0.2 s^{-1}. A simple model was developed to explain the experimental results. The aggregate was modeled as a solid body that eventually will break in two nearly equal pieces. The capillary and drag force on the two pieces were calculated and from their ratio the critical shear rate was found. In accordance to experimental observations, the theoretical model shows that the size dependence of the critical shear rate is weak. This is also consistent with the model developed by Bagster and Tomi [7]. Our model predicts the critical shear rate correctly if one assumes an average value $< f_d >$ of 0.24. This is in line with the expectation that the drag force on particles near the center of the aggregate is screened by the presence of the outer particles, reducing the average value of f_d, compared to a single partially immersed particle.

Acknowledgments. This work has been supported by the Foundation for Fundamental research on Matter (FOM), which is financially supported by the Netherlands Organization for Scientific Research (NWO).

Appendix 5A. Calculation of $Co_{max}(N)$

To calculate the optimum coordination number for an aggregate of finite size we consider a hexagonal aggregate with k particles in each of the 6 edge rows. Such a hexagon

contains in total $N^{(k)} = 3k\,(k-1)+1$ particles. The largest hexagon inside this hexagon, in which all particles have 6 nearest neighbors, contains $(k-1)$ particles in the edge rows and counts $N^{(k-1)}$ particles. Moreover there are 6 vertex particles having 3 nearest neighbors and another $6\,(k-2)$ edge row particles having 4 nearest neighbors. (The total number of particles correctly sums up to: $N^{(k-1)} + 6 + 6\,(k-2) = N^{(k)}$.) The total sum of nearest neighbors $S_{nn}^{(k)}$ becomes:

$$\begin{aligned} S_{nn}^{(k)} &= N^{(k-1)} \times 6 + 6 \times 3 + 6\,(k-2) \times 4 \\ &= 6\,\left(3k^2 - 5k + 2\right) \\ &= 6\,\left(N^{(k)} - \sqrt{1 + \frac{4}{3}\left(N^{(k)} - 1\right)}\right) \end{aligned}$$

The average coordination number, which we identify with $Co_{\max}(N)$, is just the ratio between this sum and the total number of particles inside the hexagon:

$$Co_{\max} = \frac{S_{nn}^{(k)}}{N^{(k)}} = 6\,\left(1 - \frac{1}{N}\sqrt{1 + \frac{4}{3}\,(N-1)}\right)$$

In Figure 5.12 the result for $Co_{\max}(N)$ versus the number of the particles is presented. As expected for large N, $Co_{\max}(N)$ will approach 6 and it is less for small numbers of particles where the edge effects have a larger influence.

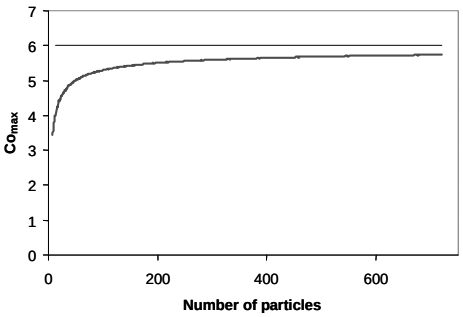

Figure 5.12: *The calculated maximum coordination number for hexagonal packed particles as a function of the number of particles.*

References

[1] Vermant J. *Curr. Opin. Colloid Interface Sci.* **2001**, 6, 489.

[2] Tadros, Th. F. *Solid-liquid dispersion*, Academic press, 1987.

[3] B.A. Wills, *Mineral processing technology (Int. Ser. Material Sci. Technology, vol 41),* Pergamon press, Oxford 1988.

[4] Elimelech M., Gregory J., Jia X., Williams R.A. *Particle deposition and Aggregation*, Butterworth-Heinemann, Woburn, 1998.

[5] Lu S.,Ding Y.,Guo J. *Adv. Coll. Int. Sci* **1998**, 78,197.
[6] Jarvis P., Jefferson B., Gregory J., Parsons S.A. *Water Research* **2005**, 39, 3121.
[7] Bagster D. F., Tomi D., *Chem. Eng. Sci.* **1974**, 29, 1773.
[8] Adler P. M., Mills P. M. *J. of Rheol.* **1979**, 23, 25.
[9] Nir A., Acrivos A. *J. of Fluid Mech.* **1973**, 59, 209.
[10] Blaser S. *J. of Colloid Interface Sci.* **2000**,225, 273.
[11] Blaser S. *Chem. Engin. Sci.* **2002**, 57, 515.
[12] Higshitani Ko, Iimura K., *J. of Colloid Interface Sci.* **1998**, 204, 320.
[13] Bossis G., Brady J. F. *J. Chem Phys.* **1984,** 80, 5141.
[14] Potanin A. *J. of Colloid Interface Sci.* **1993**, 157, 399.
[15] Chen D., Doi, M. *J. of Colloid Interface Sci.* **1999**, 212, 286.
[16] Hoekstra H., Vermant J., Mewis J. *Langmuir* **2003**, 19, 9134.
[17] Hansen P. H., Malmsten M., Bergenstahl B., Bergstrom L. *J. of Colloid Interface Sci.* **1999**, 220, 269.
[18] Stancik E. J., Gavranovich G. T., Widebrant M. J. O., Laschitsch A. T., Vermant J., Fuller G. G. *Faraday Discuss.* **2003**, 123, 145
[19] Stancik E.J, Widenbrant J.O., Laschitsch A.T., Vermant J.. Fuller G. *Langmuir* **2002**, 18 , 4372.
[20] Aveyard R., Clint J. H., Nees D., Paunov V. N. *Langmuir* **2000**, 16, 1969.
[21] Aveyard R., Clint J. H., Nees D., Quirke N. *Langmuir* **2000**, 16, 8820.
[22] Yeung A. K. C., Pelton R. *J. of Colloid Interface Sci.* **1996**, 184, 579.
[23] Vassileva, N. D.; van den Ende, D.; Mugele, F.; Mellema, J. *Langmuir* **2005**, 21, 11190.
[24] Van de Ven, T. G. M. *Colloidal hydrodynamics*, Academic Press: London, **1989**.
[25] Teague M. R. *J. Opt.Soc.Am.* **1980**, 70, 920.
[26] Gray J. J., Klein D. H., Korhel B. A., Bonnecaze R. T., *Langmuir* **2001**, 17, 2317.
[27] Kralchevsky, P.A.; Nagayama, K. *Adv. Colloid Interface Sci.* **2000**, 85, 145.
[28] Petkov, J.T.; Denkov, N.D; Danov, K.D.; Velev, O.D.; Aust, R., Durst, F. *J. Colloid Interface Sci.* **1995**, 172, 147.
[29] Kao S., Mason S. G., *Nature* **1975**, 253, 619.
[30] Pantina J.P., Furst E.M.; *Phys. Rev. Lett.* **2005**, 94 (13): 138301.
[31] Pantina J.P., Furst E.M.; *Langmuir* **2004**, 20, 3940-3946.
[32] Stancik E.J., Hawkinson A.L., Vermant J., Fuller G.G.; *J. of Rheol.* **2004**, 48, 159-173.

Chapter 6

Fragmentation and erosion of two-dimensional aggregates in shear flow

Abstract

We consider single two-dimensional aggregates, containing glass particles trapped at a water/oil or water/air interface. Two modes for aggregate break-up are investigated: break-up by fragmentation into a few parts and break-up by erosion of single particles. We have studied the critical shear rate for these modes as a function of the aggregate size. Two different particle sizes were used. The smaller particles, with a radius of 65μm, form aggregates which break-up predominantly by erosion at a shear rate between 0.5 and 0.7 s^{-1}, which value hardly depends on the size of the aggregates, while the larger particles, with a radius of 115 μm, form aggregates that break by erosion or by fragmentation. Again in both modes the critical shear rate depends only weakly on the size of the aggregates and ranges between 1.6 and 2.2 s^{-1}. Also the structural changes inside the aggregate before break-up were studied. The aggregate behavior at the water/air and water/oil interfaces is quite similar. The critical shear rate for break-up was also modeled. The model shows in both modes a weak dependence of the critical shear rate on the aggregate size, which is consistent with the experimental observations. The kinetics of the erosion process was modeled, too and compared with the experimentally obtained time dependence of the aggregate size.

The differences for the large and small particle systems can be attributed to the occurrence of friction forces between the particles, which one expects to be much larger for the large particle system, due to the stronger two particle interaction.

6.1 Introduction

The behavior of aggregates is an important issue in liquid suspension processes. For example in waste water treatment one needs an efficient method for the removal of particles [1, 2, 3, 4]. Larger particles are easier to remove, thus it is convenient to work with aggregates of particles. Also smaller flocs will settle down slower and will be captured less efficiently by air bubbles. Small flocs can also block the membranes during filtration. These processes are designed to minimize the breaking of flocs, but still the flocs can be

subjected to high shear rates (e.g. close to a mixing impeller or during the transfer from one tank to another) where the flocs have to resist to the corresponding stresses [4]. Thus it is important to study aggregate behavior when subjected to flow in order to design efficient methods for their treatment.

Detailed knowledge of how 3D aggregates will break is still missing. This is due to the complexity of the system and the involved processes: many body interactions, irregular shapes and influence of contamination. Moreover, not all forces acting in these processes are clear [4]. The logical way to investigate such a complicated system is to start with the simpler 2D case. The main advantage of 2D experiments is the absence of gravitational settling of the aggregates, which makes the visualization much easier. The theoretical modeling in 2D is also simpler. However, even for 2D systems there is little information available on the break up mechanisms for different conditions.

Floc break-up has been classified in two general modes [4, 5]. The first one is the removal of single particles or small aggregates from the parent aggregate, called surface erosion. In the second mode the flocs break-up into pieces with similar sizes, called fragmentation. The resulting size distribution after rupture can inform us whether erosion or fragmentation has occurred. Erosion produces fragments with much smaller size than the original aggregate thus the particle size distribution is roughly bimodal [6]. The main qualitative difference between erosion and fragmentation is the energy input which is low for erosion and high for fragmentation. The time scales of the two processes are also different. Fragmentation occurs immediately after applying of the critical stress while the erosion occurs over much longer time scales [4]. For 3D systems there are indications that the two modes are driven by different stresses. Erosion is caused by shear in tangential direction and fragmentation by a tensile stress acting normally across the floc [7, 8, 9].

There is no unique way to determine the floc strength because the flocs can be very different in size, shape and properties. It is also difficult to compare the results from different studies because the results depend strongly on the used technique for measuring the aggregate strength. Most researchers investigate the dependence of the floc size as a function of the applied hydrodynamic shear flow. For a review of the techniques used we refer to Jarvis and coworkers [3]. The simplest way of evaluating the floc strength is to measure the ratio between the floc size before and after break-up for a particular shear rate. The floc strength can be related to the energy dissipation of the system or the velocity gradient applied to the system. This technique relays upon complex theories and floc break-up models. Recently developed techniques directly measure the floc rupture [10, 11, 12]. Pantina and Fust [10] investigated the bending of bonded colloidal particles using optical tweezers. The results show the existence of strong tangential forces between the particles which they explain with a surface roughness. Yeung and Pelton [11] use micromechanical techniques to pull apart flocs. They found that break-up occurs at the weakest spot inside the aggregate. This explains why a compact aggregate will break due to erosion. According to their results the aggregate strength did not depend on the aggregate size.

In 2D most of the research has been concentrated on the investigation of particle monolayers at a liquid interface [13, 14, 15, 16]. Aggregates in 2D were investigated by Hoekstra [17] and Hansen [18]. Hoekstra and coworkers [17] studied two types of 2D suspensions with particles sliding over each other or not depending on the attraction potential between the particles. They found that shear flow induces the same type of anisotropy in both systems. In the system with a strong attractive potential the density inside the aggregates increases with the applied shear flow while it decreases in systems

with a weak attraction between the particles. Break-up was found to occur at the weakest link in the aggregate (at a single contact point between the particles) and erosion was not observed. Hansen and coworkers [18] studied 2D colloidal aggregation in a Couette cell. The development of the cluster size and structure was followed at different shear rates. The weakly aggregated systems showed rearrangement into a more compact structure and a densification with increasing shear rate while the strongly aggregated systems did not display a significant change in structure.

Analytical models can be used to describe the aggregate break-up. These models generally oversimplify the aggregate structure. The two limiting cases are a uniform impermeable [19] or permeable [20] sphere. The model developed by Sontag and Russel [21] considers also an nonhomogeneous aggregate structure.

The fracture of the aggregate is assumed to occur along planar surfaces (usually passing through the aggregate center) [19, 22] or by crack growth [23]. The several models for break-up predict a different dependence on the volume fraction and the radius of the primary particles.

Only a few studies dealing with erosion have been carried out [4, 24, 25]. Powell and Mason [24] described the erosion kinetics for compact spherical aggregates without attraction between the primary (cohesionless) particles. They found that the erosion rate depends on the flow type and the ratio between the aggregate and primary particle size, but it was independent of the shear rate.

It is quite complicated to model the transient response of an aggregate to a change in flow pattern, analytically [26, 27]. The easiest way to address this transient response is to use a simulation. A promising simulation model is based on the discrete element method (DEM) [28, 29]. Currently the limitation of DEM is that it does not take into account the exact local flow field. A more advanced version of DEM attempts to model the hydrodynamic contributions to the drag force [30], however it is a rough approximation because it adjusts the flow based only on the local porosity of the aggregate.

In our previous study [31] (see chapter 5) we presented experimental results for the break-up of aggregates of glass particles at the water/air interface. An advantage of our experimental method is that it is direct and nondestructive. We observe with video microcopy single aggregates, which give us a detailed look into the processes of breaking. In addition, the reverse process of aggregation after collision with another aggregate is suppressed, which also simplifies the modeling. However the method has certain drawbacks, too. First, like every method looking at single particle level, it is difficult to get enough data for statistically significant results. Second, it was not possible to keep the aggregates in the field of view and thus the exact moment of aggregate break-up is seldom seen. To be able to collect statistically reliable data we work with aggregates consisting of sub-millimeter non-colloidal particles which will give a similar initial structure for all experiments. Using non-colloidal particles has the advantage that we have a well defined attraction force because the capillary force is significantly larger than the other forces.

Our results showed that the aggregates break at nearly the same shear rate independent of their size. The evolution of the aggregate before break-up was also investigated. With increasing shear rate the aggregates adopt a more circular shape and the particles order in a denser hexagonal structure. A simple theoretical model was developed to explain the experimental data. In this model it was assumed that the aggregate is a circular disk which will break exactly along a center line into two equal pieces. The capillary and drag forces acting on both parts of the aggregate were calculated and from their ratio the critical shear rate was found. The model shows a weak size dependence of the critical

shear rate for break-up which is in agreement with the experimental observations.

Here we continue the investigation of the aggregate break-up, expanding the studied systems to two different interfaces (water/air and water/oil) and two particle sizes (R_p = 115 μm and 64 μm). Moreover, special attention has been paid to the possible modes of the break-up process. We are interested in how and where the aggregates will break. The aggregate structure before break-up was also investigated and compared for the different systems. The modeling has been developed further by including the determination of the critical shear rate for erosion and the kinetics of the erosion process.

The structure of the present chapter is as follows. In section 6.2 the forces acting between the particles are discussed and moreover, single particle erosion is modeled. In section 6.3 we present and discuss our experimental results. The chapter ends with a summary of our findings.

6.2 Theory

6.2.1 Interaction forces

For colloidal 2D systems interaction forces include capillary, Van der Waals, electrostatic, excluded volume repulsion and electric-field-induced capillary [32] (electrodipping) forces.

Due to the size of the primary particles the capillary interaction in our system is so strong that all other interaction forces, except the excluded volume repulsion, can be neglected. As we have shown in Chapter 4 [33] in the "Linear Superposition Approximation" (LSA) the capillary force between particle a and b is given by:

$$F_{lsa}^{[a,b]} = 2\pi\sigma q Q^2 K_1(qr_{ab}) \tag{6.1}$$

where $K_1(x)$ is the modified Bessel function of first order and r_{ab} is the distance between particles a and b. The coefficient Q is defined as: $Q = r_{cl}\sin\psi$ where r_{cl} is the radius of the three phase contact line around the particle and ψ is the angle between the liquid interface and the horizontal plane near the particles. The inverse capillary length is given by $q = (g\Delta\rho/\sigma)^{1/2}$ where g is the acceleration due to gravity, $\Delta\rho$ is the density difference between the lower and upper liquid and σ is the surface tension. In [33] we showed that the LSA expression is valid also at short distances between the particles and in the LSA the multiparticle interactions are just pair-wise additive. In Figure 6.1 the capillary force between two particles has been plotted for all investigated systems.

The only tangential interaction force arrises from the friction between two touching particles. This friction can be dynamic (sliding) or static (sticking). The distinction is important, because the dynamic friction can be significantly smaller than the static friction. The friction force between two surfaces is considered to be proportional to the normal force with which the surfaces are pushed together. In the inner regions of an aggregate the normal forces are larger than in the outer regions, due to the long range tail of the two particle interaction, and hence also the friction forces are larger in the inner regions.

6.2.2 Flow field

A particle moving in a liquid experiences a drag force. A particle moving in an interface between two liquids experiences a drag force due to the presence of the two liquids and

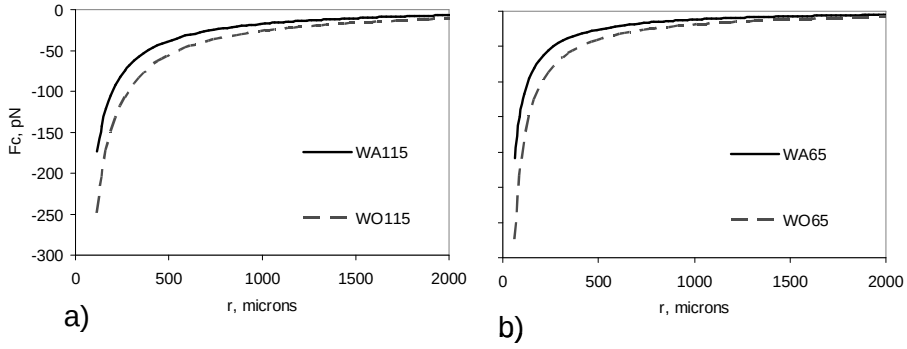

Figure 6.1: *Calculated capillary forces. Panel a) shows the calculations for the particles with R_p= 115 μm and panel b) shows the force for R_p= 65 μm. The solid lines correspond to water/air interface and the dashed to water/oil.*

the interface itself. Hence we modify this drag force by introducing an additional f_d coefficient: $\underline{\mathrm{F}}_d = 6\pi\mu R_p f_d \underline{\mathrm{V}}$.

The nature of the flow also influences the fragmentation process. In simple shear flow significantly higher shear rates are required for break-up, compared to extensional flow [34]. In general the less vorticity there is in a flow, the more efficient is the break-up [35]. On the other hand, simple shear flow can be more efficient than extensional flow if rupture is occurring along crack line. Due to the rotational motion of the aggregates the crack line will pass through certain orientations that are favorable for aggregate break-up [36].

The flow field around a particle in an aggregate is disturbed by its neighboring particles. This hydrodynamic contribution can give rise both to normal and tangential forces on the particles. In a system with just two particles it leads to an effective repulsive force between approaching particles and can prevent them from aggregating. Most analytical theories either do not take the hydrodynamic contribution into account, by assuming a completely porous aggregate, or approximating the aggregate as very dense and impermeable, in which case the external flow does not penetrate at all inside the aggregate. In our 2D system there is a more or less free flow above and below the particles and in first approximation the hydrodynamic force on an individual particle can be modeled as a simple Stokes law as for isolated particles.

The influence of the Brownian motion can be neglected in our non-colloidal system. Moreover, inertia forces have been calculated to be significantly smaller than the interaction and drag forces.

6.2.3 Critical shear rate in the erosion model

The critical shear rate for erosion can be calculated using the formalism explained in Chapter 5 [31] with some small adjustments. We consider a disk shaped aggregate with a single particle on its the rim as illustrated in Figure 6.2.

To predict when break-up will occur in this case, again both of the capillary and hydrodynamic forces have to be calculated. The capillary force between the aggregate A

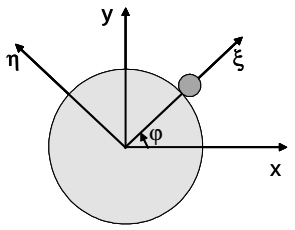

Figure 6.2: *The scheme used for modelling erosion of single particle.*

and the particle b can be calculated by summing the particle-particle interactions between all particles in A with particles b. Using expression 6.1 for the particle interaction, the capillary force dF_c between a small area element dA_a located at $(r\cos\phi, r\sin\phi)$ and particle b located at $(R_{\rm agg}+R_p, 0)$ is given by:

$$dF^{[c]} = 2\pi\sigma q Q^2 K_1\left(qr_{ab}\right) n dA_a \tag{6.2}$$

where $r_{ab} = [(R_{\rm agg}+R_p-r\cos\phi)^2 + (r\sin\phi)^2]^{1/2}$ is the distance between dA_a and the particle. The number of particles per unit area n is given by $n = 1/A_{\rm spec}$, where $A_{\rm spec}$ is the specific area of one particle in hexagonal packing: $A_{\rm spec} = 2\sqrt{3}R_p^2$.

To sum the interactions of every element dA_a in A, with the particle b, we have to integrate over the area of the aggregate A. For the components of the force dF_c in the ξ- and η-direction we have:

$$F_\xi^{[c]} = C_1 \int_0^{2\pi}\int_0^R K_1(qr_{ab})\cos\phi\, r dr d\phi$$

$$F_\eta^{[c]} = C_1 \int_0^{2\pi}\int_0^R K_1(qr_{ab})\sin\phi\, r dr d\phi$$

where $C_1 = 2\pi\sigma q Q^2 n$ is a constant. Due to symmetry arguments $F_\eta^{[c]}$, will be zero in our case.

We assume that the hydrodynamic force on aggregate A and particle b can be calculated as the sum of the drag force on the separate particles. For Stokes flow this drag force is given by:

$$\underline{\mathrm{F}}_d = 6\pi\mu R_p f_d \underline{\mathrm{V}} \tag{6.3}$$

where μ is the liquid viscosity and f_d is a friction coefficient to account for the partial immersion of the particle and the hydrodynamic screening of the other particles in the aggregate. $\underline{\mathrm{V}}$ is the local undisturbed flow velocity.

In simple shear flow the velocity is given by: $\underline{\mathrm{V}} = \dot\gamma y \underline{\mathrm{e}}_x$. This flow can be decomposed into a straining flow and a rotation [35]:

$$\underline{\mathrm{V}} = \tfrac{1}{2}\dot\gamma\left(y\underline{\mathrm{e}}_x + x\underline{\mathrm{e}}_y\right) + \tfrac{1}{2}\dot\gamma\left(y\underline{\mathrm{e}}_x - x\underline{\mathrm{e}}_y\right) \tag{6.4}$$

Since the aggregate can follow the rotation, this component of the flow does not exert any force on the aggregate. Eventual break up of the aggregate stems from the straining flow field. Therefore we only consider this component in the calculations (the first term on the right hand side). Because the force should be calculated in the body fixed (ξ,η)

coordinate system, the (x, y) components of this straining field are expressed in the (ξ, η) components:

$$V_\xi = \tfrac{1}{2}\dot{\gamma}\,(\xi \sin 2\varphi + \eta \cos 2\varphi)$$
$$V_\eta = \tfrac{1}{2}\dot{\gamma}\,(\xi \cos 2\varphi - \eta \sin 2\varphi)$$

where φ is the angle between the ξ and the x direction.

The total drag force acting on particle b is given by:

$$F_\xi^{[d]} = 6\pi\mu R_p f_d V_\xi \tag{6.5}$$

$$F_\eta^{[d]} = 6\pi\mu R_p f_d V_\eta \tag{6.6}$$

The total drag force on part A, should be equal but opposite to that on particle b. The extensional drag force is maximum for $\varphi = 45^o$. In this case the line of fracture coincides with the compressional axis. Both $F_{c,\eta}$ and $F_{d,\eta}$ are zero in this case and we can express the critical shear rate from the force balance

$$3\pi\mu R_p f_d \dot{\gamma}_{\rm crit}\,(R_{\rm agg} + R_p) = C_1 \int_0^{2\pi}\int_0^R K_1(qr_{ab})\cos\phi\, r dr d\phi$$

as:

$$\dot{\gamma}_{\rm crit} = \frac{\sigma q Q^2}{3\sqrt{3} f_d \mu R_p^3} \frac{\int_0^{2\pi}\int_0^R K_1(qr_{ab})\cos\phi\, r dr d\phi}{(R_{\rm agg} + R_p)} \tag{6.7}$$

The integral expression for the critical shear rate, Eq. (6.7), has been evaluated numerically, where $\dot{\gamma}_{\rm crit}$ was expressed as a function of N, i.e. the number of particles inside the aggregate; N is related to the radius of the aggregate $R_{\rm agg}$ (assuming close hexagonal packing) by:

$$N = \frac{\pi R_{\rm agg}^2}{A_{\rm spec}}$$

The critical shear rate for erosion assuming $f_d = 1$ has been calculated for the 2 different systems studied here: small and large particles. The viscosity and interfacial tension values are taken for the water/air interface. The results are presented in Figure 6.3. As one can see the small particles aggregate will erode at much lower shear rate than the large particle aggregates. The dependence of the critical shear rate on the size of the aggregate is very small, especially for the small particles system. For comparison the critical shear for breaking in two halves is also presented in the figure. Surprisingly, the critical shear rate for breaking by erosion and fragmentation are very close to each other. Hence, one can expected the aggregates to break by both mechanisms. One has to keep in mind that we only have an order of magnitude guess for the value of f_d. For $f_d \neq 1$ we can read the vertical axis in Figure 6.3 as $f_d\dot{\gamma}_{\rm crit}$ to obtain the dependence of $\dot{\gamma}_{\rm crit}$ on f_d. Additionally, the value of f_d could be different for the water-oil and water-air interface.

6.2.4 Modeling the erosion kinetics

We are also interested in the number of particles dN inside an aggregate that escape from the aggregate during dt or, equivalently, the time rate of change of the aggregate radius $R_{\rm agg}$:

$$\frac{dN}{dt} = \frac{d}{dt}\frac{\pi R_{\rm agg}^2}{2\sqrt{3}R_p^2} = \frac{\pi R_{\rm agg}}{\sqrt{3}R_p^2}\frac{dR_{\rm agg}}{dt} \tag{6.8}$$

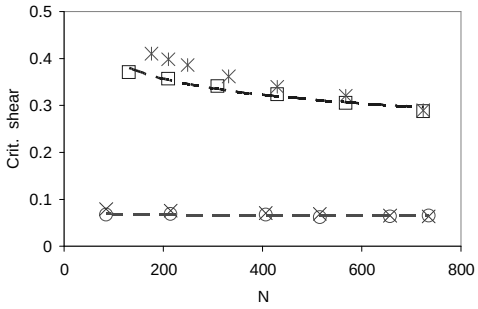

Figure 6.3: *Calculated critical shear rate for erosion of single particle for WA115 (with open squares) and WA65 systems (with open circles). The lines are fit, according to Eq.(6.10). With crosses and stars symbols are presented also the critical shear rate for rupture of the aggregate in two equal pieces. The calculations are made assuming* $f_d = 1$.

To simplify the argument we assume that the average escape rate Y for a single particle will be given by:

$$Y = c_1 \left(F_{\rm hydr} - F_{\rm attr}\right)_{\rm max}$$

where c_1 is a constant. The total escape rate dN/dt should be proportional to the number of particles at the rim of the aggregate: $N_{edge} = \pi R_{\rm agg}/R_p$:

$$\frac{dN}{dt} = -\frac{\pi R_{\rm agg}}{R_p} Y = -c_1 \frac{\pi R_{\rm agg}}{R_p} \left(F_{\rm hydr} - F_{\rm attr}\right)_{\rm max} \tag{6.9}$$

In the preceding section we calculated the critical shear rate for break-up. From that we can express the maximal attraction force as:

$$F_{\rm attr} = C_1 \int_0^{2\pi} \int_0^R K_1(q r_{ab}) \cos\phi \, r dr d\phi = 3\pi\mu f_b \left(R_{\rm agg} + R_p\right) R_p \dot{\gamma}_{\rm crit}$$

while the maximal hydrodynamic force has been given by:

$$F_{\rm hydr} = 3\pi\mu f_b \left(R_{\rm agg} + R_p\right) R_p \dot{\gamma}$$

So Eq. (6.9) can be written as:

$$\frac{dN}{dt} = -3c_1\pi^2 \mu f_b R_{\rm agg} \left(R_{\rm agg} + R_p\right) \left(\dot{\gamma} - \dot{\gamma}_{\rm crit}\right)$$

Combining this with Eq. (6.8) gives:

$$\frac{dR_{\rm agg}}{dt} = -A \left(R_{\rm agg} + R_p\right) \left(\dot{\gamma} - \dot{\gamma}_{\rm crit}\right)$$

with $A = 3\sqrt{3} c_1 \pi \mu f_b R_p^2$ a dimensionless constant. If $\dot{\gamma}_{\rm crit} = {\rm const}$, the general solution of this equation is given by:

$$R_{\rm agg}(t) = R_0 \exp(-A \left(\dot{\gamma} - \dot{\gamma}_{\rm crit}\right) t)$$

with R_0 the radius of the aggregate at $t = 0$ when the shear rate was set to $\dot{\gamma}$. The influence of R_p has been neglected in this solution because the assumption that A is constant is only valid for large aggregates: $R_{\rm agg}/R_p >> 1$.

However, $\dot{\gamma}_{\rm crit}$ does depend on the size and we describe this dependence as:

$$\frac{\dot{\gamma}_{\rm crit}}{\dot{\gamma}_c} = \left(\frac{N}{N_c}\right)^{-1/k} = \left(\frac{R_{\rm agg}}{R_c}\right)^{-2/k} \tag{6.10}$$

which is a good representation of the observed size dependence. The differential equation which one has to solve, becomes:

$$\frac{d}{dt}\left(\frac{R_{\rm agg}}{R_c}\right) = -A\left(\frac{R_{\rm agg}}{R_c} + \frac{R_p}{R_c}\right)\left(\dot{\gamma} - \dot{\gamma}_c\left(\frac{R_{\rm agg}}{R_c}\right)^{-2/k}\right)$$

The steady state solution of this differential equation is given by:

$$\dot{\gamma} - \dot{\gamma}_c\left(\frac{R_{\rm agg}}{R_c}\right)^{-2/k} = 0$$

or

$$R_\infty = R_c\left(\frac{\dot{\gamma}}{\dot{\gamma}_c}\right)^{-k/2}$$

with R_∞ the radius of the aggregate for $t \to \infty$. This could also be concluded directly from Eq.(6.10). Assuming $R_p << R_{\rm agg}$ one obtains for the differential equation:

$$\int_{X_0}^{X(t)} \frac{dX}{X\left(X^{-2/k} - [X_\infty]^{-2/k}\right)} = A\dot{\gamma}t$$

where $X = R_{\rm agg}/R_c$ and $X_\infty = R_\infty/R_c$. Introducing $\xi = X/X_\infty$ the integral reduces to:

$$A\dot{\gamma}t = \int_{\xi(t)}^{\xi_0} \frac{d\xi}{\xi\left(1 - \xi^{-2/k}\right)}$$

which is a standard integral:

$$\int \frac{dx}{x\left(1 - x^{-m}\right)} = \frac{1}{m}\ln\left(x^m - 1\right)$$

Substitution of $m = 2/k$ results in:

$$A\dot{\gamma}t = \frac{k}{2}\ln\left(\frac{\xi_0^{2/k} - 1}{\xi^{2/k}(t) - 1}\right)$$

This relation can be inverted to:

$$\xi(t) = \left[1 + \left(\xi_0^{2/k} - 1\right)\exp\left(-\tfrac{2}{k}A\dot{\gamma}t\right)\right]^{k/2}$$

where $\xi = R_{\rm agg}/R_\infty = (N/N_\infty)^{1/2}$. Hence one eventually obtains for the aggregate size as a function of time:

$$R_{\rm agg}(t) = \left[R_\infty^{2/k} + \left(R_0^{2/k} - R_\infty^{2/k}\right)\exp\left(-\left(2A\dot{\gamma}/k\right)t\right)\right]^{k/2}$$

where R_0 is the size at $t = 0$. The number of particles inside the aggregate as a function of time is given by:

$$N(t) = \left[N_\infty^{1/k} + \left(N_0^{1/k} - N_\infty^{1/k}\right) \exp\left(-\left(2A\dot{\gamma}/k\right) t\right)\right]^k \tag{6.11}$$

Several approximations have been made in the last two sections which limit the applicability or accuracy of this simple model. Below those assumptions are summarized:

- The dependence of the critical shear rate on the aggregate radius is calculated by approximating the aggregate by a disc with constant particle density. This approximation is only valid for large aggregates; at small aggregates the discrete particle-particle interactions will become important.
- We use a power law for the dependence of the critical shear rate on the aggregate radius.
- We assumed that the erosion rate is proportional to the difference $(F_{hydr} - F_{attr})$.
- We assume single particle erosion. Multiple particle erosion might result into and increased erosion rate.

6.3 Experimental

6.3.1 Materials and Methods

Materials

All measurements were conducted with spherical glass particles trapped at a liquid-fluid interface. As lower liquid phase was used a mixture of water with glycerol (35 wt. % , Merck). As upper phase was used pentadecane (Merck) or air. In this way two kinds of interfaces were created: a water/air and a water/oil interface. Moreover, two sizes of glass particles were used: $R_p = 115\ \mu m$ and $R_p = 65\ \mu m$ (Polysciences Inc, density 2480 kg/m^3). The glass particles were small enough to be trapped at the water/air interface. The system properties are summarized in Table 6.1. The lower phase has a viscosity of 2.34 $mPas$ and a density 1090 kg/m^3. Pentadecane has a viscosity of 2.34 $mPas$, too and a density 773 kg/m^3. For all systems the particles were submerged mostly in the lower phase. Images of the particles positioned at the interface are shown in Figure 6.4 and the measured contact angles α_c are included in Table 6.1.

System	Lower phase	Upper phase	γ, mN/m	$R_p, \mu m$	α_c°
WA115	Water+Gly	Air	71	115±10	55°±2.5
WO115	Water+Gly	PD	44	115±10	54°±3
WA65	Water+Gly	Air	71	65±10	41°±5
WO65	Water+Gly	PD	44	65±10	43°±5

Table 6.1: *System properties; Gly: Glycerol, PD: Pentadecane.*

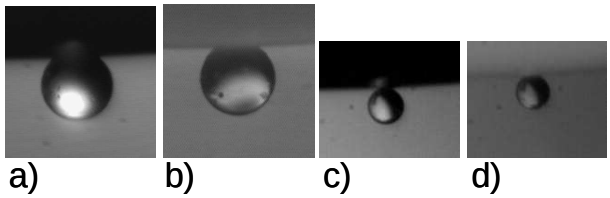

Figure 6.4: *Images of single particle positioned at the interface: a) WA115, b) WO115, c) WA65 and d) WO65.*

Experimental Setup and Procedure

The experimental setup as it was illustrated in Figure 5.1 of Chapter 5 consists of a Couette device with two concentric cylinders ($R_i = 24$ mm, $R_o = 45$ mm) that can be rotated in opposite directions. This creates a controlled shear flow in the liquid confined by the gap between the cylinders, with a stagnant zone at a controllable radial position. Thin stainless steel rings were attached to the cylinders to create an edge at which the liquid-air interface is pinned. The flatness of the interface is controlled by adding or removing liquid to or from the lower phase and it is measured from the refraction of a laser beam at the interface, as explained in Chapter 2.

The glass particles were added to the w/a interface. They aggregated fast due to the strong capillary attraction between them. In this way the initial aggregate was created. For the w/o experiments additionally the oil phase is poured on the top of the water layer. It was checked that adding the oil phase does not change the pinning of the three phase contact line, keeping the liquid-liquid interface flat.

The liquid interface is illuminated through the transparent bottom of the outer cylinder, while it is observed from above using a CCD camera equipped with a zoom lens. The camera was connected to an image acquisition system. In principle it is possible to keep the aggregate in the stagnant zone and thus in the field of view of the camera. However, the aggregate will stay on the same spot only if the total shear forces on all particles cancel each other. When the aggregate rotates a little bit, due to the irregular shape of the aggregate, the shear forces change. Hence, in order to keep the aggregate at the same place, the rotational speed of the cylinders should be adjusted continuously using a feedback loop, which in practice is not possible due to the relatively slow response of the flow field to the cylinder speed adjustments, see Chapter 2. This was observed by other researchers [18], too. Instead the aggregate is allowed to rotate slowly in the Couette device. The CCD camera is kept stationary and the aggregate is recorded when it passes the field of view. The rotational speeds of the cylinders are set to minimize the velocity of the aggregate.

The protocol for measuring the restructuring and eventual break-up of an aggregate was as follows: After the formation of the aggregate it was sheared for 10 minutes at fixed shear rate, starting at 0.1 s^{-1}, while images of the aggregate were captured. This time span was long enough to reach a steady state. After 10 minutes the shear rate was increased in steps of 0.10 s^{-1} and again kept constant during 10 minutes. The highest applied shear rate was 2.5 s^{-1} enough to observe break-up of the aggregate.

Aggregate Characterization

The most relevant properties of the aggregate are internal structure, size, and shape. As characteristic of the aggregate size we use the number of particles, for the shape the aspect ratio L/B and for the structure the coordination number Co as well as the Fourier transforms of the images. All those characteristics were extracted from the captured images using the image processing software tools Optimas and ImageJ. The way to determine them has been explained in detail in Section (5.2.3), see also ref [32].

Reproducibility

In general the behavior of all aggregates from the four systems considered was qualitatively the same. It should be noted however that for the same system, identical experiments sometimes produce different results. Considerable effort has been put into controlling the experimental conditions. Before each experiment the whole set-up was rigorously cleaned to prevent contamination by previous experiments. Also the liquid-particle systems were allowed to equilibrate before the experiments start as well as after a change in the shear rate. Both these reproducibility enhancing measures make a single experiment very time consuming. Hence, this set-up and procedure are not suitable for obtaining statistical information based on a very large number of experiments.

There are two main arguments that can explain the observed reproducibility problems. First, the bad reproducibility could be related to the structure (dislocation density, order, porosity, shape) of the aggregate at the beginning of an experiment. The initial structure of the aggregate can influence its behavior throughout the whole experiment. Each aggregate is unique and hence the differences between the experiments would have a statistical origin.

Second, the bad reproducibility could be caused by uncontrolled experimental conditions. Contamination of the phases can be excluded due to the rigorous cleaning procedures. However, during the preparation of the experiment, dust from the ambient air can pollute the interface. These dust particles are difficult to observe since they usually are smaller than the particles. When there is dust present between the particles it could change the aggregate behavior.

Another uncontrolled parameter is the ambient temperature, which directly influences the viscosity and the interfacial tension. However, it is expected that the temperature does not have a large influence on the qualitative behavior of the aggregate; it will mainly influence the value (and accuracy) of the measured critical shear rate.

6.3.2 Results and Discussion

As mentioned in the introduction we are interested in the structural changes and break-up mechanisms of aggregates subjected to a simple shear flow. Four different systems were considered while the shear rate was varied between 0.1 and 2.5 s^{-1}. The obtained results will be presented in the following order: First, we will consider the general aggregate behavior and the differences between the four systems will be discussed. Next, a detailed view will be taken at the occurring break-up mechanisms. At last the model for erosion kinetics, as discussed in the theoretical section, will be compared with the experimental results.

General aggregate behavior

In Figure 6.5 representative images of the aggregate behavior are shown at different shear rates for the four investigated systems. As one can see for all systems in the initial stage the particles form compact, dense aggregates. With increasing shear rate the aggregates become more circular, stay dense or become denser and the crystalline ordering increases. At a certain shear rate, which corresponds to the critical shear rate, the aggregate size is reduced significantly. The last image in panel a (large particles system) shows clearly breaking by fragmentation, while in panel d (smaller particles) the result of the erosion process is clearly visible.

Below we will consider separately the changes that the shear flow induces in aggregate size, shape and structure, one by one.

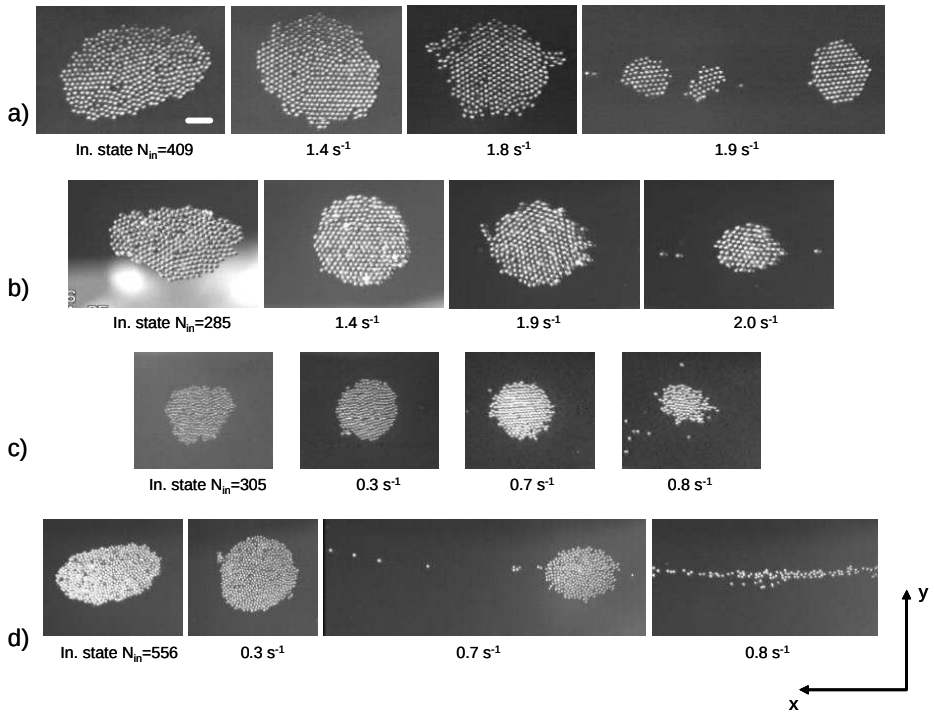

Figure 6.5: *Images of the four investigated system at different shear rates: a) WA115, b) WO115, c) WA65 and d) WO65. The flow is along x-direction. The white bar corresponds to 1 mm.*

Size The size of the aggregate is given by the number of particles. Representative experiments on the evolution of the aggregate size as a function of the shear rate are shown in Figure 6.6. As one can observe the size stays more or less constant until the critical shear rate is reached. In the next figure (Figure 6.7) the critical shear rate for all experiments has been summarized. Because of the spread in the experimental data it is difficult to say how the critical shear rate exactly depends on the aggregate size. However, it seems that the dependence is very weak. Because the data spread it is also

difficult to distinguish between the models for break-up by fragmentation and break-up by erosion. The lines in the figure represent the calculations of the critical shear rate in case of erosion according to Eq.(6.7). For the fitting parameter f_d the optimum was found at $f_d = 0.19$ for the Wx115 and $f_d = 0.11$ for the Wx65 system, which is lower than expected (for half immersed spheres at w/a interface one can expect $f_d = 0.5$). As was discussed in [31] and chapter 5, a smaller f_d value corresponds to a higher critical shear rate, which in the case we consider (a single particle at the rim) can be explained by the hydrodynamic coupling between the particle and its neighbors and internal particles rearrangements. The difference in the received f_d values between the large and small particle systems will be discussed later in the present section.

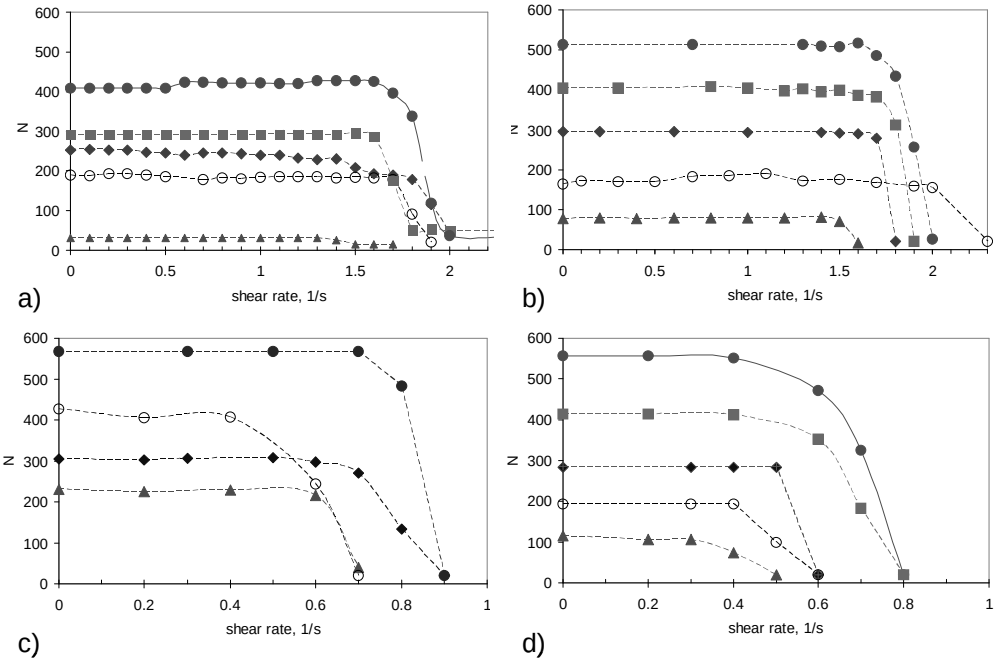

Figure 6.6: *The evolution of the number of particles as a function of the shear rate for the four experimental systems: a) WA115, b) WO115, c) WA65 and d) WO65.*

The critical shear rate is similar for aggregates at w/a and w/o interface. It can be explained by looking at the capillary forces, which are quite similar in both cases. Since the measured contact angles of the particles in both systems are very similar (see Table 6.1) the magnitude of the capillary force is also similar. For distance $r = 2R_p$ it was calculated that $F_{cap}^{(WA115)} = -174\ pN$, $F_{cap}^{(WO115)} = -248\ pN$ and $F_{cap}^{(WA65)} = -8\ pN$, $F_{cap}^{(WO65)} = -13\ pN$. In addition, for both systems the particles were for the largest part submerged into the water phase (Figure 6.4), hence it can be expected that covering them with oil will not change a lot of their properties.

Shape In Figure 6.8 it is shown that the aspect ratio decreases (i.e. circularity increases) with increasing shear rate for all systems. Such increase of the circularity is characteristic

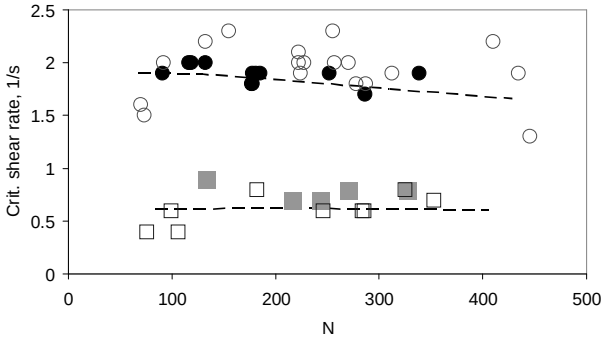

Figure 6.7: *Critical shear rate versus number of particles for the different systems. With solid circles are the results for WA115, with open circles-WO115, with solid squares-WA65 and with open squares- WO65. The lines are fits according to the model in section 6.2.3 with* $f_d = 0.19$ *for Wx115 and* $f_d = 0.11$ *for Wx65 system.*

for simple shear flow; it has not been observed in other types of flow such as extensional flow. We attribute this to the rotation of the aggregates. If the aggregates adjust themselves too slowly to the continuously changing (rotating) deformational component of flow, circular symmetry is promoted. When the shear rate approaches the critical shear rate, there is a tendency towards larger aspect ratio's, as the onset to break-up.

Structure The structure of an aggregate is directly related to the strength of the aggregate. Its development will be characterized by the changes in the coordination number Co, and in the Fourier transforms of the images. It was also observed that an amorphous layer in the aggregate was formed. In Figure 6.9 Co is presented as a function of the applied shear rate. There is a pronounced difference in the initial state between the systems with small and with large particles. In the initial state Co is significantly larger for the WX65 systems than for the WX115 systems. With the applied flow the coordination number for WX65 systems is constant within the measurement accuracy (Figure 6.9c) or even decreases (Figure 6.9d) while for WX115 it increases (Figure 6.9a and b).

Similar differences in the coordination number as a function of the applied shear rate were received by Hoekstra and coworkers [17] for 2D suspensions. They observed for a system with a stronger attraction potential (a surfactant free system) an increase of the coordination number with increasing shear rate while a system with a weaker attraction potential (with surfactant) showed the opposite behavior i.e. a decrease of the coordination number with increasing shear rate. The two systems have a different bonding strength between the particles, in the first one the bonds are rigid and the particles can not slide easy over each other, while in the second system the bonds are weaker and the particles can slide over each other.

The results for L/B and Co show that the initial effect of the shear rate is to order and increase the circularity of the aggregates. It was also noticed that for many experiments a small decrease not only of the circularity but also of the coordination number was observed just before breaking (Figure 6.8 and Figure 6.9). This is again an indication that the aggregate structure starts to break down under the applied shear flow. Because the

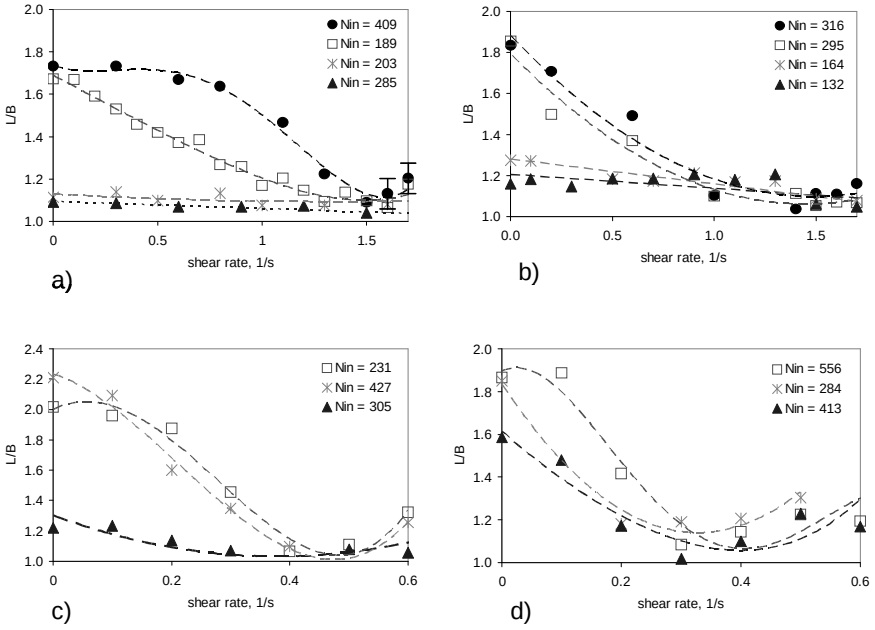

Figure 6.8: *Typical aspect ratio L/B at different shear rates for the four different systems: a) WA115, b) WO115, c) WA65 and d) WO65. In the legends of the graphs are shown the initial number of particles for the particular aggregate. The measured values are given by the symbols, the lines are guide to the eye.*

WO65 system shows this decrease from the beginning it means that the flow destabilizes the aggregate at all shear rates.

The *Co* results indicate that all aggregates already had, or developed a crystalline structure. The large aggregate systems preferably develop a single crystal structure (with 3 exceptions), identified by the points in the 2D Fourier transform (Figure 6.10). The Fourier images of the small particle systems (1 exception) showed the development of circular bands instead of points with increasing shear rate (Figure 6.11). The combination of a high coordination number with a band structure in the Fourier images points towards the existence of multiple crystal domains with different orientations in the small particle system. The exceptions observed we explain with a difference in the initial aggregate structure due to the statistical nature of the aggregation.

In Chapter 5 [31] we argued that the WA115 aggregates behave as solid disc-like bodies. Compared to the motion of the aggregate as a whole, there occurs hardly any restructuring and movement of separate particles inside the aggregate. This behavior is observed for the WO115 system, too, while WX65 aggregates become softer, i.e. more amorphous, with increasing shear rate. In the initial stages of the experiment and at low shear rate (<0.2 s^{-1}) the aggregates have a hard crystalline structure. With increasing shear rate a thin amorphous layer forms around the crystalline core. At even higher shear rates the thickness of the amorphous layer grows. Just after increasing the shear rate above the critical shear rate, multiple amorphous layers form and eventually the outer layers start to erode very slowly. When the aggregate reduces in size, previously

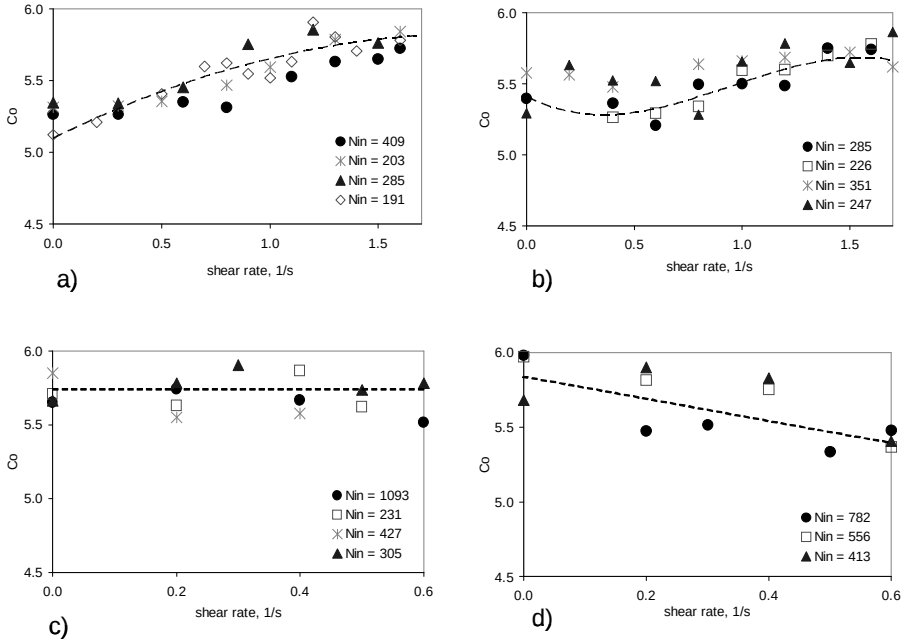

Figure 6.9: *Typical coordination number Co measured for different shear rates for the four different systems: a) WA115, b) WO115, c) WA65 and d) WO65. In the legends of the graphs are shown the initial number of particles for the particular aggregate. The measured values are given by the symbols, the lines are guide to the eye.*

crystal layers, on the outside of the crystalline core, also become amorphous. Thus the amorphous boundary is moving inward. The aggregate radius continues reducing until an equilibrium radius is reached. In this situation there is only a single amorphous outer layer surrounding a multiple domain crystal, circular shaped core.

The formation of these multiple amorphous layers has been illustrated in Figure 6.12 for a WA65 aggregate. The ellipses approximately indicate the boundary between the core and the outer layers. The insets in the figure are the same images in black and the white for better visualization of the more open amorphous layer. It can be seen clearly that the core has a crystalline structure and that the outer layers are amorphous. It cannot be seen on these pictures, but the particles in the amorphous layer are continuously rearranging.

The aggregates with large particles, which are supposed to behave as solid body, develop a much more narrow and slower amorphous layer (see Figure 6.13), than the small particles systems.

Summary The main differences between the systems are summarized in Table 6.2.

As one can see the aggregate behavior for the water-air and water-oil interfaces is similar but there are significant differences in behavior between the large (115 μm) and small (65 μm) particle systems. The most important difference is the critical shear rate. The experiments show that the critical shear rate for the small particles systems is about two times smaller that the critical shear rate for the large particle systems, while according

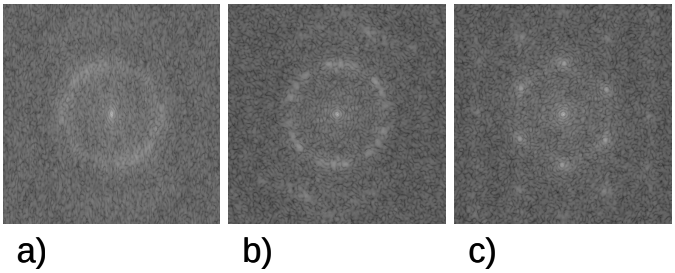

Figure 6.10: *Evolution of FFT for WO115 system with Nin=285 at: a) initial state, b) shear rate 1 s^{-1} and c) 1.4 s^{-1}.*

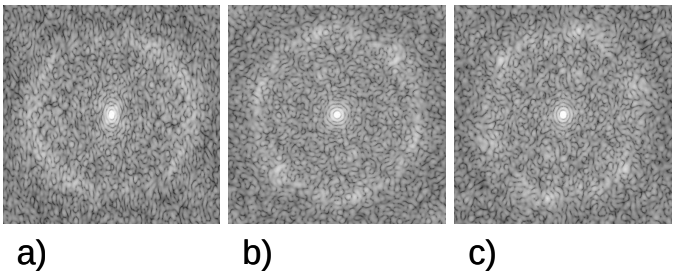

Figure 6.11: *Evolution of FFT for WO65 system with N_{in} = 413 at: a) initial state, b) shear rate 0.3 s^{-1} and c) 0.5 s^{-1}.*

to the theory developed in section 6.2.3 it is expected to be 4 times smaller. The theory considers only capillary and hydrodynamic forces and the difference with the experiments shows that other factors play role too. The difference is explained by assuming different value of the fitting coefficient f_d. As shown in Figure 6.7 $f_d = 0.19$ for the big particles system and $f_d = 0.11$ for small particles system describes well the experimental data. The value of f_d can be linked to the difference in the properties of the experimental systems, such as different roughness and mobility of the particles or different degree of shielding from the neighboring particles. The smaller value of f_d for the WA65 systems indicates either that the roughness of the particles is less, or that their increased mobility reduces the "grip" of the flow on the particles.

We believe that the friction force is a very important factor. The smaller friction forces in the Wx65 system allows the aggregate to restructure more easily and hence it adjusts faster to the continuously changing deformational field. This will effectively lead to a higher critical shear rate than expected.

The presence of smaller friction forces in the Wx65 systems could also explain the difference in the Co of the initial configuration. Smaller friction forces in the Wx65 system allow the particles to slide over each other easier than in the Wx115 system, which results in an energetically more favorable, i.e. denser, initial aggregate configuration.

The formation of an amorphous layer around a crystalline core can be explained also by considering friction forces. A friction force between two adjacent surfaces is proportional to the normal force acting on these surfaces. Inside an aggregate the normal forces are

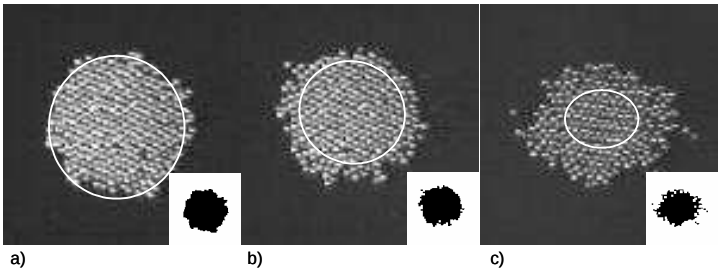

Figure 6.12: *Formation of amorphous layers with increasing shear rate for WA65 at shear rates: a) 0.6 1/s, b) 0.7 1/s and c) 0.8 1/s. The initial number of particles was Nin=305. The insets show black and white transformation of the original images. The amorphous layers are outside of the drawn ellipses.*

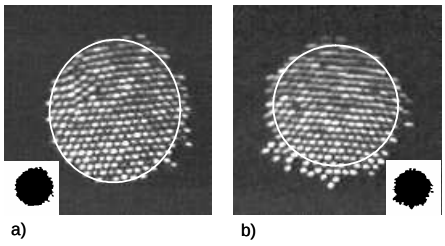

Figure 6.13: *Formation of amorphous layers with increasing shear rate for WA115 at shear rates: a) 1.5 1/s and b) 1.8 1/s. The initial number of particles was Nin=285. The insets show black and white transformation of the original images. The amorphous layer are outside of the drawn ellipses.*

the largest in the central region of the aggregate and the resulting friction forces will prevent the particles from sliding over each other. The friction forces on the outside of the aggregate are not that large and hence the particles on the outside can slide and move around, resulting in an amorphous outer layer. Due to the size of the particles the normal forces and so these friction forces are smaller for the Wx65 systems and a much thicker amorphous layer will develop, just as observed in the experiments. In a transient situation (i.e. not an equilibrium state), just after a change in shear rate, particles on the outside start eroding away, the aggregate becomes smaller and both the normal forces and the friction forces inside the aggregate become smaller too. As a consequence with reducing aggregate size the thickness of the amorphous layer is more or less preserved. In addition, difference in the surface roughness of the particles of both system will lead to difference in the friction force.

Break-up mechanisms

First it has to be noticed that due to their motion in the Couette apparatus, the aggregates are not permanent in the field of view of the camera. Hence, it is difficult to observe the aggregate break-up directly. For example, if an aggregate returns into the field of view in several pieces it is not obvious whether it fragmented, or eroded and afterwards

System	$\dot{\gamma}_{cr}$, s^{-1}	Init. Co	Am. layer	Structure
WA115	1.9±0.1	5.4±0.6	Small	Mostly single domain crystalline, hard
WO115	1.9±0.3	5.2±0.4	Small	Single domain crystalline or with defects, hard
WA65	0.8±0.1	5.7±0.1	Increasing with $\dot{\gamma}$	Multi domain crystalline, hard $(\leq 0.6\ s^{-1})$ and soft $(> 0.6\ s^{-1})$
WO65	0.6±0.1	5.8±0.2	Increasing with $\dot{\gamma}$	Multi domain crystalline, hard $(\leq 0.3\ s^{-1})$ and soft $(> 0.3\ s^{-1})$

Table 6.2: *Summary of the differences between the experimental systems. Am layer stands for amorphous layer.*

re-aggregated during the time that it was not visible. The mechanism of break-up was determined from the direct observations in front of the camera and from indirect indications such as the size of the aggregate as a function of time or the presence of single particles in the system. We observed both erosion and fragmentation in the experiments. Below we consider the two mechanisms separately.

Break-up by erosion Erosion was observed in all four experimental systems. In Figure 6.14, and in Figure 6.5c) and d), one can see single particles eroding. Unfortunately, such a direct observation was not possible for all experiments; therefore these observations alone are not decisive to consider erosion as the only break-up mechanism.

If one considers the size distribution of the aggregates after break-up, the erosion seems more pronounced for the small particles systems (see the images in Figure 6.5). For the small particle systems, there are a lot of single particles present as can be observed from Figure 6.5d). When the size distribution after break-up contains mainly single particles, this is a strong indication of erosion. However the eroded particles can form new aggregates again, hence the presence of small aggregates after break-up is not inconsistent with erosion, too.

The third argument for erosion is given by the time dependence of the effective aggregate radius. Erosion will show a continuous decrease in time, while fracture is a discontinuous, step wise reduction in aggregate size. Figure 6.15 presents the number of particles in the aggregate as a function of time for three of the investigated systems As one can see the change in the number of particles is gradually decreasing, indicating break-up by erosion. However, due to lack of sufficient data points, because data points can only be taken when the aggregate is in the field of view, we can not absolutely discriminate between erosion or fragmentation. For example, the curve with open triangles in Figure 6.15d) could be due to both erosion and fragmentation.

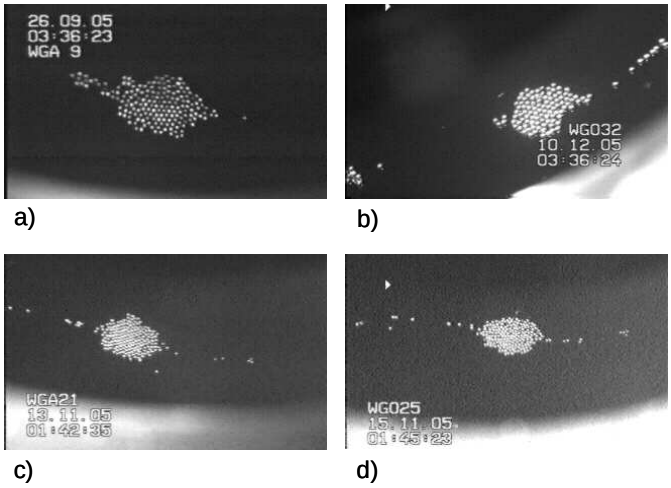

Figure 6.14: *Direct observation of erosion for systems: a) WA115, at shear rate 1.9, experiment with N_{in} = 291, b) WO115, at shear rate 2.1, N_{in} = 222 c) WO65 at shear rate 0.7 s^{-1}, N_{in} = 305 and d) WA65 at shear rate 0.8 s^{-1}, N_{in} = 556.*

As seen in Figure 6.15 erosion of the aggregates occurs at several shear rates. At every shear rate a steady state is reached. This is explained by the critical shear rate dependence on the aggregate size. However, the calculations for the critical shear rate show only a weak dependence on the aggregate size (Figure 6.3).

Break-up by fragmentation Figure 6.16 shows consecutive images of the break-up process. On the video recordings it can be seen that the separate fragments of the aggregate move independently from the main aggregate. In the static pictures this temporal information has been lost and the separate pieces appear to be still attached, but they are not. The last frames show the daughter aggregates when break-up has been completed. Break-up in fragments in front of the camera was not observed for the small particle systems.

The fragmentation occurs at the periphery of the aggregate, as one can see in Figure 6.16 and the aggregate breaks in more than two parts. It was also noticed that the fragmentation starts with a single rupture. Rupture of the first fragment triggers more rupturing processes. This cascade of fragmentation can be explained from the fact that the aggregate loses it circular shape and thus becomes weaker once the first part has been broken.

The critical shear rate for the two cases in Figure 6.16 is quite different, i.e. 2.2 s^{-1} for the first and 1.3 s^{-1} for the second case. Partially this is due to the statistical nature of the break-up process. But it is also due to the aggregate size dependence of the critical shear rate. For instance large aggregates can contain more defects that will promote the fragmentation. For the aggregates shown in the Figure 6.16 the break-up occurred about 1-2 minutes after applying the shear rate. Which is much faster than the processes in Figure 6.15.

In summary, break-up by both erosion and fragmentation has been observed. Single and multiple particle erosion is the prevailing process. As it was shown in Figure 6.3,

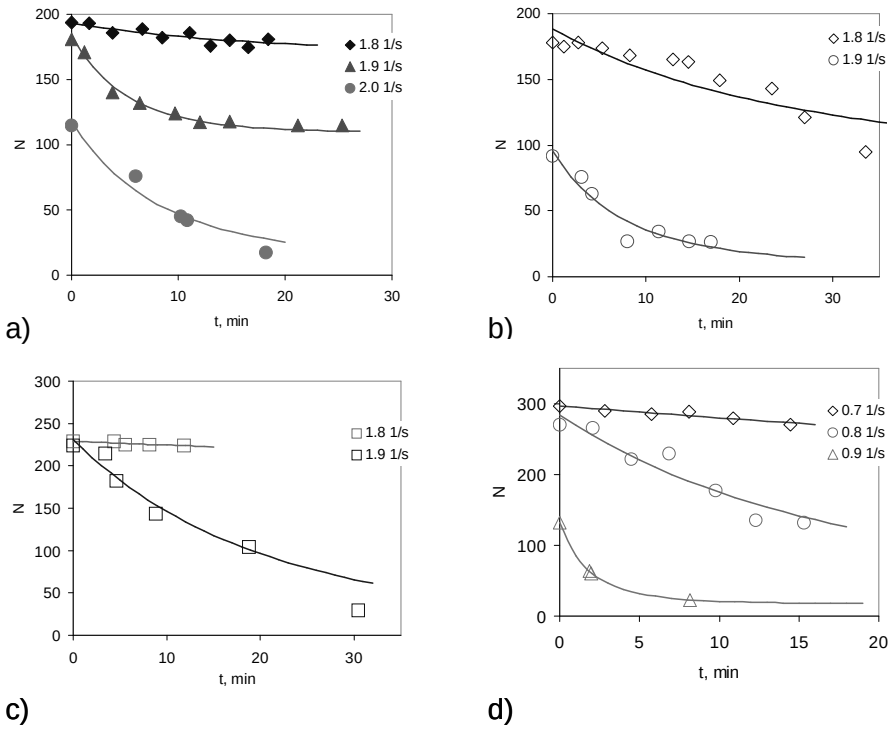

Figure 6.15: *Number of particles as a funtion of time for three of the experimental systems: a) and b) WA115, c) WO115 and d) WA65. With symbols are given the experimental points and with line the fitting according to the model. The shear rates are shown on the graphs.*

the critical shear rates for fragmentation and erosion are similar, thus it is expected that the aggregates can break by both mechanisms. We have indications that fragmentation is promoted by the presence of defects in the crystal structure. The analysis of the video images clearly showed that aggregates with a perfect hexagonal structure will break by erosion due to the stronger bonding between the particles in the inner regions of the aggregate [11]. Due to the high normal forces and large friction forces, restructuring in the Wx115 systems is more difficult than in the Wx65 systems. The small particle aggregates restructure easier with the applied flow, which explains why these systems break only by erosion.

Comparison with the kinetic model for erosion

In this section the kinetic model for erosion, developed in section 6.2.4, is evaluated by comparing it with the experimental data, i.e. the number of particles in an aggregate as a function of time after the shear rate in the Couette cell has been increased. Because the aggregates move in and out the field of view, it is difficult and time consuming to collect this data. Hence only a few experiments have been processed in this way. To be able to

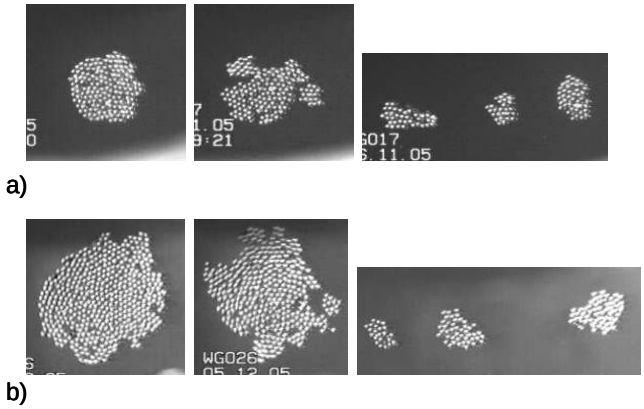

Figure 6.16: *Breaking in the field of view for WO115 system. Case a) corresponds to* N_{in} *=164 at shear 2.2* s^{-1} *and case b) to* N_{in} *= 449 at shear 1.3* s^{-1}*. The first frames show the aggregate before to be broken while the last frames show the broken aggregate the next time it passes in front of the field of view.*

compare the model with the experimental results we rewrite Eq.(6.11) as:

$$N(t) = (a + b * exp(-ct))^k \tag{6.12}$$

where the constants are defined as follows :

$$\begin{aligned} a &= (N_\infty)^{1/k} \\ b &= (N_0)^{1/k} - (N_\infty)^{1/k} \\ c &= \frac{2A\gamma}{k} = \frac{6\sqrt{3}c_1\pi\mu f_d R_p^2\gamma}{k} \end{aligned}$$

The only unknown is the proportionality constant c_1, which is part of the constants A and c. The numbers N_0 and N_∞, received from the constants a and b, can be compared with the experimental values. The optimum k-value has been found by fitting Eq. 6.10 to the critical shear rate as a function of the number of particles, as given in Figure 6.3. For the particles with a radius of $115\mu m$ the optimum k-value is 7 and for the particles with a radius of $65\mu m$ the optimum k-value is 34. The constants a, b and c were used as fitting parameters, for k the values given above were used.

In Figure 6.15 the experimentally obtained time dependence of the aggregate size has been given for the WA115, WO115 and WA65 systems, together with the model fit. The kinetic model for erosion describes the experimental data reasonably well. All the resulting values for the fitting parameters are presented in Table 6.3. In the table R^2 is the statistical coefficient of determination which shows how closely the fitted values correspond to the actual data.

From the table we observe that the fitted values for N_0 and N_∞ are in good agreement with the experimental values. However, the values for A scatter quite a lot for the different shear rates which is in disagreement with the model. The model implies that the A-value should be the same for each experiment within the same experimental system. Thus the model can not be completely validated both due to the scattering in the fitting parameter

System	$\dot{\gamma}_{cr}$, s^{-1}	k	A	R^2	$N_{0,fit}$	$N_{0,\exp}$	$N_{\infty,fit}$	$N_{\infty,\exp}$
a)	1.8		0.107	0.99	193	194	170	175
WA115	1.9	7	0.304	0.98	184	181	110	115
	2.0		0.100	0.95	118	115	10	17
b)	1.8		0.057	0.80	189	178	89	92
WA115	1.9	7	0.105	0.92	95	92	8	26
c)	1.8		0.006	0.73	229	229	78	224
WO115	1.0	7	0.026	0.95	224	224	4	29
d)	0.7		0.237	0.88	297	297	156	270
WA65	0.8	34	0.419	0.88	284	270	17	132
	0.9		4.719	0.99	132	132	18	23

Table 6.3: *Summary of the fitting constants for Figure 6.15*

A and the insufficient number of experimental data. A possible explanation for the spread in A-values could be that the real break-up mechanism consists of a mixture of fragmentation and erosion instead of just pure erosion. Erosion could be dominant in the measurement sets that fit the model reasonably well (Figure 6.15a and d).

6.4 Conclusions

Both break-up by erosion and fragmentation have been observed. Erosion was observed in all investigated systems while fragmentation was seen only for the large particle systems. According to the calculations the critical shear rates for erosion and fragmentation are similar, thus both mechanisms can occur simultaneously. We have shown examples where break-up in fragments was initiated by the presence of defects in the aggregate structure.

No differences in the behavior have been observed between the water-air and water-oil systems, but the differences between the large and small particle systems were significant. They differ in the critical shear rate, coordination number and orientational ordering as shown by the Fourier images.

These differences can be understood by noting that the normal forces in the center of the aggregate are larger than near its rim. These normal forces and so (as we assume) the resulting friction forces are larger for the larger particle systems. Hence restructuring in the central part of the large particle aggregates is hardly possible and fracturing initiated by crack growth is in favor. In the small particle aggregates this restructuring is feasible and so crack growth is unlikely while erosion far inside the aggregate is possible. However, analytical modeling of these friction forces is very difficult and we propose for future work to use numerical simulation techniques to model our experimental system in order to get more insight in the influence of friction forces on the aggregate behavior in a shear flow and possibly to support our conclusions here.

The critical shear rate for break-up by fracturing or erosion could be described by our model calculations, assuming a quite low value for f_d. This low f_d value can be explained by the hydrodynamic interaction with neighboring particles which at contact lowers the

net drag force on the particle. Also the time evolution of the aggregate sizes after a step increase in shear rate, was reasonably well described by our model calculations. However an insufficient number of experimental data is available to fully confirm or invalidate the erosion kinetics model.

References

[1] Wills B.A., *Mineral processing technology* (Int. Ser. Material Sci. Technology, vol 41, Pergamon press, Oxford **1988**.

[2] Elimelech M., Gregory J., Jia X., Williams R.A. *Particle deposition and Aggregation*, Butterworth-Heinemann, Woburn, **1998**.

[3] Jarvis P., Jefferson B., Gregory J. and S.A Parsons, *Water Research*, **2005**, 39, 3121.

[4] Ottino J.M, DeRoussel, Hansen S. and Khakhar D.V., *Adv. Chem. Eng.* **1999**, 25, 105.

[5] Parker D.S, Kaufman W.J., Jenkins D.J, *San. Eng. Div. Proc. Amer. Soc. Civ. Eng.* **1976**, 102, EE2, 251.

[6] Redner S. (H.J Herrman and S. Roux, Eds.), *Statistical models for the fracture of the disordered media*, Elsevier, North-Holland, 321,**1990**.

[7] Thomas D. G., *AIChE J*, **1964**, 10(4), 517.

[8] Mühle K., *Coagulation and Flocculation* (B. Dobiáš Ed.), 355, Marcel Dekker, New York, **1993**.

[9] Thomas D.G., *AIChE J*, 1964, 9(4), 303.

[10] Pantina J.P, Fust E.M, *PRL* **2005**, 94, 138301.

[11] Yeung A.K., Pelton R., *JCIS* **1996**, 184,579.

[12] Zhang Z., Sisk M. L., Mashmoushy H. and Thomas C.R. *Part. Part. System Characterisation* **1999**, 16, 278.

[13] Stancik E. J., Gavranovich G. T., Widebrant M. J. O, Laschitsch A. T., Vermant J. and Fuller G. G., *Faraday Discuss.* **2003**, 123, 145.

[14] Stancik E. J., Hawkinson A. L., Vermant J. and Fuller G. G., *J. Rheol.* **2004**, 48(1), 159.

[15] Aveyard R., Clint J. H., Nees D., Paunov V. N. *Langmuir* **2000**, 16, 1969.

[16] Aveyard R., Clint J. H., Nees D., Quirke N. *Langmuir* **2000**, 16, 8820.

[17] Hoekstra H., Vermant J. and Mevis J., *Langmuir* **2003**, 19, 9134.

[18] Hansen P. H., Malmsten M., Bergenstahl B.,Bergstrom L. *J. of Colloid Interface Sci.* **1999**, 220,269.

[19] Bagster D. F., Tomi D., *Chem. Eng. Sci.* **1974**, 29, 1773.

[20] Adler P. M., Mills P. M. *J. of Rheol.* **1979**, 23, 25.

[21] Sontag R. C. and Russel W. B. , *JCIS* **1987,** 115, 378.

[22] Rumpf H., *Agglomeration* (W.A.Knepper Ed.), Wiley Interscience, New York, **1962**.

[23] Kendall K., *Powder Metallurgy* 31, 28, **1988**.

[24] Powel R. L. and Mason S. G. *AIChE J* **1982**, 28, 286.

[25] Pandya J.D. and Spielman L. A., *JCIS* **1982**, 90, 517.

[26] de Rooij, R., Potanin, A. A., van den Ende, D., Mellema, J., *J. Chem. Phys.* **1994**, 100(7), 5353.

[27] Tolpekin V.A., Duits M.H.G., van den Ende D., Mellema J. *Langmuir* **2004**, 20 (7), 2614.

[28] Cundall p. A. and Strack O. D. L., *Geotechnique* **1979**, 29(1), 47.

[29] Higshitani Ko, Iimura K., *J. of Colloid Interface Sci.* **1998**, 204, 320.

[30] May Lim and Amal R., *9th APCChE Congress and CHEMECA* ,paper 581, **2002**.

[31] Vassileva, N. D.; van den Ende, D.; Mugele, F.; Mellema, J., *Langmuir* **2006**, 22(11), 4959.

[32] Nikolaides M. G., Bausch A. R., Hsu M. F., Dinsmore A. D.,Brenner M. P., Gay C. and Weitz D. A., *Nature* **2002**,420, 299.

[33] Vassileva, N. D.; van den Ende, D.; Mugele, F.; Mellema, J. *Langmuir* **2005**, 21, 11190.

[34] Manas-Zloczower I. and Feke D. L, *Intern. Polym. Process. II 3/4*, 185, **1988**.

[35] Van de Ven, T. G. M. *Colloidal hydrodynamics*, Academic Press: London, **1989**.

[36] Feke D. L and Manas-Zloczower I., *Chem. Eng. Sci.* **1991**, 46, 2153.

Chapter 7

Overview and perspectives

This manuscript describes the work done to investigate the influence of hydrodynamic flow on the properties of 2D aggregates. We choose to work with a 2D system because it is more convenient for optical observation, there is no gravitational settling and the theoretical modeling is simpler. We believe the 2D systems are a good model system and starting point for the investigation of the more complicated 3D aggregates.

Our method is direct and nondestructive. We observe with video microcopy single aggregates, which gives us a detailed look into the processes of breaking. In addition, the reverse process of aggregation after collision with another aggregate is suppressed, which simplifies the modeling additionally.

However the method has certain drawbacks too. First, like every method looking at single particle level, it is difficult to get enough results for statistically significant data. Second, it was not possible to keep the aggregates in the field of view and thus the exact moment of aggregate breaking is lost.

To be able to collect statistically reliable data we work with aggregates consisting of big non-colloidal particles which will give a similar initial structure. Using big particles results in a well defined attraction force. For that purpose also the interface shape was measured and controlled. In our experiments the capillary force is the main force and all the other forces are negligible. There is an easy and accurate way to calculate the capillary force by measuring the contact angle of the particles. The multiple particles interactions are also well defined as shown in the thesis.

In our experiments we observe a single aggregates for long time at different shear rates. Four different experimental systems were used. The type of liquid interface and the size of the primary particles were varied. We consider floc structure, shape and size.

Floc structure is directly related to the floc strength which is defined by the number of bonds between the individual particles. Thus one of the most important property of the aggregates is their porosity. It was found that the flocs generally get more compact with the applied shear rate. Before the breaking to occur the aggregates become less dense which can be used for prediction of the onset of breaking.

With increasing shear rate the aggregates adopt a more circular shape. The circular shape is something specific to the simple shear flow and was not observed elsewhere. The aggregates try to shape themselves through restructuring along the flow pattern. The rotational component of the simple shear flow rotates the aggregate faster that the shape can adjust through restructuring. Due to the symmetry considerations in that case a circular shape is preferred.

The aggregate behavior at water/air and water/oil interface is similar. Also the critical shear rate is the same for aggregate consisting of the same size primary particles. However, there are significant differences in the aggregate restructuring and critical shear rate depending on the size of the primary particles.

Special attention was paid to the breaking mechanism. Both erosion and fragmentation of the aggregates was observed. The erosion is the prevailing process, especially for the small particles. Direct observation of the breaking process is difficult due to the aggregate not being constantly in the field of view. It was found that the critical shear rate depends weakly on the aggregate size. A simple theoretical model has been developed for comparison with the experimental critical shear rate.

The main advantage of the model is its simplicity. It is applicable to dense aggregates that behave as solid body (the particles are held together by strong capillary and friction forces). Although the particles move together as one solid body every particle is assumed to feel the hydrodynamic force as if it is alone (which is more true for 2D than 3D because the particles can feel the flow from below the interface). The aggregate was modeled as circular shaped with hexagonally packed particles, as was experimentally observed.

We investigated breaking in normal direction along the extensional axis of the flow. Two cases are considered: rupture exactly in the middle on two equal pieces and erosion of a single particle from the periphery. In principle other dividing planes such as breaking of a single particle from the surface of the aggregate can be also considered.

The attractive interactions inside the aggregate were assumed to be pair wise additive. We proved that even at short distances the capillary interactions is just pair wise additive. It is difficult to evaluate the exact hydrodynamic force acting on every particle in the aggregate. Hence the total hydrodynamic force was assumed to be sum of the hydrodynamic force acting on each particle. Such way of treating the hydrodynamic force for sure overestimates it because the shielding from the neighboring particles is not taken into account. This is compensated by using an average friction coefficient for the whole aggregate as fitting parameter.

According to the calculations there is no significant difference in the critical shear rate for breaking in the middle and erosion. Thus both processes can occur in the same time. Moreover, the calculated critical shear rate both for erosion and rupture shows weak dependence of the aggregate size which correlates well with the experiments.

The model was developed further to consider erosion kinetics and was compared with the experientially obtained time dependence of the aggregate size. We found that the model fits the experimental data sometimes well and sometimes not. One possible explanation could be that the real breaking mechanism consists of a mixture of breaking and erosion instead of just pure erosion. Insufficient experimental data is available to completely confirm or invalidate the erosion kinetics model.

In the future it will be interesting to extend the experiments to aggregates with a more open (fractal) structure. The preliminary results showed that aggregates consisting of PMMA particles have fractal structure. It was found that they break at lower shear rates in comparison with the glass particles. One of the problems that one has to expect with more open aggregate structure is worse reproducibility due to the larger variety of internal configurations.

Clearly the transient behavior of the aggregates is very complicated and it is difficult to model analytically. An interesting approach would be to adjust the discrete element method (DEM) developed by Cundal and Higashitani to our experimental system. The ability of this method to visualize transient behavior and to intuitively change and define

all the relevant forces makes it a very strong tool to understand aggregate behavior in shear flows. Especially it would be interesting to model the influence of the friction forces on the transient behavior, which would be a way to test our interpretation of the experimental behavior.

Summary

In many disperse systems of practical importance (e.g. paints, dairy products), one observes, under certain circumstances, aggregation of the suspended particles. Aggregation phenomena are also an important issue in many solid-liquid separation processes as mineral processing or waste water treatment, where one has to deal with both colloidal and non-colloidal particles. In another application field colloidal or non-colloidal particles (organized in 2D structures) are used as stabilizing agents of foams and emulsions (known as Pickering emulsions) encountered in many industrial and natural processes such as food, cosmetic and pharmaceutical products. To improve the properties of these products or the efficiency of these processes one needs a detailed knowledge of the behavior and properties of the aggregates involved. The behavior of an aggregate in shear flow can be quite complex. The aggregate may deform, restructure or break-up.

Our goal is to find the relationship between the behavior of an aggregate and the shear flow to which it is subjected. In this thesis an experimental study of 2D aggregates (as a model for 3D structures) in shear flow is presented. We are interested in the critical shear rate at which the aggregate will break-up, but also in the structural changes that the aggregates undergo due to the applied shear flow. We investigate single aggregates, in this way only the disintegration of the aggregate is considered and the process of aggregation is negligible.

In the literature flock break-up has been classified in two general categories. The first one is the removal of single particles or small aggregates from the parent aggregate surface (erosion). The second consists of flock break-up into pieces with similar size (fragmentation). However, direct observations of erosion or fragmentation are scarce.

In the first part of the thesis the experimental setup and its characteristics are described. The set-up consists of Couette device with two concentric cylinders rotating in opposite directions. In the gap between them two liquids are inserted on top of each other, forming an interface. When small (i.e. submillimeter) particles are added, they are trapped at the interface due the interfacial tension force. Under the influence of gravity every particle slightly deforms the interface which causes a capillary interaction force with neighboring particles. These capillary interactions are strong enough to induce aggregation of the particles. The resulting aggregate is observed from above with a ccd camera connected to a video recorder.

The flow properties, to which the aggregates are subjected in our Couette device, are described in chapter 2. The initial idea was to keep the aggregate in the stagnant zone of the flow field and so in the field of view of the camera, by continuous adjustment of the cylinder speeds, using a feedback loop. However, calculation of the transient flow profile after speed adjustment showed that the characteristic time for reaching the steady-state profile is about 45 s in a typical case. Due to this long response time we are not able to

keep the aggregate under investigation in the field of view. Hence, we allow for a slow rotation of the aggregate. The camera is kept stationary and the aggregate is observed during the time it passes the field of view.

To prevent capillary interactions of the particles with their environment due to the interface curvature, the liquid-liquid interface, without particles, should be completely flat. To this end we modified the Couette device in order to be able to control the interface shape. The lower sides of both cylinder surfaces have been constructed of a hydrophilic material while the upper sides are hydrophobic. The interface can be pinned to the transition between these two surfaces. By optimizing the amount of lower liquid, while the interface is pinned, and checking the interface slope using a laser beam refraction technique, a flat interface is achieved.

Chapter 3 and 4 of the thesis deal with the capillary interaction between the particles without any shear field applied. We report both new experimental results and a analytical method to calculate many particle capillary interactions. Chapter 3 describes a single particle trapped at an otherwise flat interface and the capillary interactions between two particles trapped at an interface. The method is developed further in chapter 4 to include capillary interactions between multiple particles. For a single particle at the interface it is shown that the vertical position of the particle relative to the interface is completely determined by the three-phase contact angle. Also the interfacial deformation due to the particle can be calculated given this contact angle. On the two particle level, knowing the deformation of a.single particle the interaction force between two particles can be found. At not too close distances between the particles the linear superposition approximation (LSA) can be used in which the deformation due to these particles is just the sum of the single particle interface profiles. At close distances the correct boundary conditions at the particle surface will be violated (the contact line on the particle surface is not circular) and the LSA will give erroneous results. In order to be able to calculate the correct force, first the exact boundary conditions are derived. Three cases are considered: a meniscus meeting a flat wall, a cylinder surface and a sphere. After that, an analytical procedure is developed to solve the linearized Young-Laplace equation that describes the interface and calculate the forces for an arbitrary number of particles. The full solution is expressed in a series of Bessel functions with coefficients determined by the contact angles at the particle surfaces. The lowest order term of the full solution is the LSA solution. The background curvature of the interface (for instance due to the container) can be also introduced as additional term in the solution. It turned out that for submillimeter particles which can adjust themselves to the interface the LSA is sufficient to describe the interaction, even at contact.

The capillary force calculations were checked experimentally. We used video microscopy to monitor the motion of individual particles and pairs of interacting particles at a liquid-liquid interface with a slight background curvature. By analyzing the video images the particle velocities have been determined. Since the capillary force should balance the viscous drag force, one is able to calculate the force on a particle from its velocity. The measured velocities (and thus the capillary forces) are in good agreement with the LSA predictions, while a physical realistic value was obtained for the only fitting parameter used in the calculations.

The resting part of the thesis deals with single 2D aggregates in shear flow. In chapter 5 we consider restructuring of aggregates of different sizes as a function of the applied shear rate and time, using different characteristics of the aggregate such as aspect ratio, coordination number, pair correlation function, orientational correlation function and

Fourier images of the aggregate structure. It was found that the aggregates adopt a more circular shape, and the particles order in a more dense, hexagonal structure at higher shear rates. We attribute this to the rotation of the aggregates in the shear field. However, just before break-up a small decrease of the order was observed which is an indication that the aggregate structure starts to disintegrate under the applied shear flow.

Moreover, we have investigated the critical shear rate for fragmentation of a single aggregate in simple shear flow. There appeared to be a narrow band of shear rates at which aggregates will break-up independent of their size: $\dot{\gamma}_{\mathrm{crit}} = 1.8 \pm 0.2\ \mathrm{s}^{-1}$ for $20 < N < 400$ (with N the number of particles inside the aggregate). A simple theoretical model has been developed to explain the experimentally observed critical shear rate for break-up. In this model the aggregate is considered as solid circular disk that will fragment in two more or less equal parts. The capillary and drag forces on these parts of the aggregate were calculated and by balancing these forces an expression for the critical shear rate was obtained. In chapter 6 the model for aggregate break-up was extended to erosion of single particles. The model shows a weak dependence of the critical shear rate on the aggregate size (similar to the critical shear rate behavior for fragmentation) which is consistent with the experimental observations. Also the kinetics of the erosion process was modeled and compared with the experimentally obtained time dependence of the aggregate size.

The experimental part of the study was extended to two different particle sizes, and aggregates trapped in a water-air interface and a water-oil interface were investigated. Special attention was paid to the characteristics of the break-up process. Both erosion and fragmentation were observed, but erosion was the dominant process, specially for the smaller particles. The aggregate behavior at the water-air and water-oil interfaces is quite similar. Also the critical shear rate is the same. We observed, however, significant differences in the critical shear rate and aggregate restructuring for different particle sizes. The results show that the friction coefficient f_d is different for aggregates consisting of large particles and small particle aggregates. Clearly other factors than capillary and drag force play a role, too. Probably, friction forces between contacting particles are an important factor as well as the details of the hydrodynamic interactions between the particles. These items can be addressed in future research in more detail, for instance by numerical simulations.

Samenvatting

In verscheidene gedispergeerde systemen welke van praktisch nut zijn, zoals verf of zuivel producten, kan men onder bepaalde omstandigheden vlokking ofwel aggregatie van de aanwezige deeltjes waarnemen. Aggregatie verschijnselen zijn ook belangrijk in scheidingsprocessen waarbij men de vaste stofdeeltjes uit een vloeistof wil verwijderen. Voorbeelden zijn het winnen van mineralen en afvalwaterreiniging. Hierbij heeft men met colloïdale en niet-colloïdale deeltjes te maken. Kleine deeltjes worden ook toegepast in schuimen en emulsies, waarbij de deeltjes als stabilisatoren gebruikt worden omdat ze op het grensvlak van de beide fasen gaan zitten. Zulke emulsies noemt men Pickering emulsies. Ze worden veel gebruikt in producten als levensmiddelen, cosmetica en farmaceutica. Om het rendement van deze processen of de eigenschappen van deze producten te optimaliseren, is het van belang om het gedrag en de eigenschappen van deze aggregaten in detail te kennen. Het gedrag van een aggregaat in een afschuifstroming kan vrij ingewikkeld zijn. Zo'n aggregaat kan vervormen, andere structuren aannemen, en zelfs opbreken in kleinere aggregaten, afhankelijk van de sterkte van de stroming.

In dit promotieonderzoek is het de bedoeling om de relatie in kaart te brengen tussen het gedrag van een aggregaat en de stroming waarin deze zich bevindt. In dit proefschrift wordt een experimentele studie beschreven van 2D aggregaten (welke als model voor 3D structuren dienen) in een afschuifstroming. Centrale aandachtspunten zijn de kritische afschuifsnelheid waarbij een aggregaat opbreekt, afhankelijk van zijn grootte, maar ook de structuurverandering die een aggregaat ondergaat ten gevolge van de afschuifstroming. We bestuderen per experiment een individueel aggregaat, zodat we ons kunnen concentreren op het opbreekgedrag van het aggregaat zonder rekening te hoeven houden met het mogelijk samengaan van twee (of meer) aggregaten.

In de literatuur worden twee categorieën van opbreken beschreven. De eerste is het opbreken ten gevolge van het afsplitsen van kleine brokjes of losse deeltjes aan de rand van het aggregaat (erosie genoemd). De tweede is het opbreken van het aggregaat in een paar stukken welke alle ongeveer even groot zijn (fragmentatie genoemd). Er zijn echter maar weinig directe waarnemingen van zowel erosie als fragmentatie beschreven.

In het eerste deel van het proefschrift worden de experimentele opstelling en haar karakteristieken beschreven. In deze studie gebruiken we een Couette apparaat welke uit twee verticale concentrische cilinderwanden bestaat die tegen elkaar in kunnen roteren. Tussen deze twee wanden worden twee vloeistoffen aangebracht. Omdat deze een verschillende dichtheid hebben, ontstaat er een nagenoeg horizontaal grensvlak tussen beide vloeistoffen. Wanneer kleine deeltjes (met submillimeter afmetingen) toegevoegd worden, zullen deze, ten gevolge van capillaire effecten, in het grensvlak ingevangen worden. Door de zwaartekracht zal ieder deeltje het grensvlak een beetje vervormen. Hierdoor ontstaat een zwakke interactie met naburige deeltjes in het grensvlak, de zogenaamde capillaire

wisselwerking. Ofschoon zwak (in ons geval typisch 50 pN), is ze sterk genoeg om aggregatie van de deeltjes te bewerkstelligen. Het resulterende 2D aggregaat wordt van bovenaf met een ccd camera in beeld gebracht. Deze camera is met een videorecorder verbonden, zodat de evolutie van het aggregaat voor verdere analyse op band vastgelegd kan worden.

De stroming waaraan de aggregaten in het Couette apparaat blootgesteld worden, wordt in hoofdstuk 2 in detail beschreven. Aanvankelijk was het de bedoeling om de afschuifstroming zo in te stellen dat het aggregaat permanent in het beeldvlak van de ccd camera zou blijven. In principe kan dit door de rotatiesnelheid van beide cilinders voortdurend zodanig aan te passen dat het centrum van het aggregaat stilstaat. Dit gebeurt door middel van terugkoppeling. De reactietijd van het stromingsprofiel, op een aanpassing van de draaisnelheid van een van de cilinders, moet dan wel voldoende kort zijn. Uit berekeningen aan het inschakelen van het stromingsprofiel bleek echter dat de reactietijd typisch 45 s bedraagt en dat is veel te traag om terugkoppeling toe te passen. Daarom laten we het aggregaat zo langzaam mogelijk met de stroming mee roteren. Nu worden de veranderingen in het aggregaat alleen waargenomen gedurende de tijd dat het in het beeldvlak van de ccd camera is.

Om te voorkomen dat er uitwendige capillaire krachten op het aggregaat werken, moet het grensvlak (zonder deeltjes) perfect vlak zijn. Daarom hebben we het Couette apparaat enigszins aangepast. De onderste helft van beide cilinders is gemaakt van hydrofiel aluminium terwijl de bovenste helft van perspex, een hydrofoob materiaal, gemaakt is. De contactlijn van het grensvlak met de cilinderwand kan vastgezet worden op de aluminium-perspex overgang. Het grensvlak kan nu uitgevlakt worden door de hoeveelheid van de onderste vloeistof aan te passen, terwijl de contactlijn gefixeerd blijft. De vlakheid wordt gecontroleerd door een laserdiffractie techniek toe te passen.

In hoofdstuk 3 en 4 wordt de capillaire wisselwerking tussen de deeltjes in het grensvlak beschreven, nog zonder afschuifveld. Naast nieuwe experimentele resultaten wordt een analytische methode beschreven om de veeldeeltjes capillaire wisselwerking uit te rekenen. In hoofdstuk 3 beschrijven we de vervorming van het grensvlak rond een individueel deeltje in dat, zonder het deeltje volstrekt vlakke, grensvlak. Ook beschrijven we de capillaire wisselwerking tussen twee, in een grensvlak gevangen deeltjes. Deze methode wordt in hoofdstuk 4 verder uitgewerkt voor meerdere deeltjes. Voor een enkel deeltje in het grensvlak laten we zien dat de verticale positie van het deeltje ten opzichte van het grensvlak volledig bepaald wordt door de contacthoek tussen de drie fasen. Ook de vervorming van het grensvlak rond het deeltje kan berekend worden, gegeven deze contacthoek. Op het twee deeltjes niveau kan de capillaire kracht tussen de deeltjes berekend worden, als het vervormd grensvlakprofiel rond de deeltjes bekend is.

Wanneer de deeltjes zich niet te dicht bij elkaar bevinden kan de lineaire superpositie benadering (LSB) gebruikt worden. In deze benadering wordt de vervorming van het grensvlak opgevat als de som van de vervormingen ten gevolge van de afzonderlijke deeltjes. Als de deeltjes echter dicht bij elkaar komen, zullen de randvoorwaarden aan het oppervlak van de deeltjes bij deze aanpak onjuist zijn (omdat de driefasecontactlijn nu niet meer cirkelvormig is) en de LSB zal verkeerde resultaten opleveren. Om de kracht goed te berekenen, worden eerst de correcte randvoorwaarden op het deeltjesoppervlak berekend. Hierbij worden drie gevallen onderscheiden: een meniscus aan een vlakke wand, een cilindrisch oppervlak en een bolvormig oppervlak. Vervolgens wordt een analytische aanpak ontwikkeld om de gelinearizeerde Young-Laplace vergelijking op te lossen. De Young-Laplace vergelijking beschrijft de vorm van het grensvlak. Met de oplossing van deze vergelijking kunnen de capillaire krachten tussen een willekeurig aantal deeltjes berekend

worden. De oplossing wordt uitgedrukt in een reeks Bessel functies. De coëfficiënten in deze reeks worden bepaald door de randvoorwaarden op de deeltjes. De laagste orde term in deze reeks is de *LSB* oplossing. De kromming van het grensvlak (zonder deeltjes) kan ook meegenomen worden als extra term in deze reeks. Het blijkt dat voor bolvormige submillimeter deeltjes, die zichzelf enigszins aan het grensvlak kunnen aanpassen door te roteren, de *LSB* voldoende is om de capillaire kracht te beschrijven, zelfs als de deeltjes elkaar raken.

De krachtberekeningen zijn experimenteel getoetst. Met behulp van video-microscopie is de beweging geanalyseerd van individuele deeltjes en deeltjes paren, welke vast zitten in een vloeistof-vloeistof grensvlak dat licht gekromd is. Uit deze analyse werd de deeltjessnelheid als functie van de deeltjesposities verkregen. Omdat de viskeuze wrijvingskracht op een deeltje (welke evenredig met de zijn snelheid is) gelijk moet zijn aan de capillaire kracht, kan men uit zijn snelheid de capillaire kracht op het deeltje berekenen. De gemeten snelheden (en de daaruit berekende capillaire krachten) zijn in goede overeenstemming met de *LSB* voorspelling, met een fysisch realistische waarde voor de enige fit parameter in de berekening.

Het resterend deel van dit proefschrift handelt over 2D aggregaten in een afschuifstroming. In hoofdstuk 5 beschouwen we het herstructureren van aggregaten van verschillende afmetingen als functie van de opgelegde afschuifsnelheid en de tijd. Hierbij worden verschillende karakteristieke grootheden gebruikt, zoals lengte-breedte verhouding, coördinatie getal, paarcorrelatie functie, oriëntatiecorrelatie functie en Fourier getransformeerde afbeeldingen van de aggregaatstructuur. De aggregaten nemen in een afschuifstroming een rondere vorm aan bij toenemende afschuifsnelheid, en ook de ordening in zeshoekige patronen neemt toe. Deze trend wordt echter doorbroken vlak voordat de aggregaten opbreken. Dan neemt de rondheid en ordening enigszins af. Dit is een aanwijzing dat het aggregaat uiteen begint te vallen onder de opgelegde afschuifstroming.

Daarnaast hebben we de kritische afschuifsnelheid voor fragmentatie van een aggregaat in afschuifstroming onderzocht. Alle aggregaten breken op binnen een nauwe band van afschuifsnelheden, nagenoeg onafhankelijk van hun afmeting: $\dot{\gamma}_{\mathrm{crit}} = 1.8 \pm 0.2\ \mathrm{s}^{-1}$ voor $20 < N < 400$ (waarbij N het aantal deeltjes in het beschouwde aggregaat is). Er is een eenvoudig theoretisch model geformuleerd om de gemeten kritische afschuifsnelheid voor opbreken te verklaren. In dit model wordt het aggregaat opgevat als een platte schijf die in twee min of meer gelijke delen fragmenteert. We hebben een uitdrukking voor de capillaire en voor weerstands krachten op deze delen afgeleid. Door deze aan elkaar gelijk te stellen, is een uitdrukking voor de kritische afschuifsnelheid als functie van het aantal aanwezige deeltjes gevonden.

In hoofdstuk 6 is dit model voor het opbreekgedrag uitgebreid om het opbreken door erosie te beschrijven. Het model laat zien dat de kritische afschuifsnelheid voor erosie zwak afhangt van de aggregaat grootte (vergelijkbaar met de kritische afschuifsnelheid voor fragmentatie). Dit is consistent met de experimentele waarnemingen. Ook de kinetiek van het erosie proces is gemodelleerd en vergeleken met de waargenomen tijdsafhankelijkheid van de aggregaatgrootte na een verandering van de afschuifsnelheid.

In het experimenteel deel van dit hoofdstuk werd het onderzoek uitgebreid naar aggregaten bestaande uit deeltjes van 115 μm en aggregaten met 65 μm deeltjes. Deze aggregaten werden onderzocht in een olie/water grensvlak en in een lucht/water grensvak. Hierbij is speciaal aandacht besteed aan de karakteristieken van het opbreekproces. Zowel fragmentatie als erosie is waargenomen maar erosie kwam het meest voor, met name in de systemen met de kleine deeltjes. Het gedrag van aggregaten in een lucht/water grensvlak

is vergelijkbaar met dat van aggregaten in een olie/water grensvlak. Ook de kritische afschuifsnelheden zijn nagenoeg gelijk. Er werd echter een significant verschil in herstructureringsgedrag en kritische afschuifsnelheid waargenomen tussen aggregaten van kleine en van grote deeltjes. De resultaten laten zien dat de weerstands coëfficiënt f_d voor grote-deeltjes- en kleine-deeltjes-aggregaten sterk verschilt. Kennelijk zijn andere factoren dan de capillaire en weerstandskrachten van invloed op het opbreekproces. Mogelijkerwijs zijn de wrijvingskrachten, die tussen elkaar rakende deeltjes op kunnen treden of de details van de hydrodynamische wisselwerking tussen de deeltjes, van belang. Deze punten kunnen in een toekomstige studie nader onderzocht worden, bij voorbeeld met behulp van numerieke simulaties.

Acknowledgments

It all started one cool November day 5 years ago in Enschede, when my future promoter asked me "Are you ready to work hard? Very hard?"... And now already at the finish I would like to acknowledge all the people that were part of my project and life during this unique PhD experience.

First of all, I would like to express my gratitude to my promoter, Jorrit Mellema for the opportunity given to work in his group. I appreciate his insightful comments and helpful pieces of advice during our discussions. His critical mind demands standard of research that is not easy to fulfill and forget.

I would like to credit my advisor, Dirk van Ende, for the supervision, patience and support. I am indebted for his contribution in the developing the theoretical models in the present thesis and the editing of all my written materials. I especially admire his ability to build theoretical models (almost about everything). He showed to such a definite experimentalist as me the beauty of the theoretical modeling.

To Frieder Mugele I am grateful for the constructive suggestions and editing of the articles we wrote. From him I learned exactly how many figures are too many for an articles and how to write more concise and up to the point. I was also fascinated by his passion and enthusiasm for science (which is so important in the final stages of a PhD).

Thanks to the members of my doctoral committee (Wim Agterof, Wim Briels, Han Slot and Hans Hoekstra) for accepting to be part of my committee and the efforts for reading my thesis, your comments and suggestions are appreciated.

I would like to thank The Foundation for Fundamental Research on Matter (FOM) for the financial support of my project.

I owe special thanks to the technicians- Klaas Smit ,Jacob Lopulissa, and Gerrit Beukema. Their specific expertise was important part of the progress in my project. In Bulgaria we say "one can not jump over his own shadow". They helped me to jump over my own shadow.

I would like to say thank you to Ryan Sidin for the interesting scientific discussions and developing the method for measuring the interface shape; to Valentin Tolpekin, who although busy finishing his own PhD project has found the time to answer all my questions about image capturing and analysis; and to Ileana Carpen, for the difficult job of reading and editing of my first manuscript.

I appreciate the help of our secretary, Anneies Cohn-Guichelaar. There were so many things she arranged for me during the years. I will also remember her "good morning" smile, her sympathy and encouragement.

I would also like to express my gratitude to all my colleagues and especially to all my roommates for the nice atmosphere during my stay in The Netherlands.

I would like to mention some of the people that I met there and they become my friends- Boris and Arup, you will be always special for me; Yuri and Alexei, I hope we will see each other again; Jacob, your friendship is a treasure for me and I am grateful for your attention; Diana, you are the closest to a sister I ever had; Violeta, I admire your spirit and devotion to work; Roman, I really appreciate your sense of humor and positive way of looking at life; Menno, you are the best listener in the world; Ryan, I think you are meant for great achievements and one day I will be proud that I used to know you.

Also to Bobi, Erik and Ivan thank you for the wonderful evenings we had together while being 'brothers in arms".

I was lucky enough to have a lot of friends from Bulgaria around me that did not let me feel lonely- to Drago for the endless care; to Mira, for the friendship and long phone calls and to the rest of the Bulgarian network (and especially to Simona and Cani, Beni and Lubo, Niki and Ivan, Reni and Marko), it was so nice to have you so close.

Благодаря на майка ми, брат ми и приятелите ми в България (Жени, Веско, Поли и Пламен) за тяхната постоянна любов и подкрепа, за вярата им в мен и моя успех, дори и когато аз не вярвам в себе си. На баща ми, иска ми се и ти да беше тук.

And finally, I would like to say thank you to Joris, my great man. Thank you for creating for me such a nice environment to finish my PhD; thank you for being there for me- day and night; thank you for holding my hand through the difficult moments and for showing me the stars under so many different skies.

ERROR: undefined
OFFENDING COMMAND:

STACK: